UNIVERSITY OF CALIFORNIA,
IRVINE

Nontopological Q-solitons and their Implications for Macroscopic Dark Matter

DISSERTATION

submitted in partial satisfaction of the requirements
for the degree of

DOCTOR OF PHILOSOPHY

in Physics

by

Rebecca Riley

Dissertation Committee:
Professor Arvind Rajaraman, Chair
Professor Mu-Chun Chen
Professor Timothy M.P. Tait

2021

DEDICATION

for Lily

TABLE OF CONTENTS

LIST OF FIGURES

ACKNOWLEDGMENTS

This work has been supported by the National Science Foundation
Graduate Research Fellowship Program, Grant #1839285.

. . .

I would also like to thank the Orange County Chapter of ARCS
for their financial support and their friendship.

VITA

Rebecca Riley

EDUCATION

Doctor of Philosophy, Physics **2021**
University of California, Irvine

Master's, Physics **2020**
University of California, Irvine

Bachelor of Engineering, Computer Engineering **2016**
Vanderbilt University

Bachelor of Arts, Mathematics **2016**
Vanderbilt University

SCHOLARSHIPS & FELLOWSHIPS

Cornelius Vanderbilt Scholar **2013–2016**

UC Irvine Chancellor's Fellow **2017–2019**

National Science Foundation Graduate Research Fellow **2019–2021**

ARCS Foundation Scholar **2019–2021**

LaVerne Noyes Fellow **2021**

REFEREED JOURNAL PUBLICATIONS

Proca Q-balls and Q-shells **2021**
Journal of High Energy Physics, Vol. 2021, Issue 10

Mapping Gauged Q-Balls **2021**
Physical Review D, Vol. 103, Issue 11

Understanding Q-balls Beyond the Thin-Wall Limit **2021**
Physical Review D, Vol. 103, Issue 4

The τ Magnetic Dipole Moment at Future Lepton Colliders **2019**
Letters in High Energy Physics, Vol. 2, Issue 2

AWARDS & HONORS

Outstanding Contributions to the Department of Physics & Astronomy **2020**

UC Irvine Grad Slam Champion **2020**

First-Year Russian Award **2020**

TEACHING EXPERIENCE

Teaching Assistant **2017–2019**
University of California, Irvine

Fundamentals of Experimental Physics (52A),
Basic Physics II (3B), *Basic Physics III* (3C),
Classical Physics (7C), *Classical Physics Laboratory* (7LC)

Microelectronics Tutor **2016**
Vanderbilt University

MENTORSHIP

Resonance Cofounder & Graduate Fellow **2018-2021**

PACE Graduate Mentor **2018-2020**

V^2 Engineering Mentor **2014-2015**

RADIO

Host of *Violet Freedom* on KUCI Irvine **2018-2021**

Host of *The Rebelution* on WRVU Nashville **2013-2016**

ABSTRACT OF THE DISSERTATION

Nontopological Q-solitons and their Implications for Macroscopic Dark Matter

By

Rebecca Riley

Doctor of Philosophy in Physics

University of California, Irvine, 2021

Professor Arvind Rajaraman, Chair

Q-balls are stable, compact objects (more precisely, nontopological solitons) that can arise in complex scalar field theories with a $U(1)$ symmetry in which the potential adheres to certain criteria. These objects are of phenomenological interest as candidates for macroscopic dark matter, an as of yet still relatively underconstrained region of dark matter parameter space. Many of the features of Q-balls – including their size, charge, energy, and stability dynamics – can be qualitatively and approximately quantitatively extracted from their potential under minimal assumptions, although exact solutions are only attainable numerically. A thorough analytic study of Q-balls leads to a simplified understanding of the interconnectedness of their parameters, attributes, and dynamics, culminating most notably in a direct mapping between global Q-ball parameters and related gauged and Proca Q-ball parameters.

This work presents several novel results, as previously published by the author and collaborators, including: precise analytic profiles for global, gauged, and Proca Q-balls; proof of various Q-ball relations and identities; precise analytic estimates of a Q-ball's radius, charge, and energy in terms of a universal Q-ball parameter; new bounds on Q-ball radii and stability; and the aforementioned parameter mapping between global Q-balls and gauged and Proca Q-balls. More complex Q-solitons, including excited Q-balls and Q-shells, are also discussed. Together, these objects represent a new candidate class for dark matter.

Chapter 1

Historical overview

1.1 The need for new theories of dark matter

Dark matter was first postulated in 1933 by Zwicky to explain large rotational anomalies of galaxies in the Coma Cluster. [1] Discrepancies between the luminous and rotational mass measurements of galaxies suggested unseen "dark" (more accurately, transparent) matter distributed throughout the universe. Later, theories and simulations of cosmic structure formation would independently confirm the need for additional matter content to seed the timely galactic accretion that produced the observed Universe. Today, sophisticated astrophysics confirms with ever-increasing certainty the fact that our Universe is awash in dark matter. But while it is five times more abundant than ordinary matter in the universe, it has yet to be directly observed.

Dark matter's existence, nature, and origin are critical questions facing particle physics, astrophysics, and cosmology, with implications for our understanding of the origin and future of the universe, galaxy evolution, and the current Standard Model of particles.

Despite additions to the Standard Model since the discovery of dark matter, it has never yielded a viable dark matter candidate. Modern consensus is that dark matter, whether it is a particle or a larger compact object, must be either (a) a new, beyond the Standard Model particle (the prevailing hypothesis) or – less likely – (b) an exotic state of normal matter, the production mechanism for which is, at present times, inaccessible or unknown.

Attempts to profile dark matter have included known particles; theorized new particles (e.g. axions); large, cold "Massive Compact Halo Objects" (MACHOs); or even an abundance of medium-mass, primordial black holes, although many of these possibilities have since been largely ruled out. Candidate dark matter particles should be weakly interacting, lack electromagnetic and color charge so as not to produce visible photons, remain stable for lifetimes on the order of the age of the Universe or longer, and have masses, couplings, and production rates that are compatible with measured dark matter relic densities. As such, the most popular candidate has historically been the Weakly Interacting Massive Particle (WIMP), a relatively heavy new particle that was thermally produced in the early Universe, subsequently underwent a period of freeze-out, and in the current epoch retains a small but detectable weak coupling to the Standard Model. WIMPs gained further popularity with the discovery of the "WIMP miracle," a realization that supersymmetric extensions of the Standard Model naturally produced dark matter candidate particles with the predicted properties of WIMPs.

While a dark matter candidate has yet to be directly observed, it is certainly not for lack of trying. Dark matter detection experiments generically include direct detection, indirect detection, and collider creation. These efforts have primarily targeted WIMPs due to their relative similarity to Standard Model particles and their weak but detectable Standard Model couplings.

Direct searches are based on the detection of dark matter particles passing through detectors and physically interacting with them. They probe the scattering of dark matter particles off nuclei in ultra-low background, deep underground experiments. Examples are the collaborations

CDMS, EDELWEISS, and XENON, which use underground chambers of elemental crystals to detect miniscule nuclear recoil from collisions between WIMPs and atomic nuclei.

Indirect searches are comprised of space- and ground-based observatories that endeavor to detect secondary particles that originated from annihilations of dark matter candidates in the Milky Way or other close galaxies. Experiments including PAMELA and Fermi LAT attempt to detect these annihilation products, typically cosmic gamma rays. While less technically challenging than direct detection, the success of indirect detection experiments relies on intimate knowledge of the distribution of dark matter within the local galaxy and the production of background by other galactic sources, both of which are extremely difficult to estimate.

Particle colliders like the Large Hadron Collider operate at high enough energies to potentially create WIMPs. The primary experimental signature of dark matter in particle colliders is missing transverse energy, a sign that a dark matter particle has escaped undetected. Current technology can identify this missing energy with a high degree of accuracy. Particle colliders are able to probe lower-mass dark matter candidates that are outside the reach of direct detection experiments. Additionally, they have the benefit of different and usually smaller systematic uncertainties compared to direct and indirect detection. The trade-off for this low-mass sensitivity is an upper mass limit from production energy constraints.

Unfortunately, these detection efforts have so far proved fruitless. The silence of experiments searching for WIMPs, as well as mounting doubt over the "WIMP miracle" in light of a lack of positive verification of supersymmetry at colliders, has caused the WIMP picture to fall out of favor in recent times. Physicists are turning to increasingly nontraditional ideas to explain this mysterious element, including, as this work will discuss, solitonic candidates like Q-balls and their sister solitons, Q-shells. As popular theories annually become more tightly constrained, continued exploration and innovation in the theory space is essential in the still uncertain hunt for dark matter.

1.2 What are Q-balls?

Q-balls are stable, nontopological solitons that can arise in theories involving complex scalars ϕ [2]. Under certain conditions, a scalar field theory admits the existence of localized soliton solutions of finite energy. These solutions, called Q-balls, are bound configurations of complex scalars ϕ that are stable against decay into individual particles or smaller Q-balls [3, 2] (for a review see Ref. [4]). The complex scalars must carry a $U(1)$ charge and require either a special scalar potential [5] or the inclusion of gravity as an attractive force [6].

The energy dynamics of such scalar potentials are what class Q-balls as nontopological solitons. These potentials allow for stable Q-configurations due to the fact that a collection of bound particles with charge Q has a lower mass energy than the same number of free particles. Q-balls are nontopological solitons because their stability arises from the existence of compact solutions of lower energy than the corresponding diffusive solution; this is in contrast to topological solitons, which are stable due to a conserved topological charge.

This simple set-up can be modified in various ways. The most obvious is to make the $U(1)$ symmetry local, which leads to *gauged* Q-balls [7]. Another interesting extension is to include more than one scalar field in the soliton [8].

Q-balls have been most saliently analyzed as candidates for macroscopic dark matter of various types [9, 10, 11, 12], including those similar to black holes and neutron stars. (See also Chapter 6.) Many supersymmetric theories naturally predict Q-balls; the global $U(1)$ is identified with baryon or lepton number in these theories. Q-balls could play a role in dark matter [13] or baryogenesis as well as phase transitions in the early universe [14]. They could lead to detectable gravitational wave signatures [15].

Q-ball solutions are additionally interesting in their own right as a rare example of a stable non-topological soliton; their stability is ensured by the conserved $U(1)$ charge as opposed to

a topological charge. Analytic solutions for some special Q-ball potentials have been studied in [16, 17, 18]. However, outside of these special potentials, Q-ball solutions rely on either approximations or numeric solvers, e.g. `Mathematica` [19], to solve their characteristic, non-linear differential equations.

The Q-ball system can be extended and complexified by, for example, charging the complex scalar ϕ under a massless or massive local symmetry (gauged and Proca Q-balls, respectively). [7, 20, 21] Gauged Q-balls are well-motivated phenomenologically given that the Standard Model includes both massless and massive gauge bosons. Unfortunately, they are predictably a more difficult system to analyze. Unlike the global case, no exactly solvable potentials are known at this time. The presence of the gauge field also complicates numeric methods, which are generally restricted to the finite element methods of `Mathematica`.

The case of a massive (Proca) gauge field has received the least attention in the Q-ball literature to date [22, 23, 24, 25], presumably because it is the most difficult system to solve and analyze. However, they are important components of the Q-ball story, not only because they interpolate the intermediary region between global and gauged Q-balls, but additionally because they are interesting in their own right, exhibiting novel effects unique to the presence of a massive gauge field.

1.3 Coleman's Q-balls

Coleman first proposed global Q-balls in 1985 [2], along with a framework for approximating their features which will be employed frequently in the discussion that follows.

Very large, global Q-balls are defined by the radial behavior of a scalar field f. In the interior of the Q-ball, this scalar field takes on some nearly constant, nonzero value, while outside the Q-ball it is zero. The boundary between the interior and exterior of the Q-ball is a "crust" of some width in which the scalar field drops from its nonzero, interior value to zero.

For very large Q-balls, the width of this crust is negligible compared to the total size of the Q-ball. Coleman's ansatz was to take this width to zero as the Q-ball becomes infinitely large, with the result that the scalar field f is described by a discontinuous step function

$$f(\rho) = \begin{cases} 1, & \rho < R^*, \\ 0, & \rho > R^*, \end{cases} \tag{1.1}$$

where R^* denotes the radius of the Q-ball. This ansatz is referred to as the "thin-wall limit."

Coleman used this ansatz to approximate the charge Q and energy E of these large Q-balls.

$$Q = \frac{4\pi}{3}\left(\frac{R^*}{\sqrt{m_\phi^2 - \omega_0^2}}\right)^3 \phi_0^2\,\omega_0 \tag{1.2}$$

$$E = \omega_0 Q + \frac{\pi\phi_0^2}{3\sqrt{m_\phi^2 - \omega_0^2}}\,R^{*2} \tag{1.3}$$

The various parameters appearing in these equations will be defined in the next section. While their accuracy for small and more complex types of Q-balls leaves much to be desired, these approximations form the historical basis for the study of Q-balls and will be referenced frequently throughout this work. They function as a starting point for improved approximations of both the scalar and gauge field profiles of global, gauged, and Proca Q-balls.

Chapter 2

Field theory framework

2.1 Types of Q-balls

Three varieties of Q-balls are treated here: global, gauged, and Proca.

Global Q-balls are solutions to Eq. (2.27) in the limit $e \to 0$ or $m_A \to \infty$. Their hallmark is a global U(1) symmetry $\phi \to e^{i\alpha}\phi$. They are described by (2.11), (2.17), and (2.20).

Gauged Q-balls are the result of promoting the global symmetry $\phi \to e^{i\alpha}\phi$ to a local symmetry, which introduces a new, massless gauge field. They are solutions to Eqs. (2.28) and (2.29) in the limit $m_A \to 0$. They are described by (2.12), (2.18). and (2.21).

Proca Q-balls are gauged Q-balls in which the gauge field is made massive. They are solutions to Eqs. (2.30) and (2.31). They are described by (2.13), (2.19), and (2.22).

2.2 Lagrangians

Global, gauged, and Proca Q-balls are described by the following Lagrangian densities, respectively:

$$\mathscr{L}_{\text{global}} = \left|\partial_\mu \phi\right|^2 - U(|\phi|) \tag{2.1}$$

$$\mathscr{L}_{\text{gauged}} = \left|D_\mu \phi\right|^2 - U(|\phi|) - \frac{1}{4} F_{\mu\nu} F^{\mu\nu} \tag{2.2}$$

$$\mathscr{L}_{\text{proca}} = \left|D_\mu \phi\right|^2 - U(|\phi|) - \frac{1}{4} F_{\mu\nu} F^{\mu\nu} + \frac{m_A^2}{2} A_\mu A^\mu \tag{2.3}$$

ϕ is a complex scalar with potential $U(|\phi|)$. $U(|\phi|)$ is a generic, $U(1)$-invariant, scalar potential that allows for the formation of Q-balls; it is described more fully in Section 2.3. $D_\mu = \partial_\mu - ieA_\mu$ is the gauge covariant derivative and $F_{\mu\nu} = \partial_\mu A_\nu - \partial_\nu A_\mu$ is the field-strength tensor. e is the positive-valued gauge coupling normalized so that ϕ has charge one. m_A is the mass of the new $U(1)$ gauge boson A.

$\mathscr{L}_{\text{global}}$ has a global $U(1)$ symmetry $\phi \to e^{i\alpha}\phi$. There is a conserved Noether charge Q under this symmetry, which is ϕ number. It is normalized here so that $Q(\phi) = 1$. $\mathscr{L}_{\text{gauged}}$ is the result of promoting the global $U(1)$ symmetry in $\mathscr{L}_{\text{global}}$ to a local symmetry, i.e. gauging it. $\mathscr{L}_{\text{proca}}$ is the result of giving the gauge field of $U(1)$ symmetry in $\mathscr{L}_{\text{gauged}}$ a mass m_A.

The gauge field mass m_A can originate in either of two ways:

i) it can be a Stückelberg mass [26]. In this case the $U(1)$ gauge symmetry is unbroken but still fixed in $\mathscr{L}$, while the underlying *global* $U(1)$ symmetry $\phi(t,\vec{x}) \to e^{i\theta}\phi(t,\vec{x})$ is manifestly conserved;

ii) it can originate from spontaneous symmetry breaking by a scalar ψ that is either very heavy or has negligible couplings to ϕ such that they are irrelevant for the soliton dynamics. If the couplings are only negligible and ψ is not heavy, the full Lagrangian $\mathscr{L}(\phi,\psi)$

must feature one global and one gauged $U(1)$ symmetry, only the latter of which is broken by $\langle\psi\rangle$.

Assuming the effects of a heavy and/or very weakly coupled scalar ψ are negligible, the phenomenology is the same for both possible m_A origins. The name "Proca Q-balls" is a general descriptor that encompasses both possibilities for the origin of the massive gauge field A. [1]

2.3 Potential

A potential $U(|\phi|)$ that admits Q-balls must meet, at a minimum, several conditions:

1. Coleman's existence criteria (2.4) must be true.
2. It must have a negative fourth-order term.
3. It must be order six or higher.
4. It must have the vacuum as a stable minimum.

1. Existence criteria for global Q-balls are described by Coleman in Ref. [2]. Namely, global Q-balls may form when $U(|\phi|)/|\phi|^2$ has a minimum at $0 < \phi_0 < \infty$ such that

$$0 \leq \sqrt{\frac{2U(\phi_0)}{\phi_0^2}} \equiv \omega_0 < \omega < m_\phi \,. \tag{2.4}$$

[1] The Romanian physicist Alexandru Proca extended Maxwell's equations to allow a massive vector boson via the eponymous Proca equation:

$$\Box A^\nu - \partial^\nu(\partial_\mu A^\mu) + m^2 A^\nu = j^\nu \,.$$

The Proca Lagrangian density is

$$\mathcal{L} = -\frac{1}{4}F_{\mu\nu}F^{\mu\nu} + \frac{m_A^2}{2}A_\mu A^\mu - j_\mu A^\mu \,.$$

The global $U(1)$ symmetry allows ϕ_0 to be restricted to be real and positive without loss of generality. ω will also be chosen to be positive to ensure a positive charge Q on the Q-ball.

The scalar frequency ω of gauged and Proca Q-balls is not strictly less than m_ϕ but may be equal to it, leading to a similar but modified constraint: $\omega_0 < \omega \leq m_\phi$. In other words, for the gauged and Proca cases $\kappa \leq 1$ rather than $\kappa < 1$ (global case). In Section 2.10, it is shown that there is another, stronger lower bound on ω in the gauged and Proca cases which will not be discussed presently.

2. The negative $|\phi|^4$ term is responsible for the attractive interaction between ϕ particles that allows the formation of Q-balls.

3. The $|\phi|^6$ term stabilizes the potential for large ϕ values. More specifically, it allows the existence of a local minimum ϕ_0 which is a prerequisite for Q-ball formation. A generic quartic potential $U(\phi) = m_\phi^2|\phi|^2 - \beta|\phi|^4$ cannot possess such a local minimum, and so cannot satisfy the existence criteria (2.4).

4. The vacuum is a stable minimum of the potential $U(|\phi|)$ when two conditions are met:

$$\left.\frac{\mathrm{d}U}{\mathrm{d}|\phi|}\right|_{\phi=0} = 0, \qquad m_\phi^2 \equiv \left.\frac{\mathrm{d}^2U}{\mathrm{d}\phi\,\mathrm{d}\phi^*}\right|_{\phi=0} > 0\,. \tag{2.5}$$

m_ϕ is the mass of the complex scalar ϕ.

There is freedom to choose the potential energy in the vacuum; here it will be zero with the selection $U(0) = 0$. Additionally, to preserve the $U(1)$ symmetry, $\langle\phi\rangle = 0$ is required in the vacuum; this implies that $f = 0$ in the vacuum.

Beyond these requirements, it is advantageous to leave the potential as generic as possible to isolate universal Q-ball features from those attributable to a specific potential. A generic,

sextic, scalar potential that admits Q-balls is

$$U(|\phi|) = m_\phi^2|\phi|^2 - \beta|\phi|^4 + \frac{\xi}{m_\phi^2}|\phi|^6 \,. \tag{2.6}$$

β and ξ are positive, dimensionless constants. This $U(|\phi|)$ satisfies all four conditions, including the criteria of Eqs. (2.4) and (2.5). The parameters β and ξ will not appear in the remainder of this work and are excluded in favor of equivalent parameters ϕ_0 – a minimum of $U(|\phi|)$ satisfying Eq. (2.4) – and ω_0.

$$\phi_0 = m_\phi \sqrt{\frac{\beta}{\xi}}, \qquad \omega_0 = m_\phi \sqrt{1 - \frac{\beta^2}{4\xi}}\,. \tag{2.7}$$

The criteria that $0 \leq \omega_0 < \omega < m_\phi$ is alternately expressed as $0 < \beta \leq 4\xi$.

With the inclusion of the $|\phi|^6$ term, $U(|\phi|)$ ceases to become renormalizable. This is an unfortunate but necessary trade-off to allow for the formation of Q-balls. A potential retaining only renormalizable terms would be unable to satisfy the existence criteria (2.4) (c.f. condition #3), excluding the possibility for Q-ball formation.

In a non-renormalizable theory, additional higher-order terms must also be considered. The typical effective field theory perspective is that the $|\phi|^6$ term plays the dominant role in the phenomenology of Q-balls when heavy scalars are introduced; higher order terms are suppressed by additional powers of the heavy scalar mass scale. An order six potential is therefore a reasonable approximation to physical reality and is adopted here. Further discussion of potential phenomenological consequences of Q-balls can be found in Chapter 6.

To date, no exact solutions to Eq. (2.6) are known, so the numeric methods and analytic approximations detailed below are pursued in their stead. For simplicity and concreteness, the discussion that follows will exclusively utilize $U(|\phi|)$ of Eq. (2.6) as a minimalistic potential

that admits Q-balls. However, the results here are also expected to be generally applicable to a broader class of potentials that retain characteristics that make them amenable to Q-balls.

2.4 Spherical symmetry ansätze

In the ground state[2], the simplifying assumption that Q-balls coalesce into a spherical configuration is imposed. (This is also the assumption of Coleman [2] in his original work.) A separable-field ansatz is the basis for spherical solutions to the Q-ball equations of motion.

$$\phi(x) = \frac{\phi_0}{\sqrt{2}} f(r) e^{i\omega t}, \tag{2.8}$$

This form isolates a purely radial, dimensionless scalar function, $f(r)$ (henceforth interchangeably "scalar profile"), from a pure frequency component, $e^{i\omega t}$. In other words, these spherical solutions only depend on time through the phase of ϕ. ϕ_0 is a dimensionful scale constant determined by the scalar potential; see Eq. (2.4). ω is bounded from above and below by $\omega_0 < \omega < m_\phi$ (2.4) (alternately $\omega_0 < \omega \leq m_\phi$ in the gauged and Proca cases).

The gauge field in the gauged and Proca cases is subjected to the constraint that only the electric potential is non-zero. It is also time-independent. (This is the "static charge ansatz" of [7].)

$$A_0(t, \vec{x}) = \phi_0 A(r), \quad A_{1,2,3}(t, \vec{x}) = 0 \tag{2.9}$$

[2] See Chapter 5 for a discussion of excited states.

With the $\phi(x)$ ansatz (2.8) and substituting ϕ_0 and ω_0 for β and ξ, the potential becomes

$$\begin{aligned} U(f) = U(|\phi|) &= m_\phi^2|\phi|^2 - \beta|\phi|^4 + \frac{\xi}{m_\phi^2}|\phi|^6 \\ &= m_\phi^2 \frac{\phi_0^2}{2} f^2 - \beta \frac{\phi_0^4}{4} f^4 + \frac{\xi}{m_\phi^2}\frac{\phi_0^6}{8} f^6 \\ &= \frac{\phi_0^2}{2}\left\{ m_\phi^2 \left(\frac{\beta^2}{4\xi} + \frac{\omega_0^2}{m_\phi^2} \right) f^2 - \frac{m_\phi^2 \beta^2}{2\xi} f^4 + \frac{m_\phi^2 \beta^2}{4\xi} f^6 \right\} \\ &= \frac{\phi_0^2}{2}\left\{ \frac{m_\phi^2 \beta^2}{4\xi}\left(f^2 - 2f^4 + f^6\right) + \omega_0^2 f^2 \right\} \\ &= \frac{\phi_0^2}{2}\left\{ (m_\phi^2 - \omega_0^2) f^2 (1-f^2)^2 + \omega_0^2 f^2 \right\}. \end{aligned} \tag{2.10}$$

The forms of the Lagrangians (2.1), (2.2), and (2.3) also change with the substitution of the separable field ansatz (2.8) and the gauge field constraint (2.9). Extra factors of 4π and r^2 appear in the conversion from $\mathrm{d}^3\vec{x}$ to $4\pi r^2\,\mathrm{d}r$.

$$\begin{aligned} L_{\text{global}} = \int \mathrm{d}^3\vec{x}\ \mathscr{L}_{\text{global}} &= \int \mathrm{d}^3\vec{x}\ \ \partial_\mu \phi \partial^\mu \phi^* - U(\phi) \\ &= \int \mathrm{d}^3\vec{x}\ \left(\partial_t \phi, \vec{\nabla}\phi\right) \cdot \left(\partial^t \phi^*, -\vec{\nabla}\phi^*\right) - U(\phi) \\ &= \int \mathrm{d}^3\vec{x}\ \ \partial_t \phi \partial^t \phi^* - \vec{\nabla}\phi \vec{\nabla}\phi^* - U(\phi) \\ &= \phi_0^2 \int \mathrm{d}^3\vec{x}\ \ \frac{1}{2}\omega^2 f^2(r) - \frac{1}{2}(\vec{\nabla} f(r))^2 - \frac{U(\phi)}{\phi_0^2} \\ &= 4\pi\phi_0^2 \int \mathrm{d}r\ r^2 \left[\frac{1}{2}\omega^2 f^2 - \frac{1}{2} f'^2 - \frac{U(f)}{\phi_0^2} \right] \end{aligned} \tag{2.11}$$

$$
\begin{aligned}
L_{\text{gauged}} &= \int \mathrm{d}^3\vec{x}\ \mathscr{L}_{\text{gauged}} = \int \mathrm{d}^3\vec{x}\ D_\mu\phi D^\mu\phi^* - U(\phi) - \frac{1}{4}F_{\mu\nu}F^{\mu\nu} \\
&= \int \mathrm{d}^3\vec{x}\ \ [\partial_t - ieA_0]\phi[\partial^t + ieA_0]\phi^* - \vec{\nabla}\phi\vec{\nabla}\phi^* - U(\phi) - \frac{1}{4}(\partial_\mu A_\nu - \partial_\nu A_\mu)(\partial^\mu A^\nu - \partial^\nu A^\mu) \\
&= \int \mathrm{d}^3\vec{x}\ \ \frac{\phi_0^2}{2}[f\,i\omega - ieA_0 f][-f\,i\omega + ieA_0 f] - \frac{\phi_0^2}{2}(\vec{\nabla}f)^2 - U(\phi) + \frac{1}{2}A_0'^2 \\
&= \phi_0^2 \int \mathrm{d}^3\vec{x}\ \ \frac{1}{2}f^2(\omega - eA_0)^2 - \frac{1}{2}f'^2 - \frac{U(\phi)}{\phi_0^2} + \frac{1}{2\phi_0^2}A_0'^2 \\
&= 4\pi\phi_0^2 \int \mathrm{d}r\ r^2 \left[\frac{1}{2}f^2(\omega - e\phi_0 A)^2 - \frac{1}{2}f'^2 - \frac{U(f)}{\phi_0^2} + \frac{1}{2}A'^2\right]
\end{aligned}
\tag{2.12}
$$

$$
\begin{aligned}
L_{\text{proca}} &= \int \mathrm{d}^3\vec{x}\ \mathscr{L}_{\text{proca}} = \int \mathrm{d}^3\vec{x}\ D_\mu\phi D^\mu\phi^* - U(\phi) - \frac{1}{4}F_{\mu\nu}F^{\mu\nu} + \frac{m_A^2}{2}A_\mu A^\mu \\
&= 4\pi\phi_0^2 \int \mathrm{d}r\ r^2 \left[\frac{1}{2}f^2(\omega - e\phi_0 A)^2 - \frac{1}{2}f'^2 - \frac{U(f)}{\phi_0^2} + \frac{1}{2}A'^2 + \frac{m_A^2}{2}A^2\right]
\end{aligned}
\tag{2.13}
$$

Primes are derivatives with respect to r. The static charge ansatz (2.9) allows a dramatic simplification of the gauge field terms, particularly $F_{\mu\nu}F^{\mu\nu}$.

2.5 Dimensionless equivalents

A more holistic and universal inspection of Q-ball properties is allowed when relevant quantities are rendered dimensionless. The most important dimensionless quantity, as will become apparent later, is called here κ and defined as

$$
\kappa^2 \equiv \frac{\omega^2 - \omega_0^2}{m_\phi^2 - \omega_0^2} \in (0, 1]\,. \tag{2.14}
$$

Section 2.11 shows that this κ uniquely parameterizes the scalar profiles.

A dimensionless radial coordinate in the same spirit is

$$\rho \equiv r\sqrt{m_\phi^2 - \omega_0^2}, \tag{2.15}$$

with $\rho \in [0, \infty)$. From here on, the scalar and gauge profiles will depend on ρ – $f(\rho)$, $A(\rho)$ – rather than r.[3]

A complete set of dimensionless quantities used throughout the remainder of this work are included here. These quantities will generally be favored over their dimensionful counterparts for expressions.

$$\begin{aligned}
\kappa^2 &\equiv \frac{\omega^2 - \omega_0^2}{m_\phi^2 - \omega_0^2} = \Omega^2 - \Omega_0^2 & \rho &\equiv r\sqrt{m_\phi^2 - \omega_0^2}, \\
\Omega &\equiv \frac{\omega}{\sqrt{m_\phi^2 - \omega_0^2}}, & \Omega_0 &\equiv \frac{\omega_0}{\sqrt{m_\phi^2 - \omega_0^2}}, \\
\Phi_0 &\equiv \frac{\phi_0}{\sqrt{m_\phi^2 - \omega_0^2}}, & \alpha &\equiv e\Phi_0, \\
A(\rho) &\equiv \frac{A_0(\rho)}{\phi_0} & M &\equiv \frac{m_A}{\sqrt{m_\phi^2 - \omega_0^2}} \\
R^* &\equiv R\sqrt{m_\phi^2 - \omega_0^2} & y &\equiv \frac{\rho}{1 + \rho/a}.
\end{aligned} \tag{2.16}$$

Once these dimensionless quantities are introduced, the Lagrangians of Equations (2.11), (2.12), and (2.13) take new, dimensionless forms. Here, primes denote derivatives with respect to ρ rather than r.

$$L_{\text{global}} = 4\pi\Phi_0^2\sqrt{m_\phi^2 - \omega_0^2}\int \mathrm{d}\rho\ \rho^2\left[-\frac{1}{2}f'^2 + \frac{1}{2}f^2\Omega^2 - \frac{U(f)}{\Phi_0^2(m_\phi^2 - \omega_0^2)^2}\right] \tag{2.17}$$

[3] Note that the dimensionful and dimensionless radial coordinates r and ρ, respectively, should not be confused with R and R^*, the dimensionful and dimensionless Q-ball radii, respectively.

$$L_{\text{gauged}} = 4\pi\Phi_0^2\sqrt{m_\phi^2-\omega_0^2}\int \mathrm{d}\rho\,\rho^2\left[-\frac{1}{2}f'^2+\frac{1}{2}A'^2+\frac{1}{2}f^2(\Omega-\alpha A)^2-\frac{U(f)}{\Phi_0^2(m_\phi^2-\omega_0^2)^2}\right] \quad (2.18)$$

$$L_{\text{proca}} = 4\pi\Phi_0^2\sqrt{m_\phi^2-\omega_0^2}\int \mathrm{d}\rho\,\rho^2\left[-\frac{1}{2}f'^2+\frac{1}{2}A'^2+\frac{1}{2}f^2(\Omega-\alpha A)^2-\frac{U(f)}{\Phi_0^2(m_\phi^2-\omega_0^2)^2}+\frac{M^2}{2}A^2\right] \quad (2.19)$$

The above forms suggest an alternative potential $V(f)$ (global Q-balls) or $V(f,A)$ (gauged and Proca Q-balls) as a starting point for analyzing Q-ball dynamics. L_{gauged} (2.18) in particular resembles two scalar fields under the influence of potential $V(f,A)$, but with a "wrong sign" kinetic term for the A field. The "physical" implications of this will be treated in Section 2.10. In keeping with the rest of the quantities presented already, these new potentials are dimensionless.

$$V_{\text{global}}(f) = \frac{1}{2}f^2\Omega^2-\frac{U(f)}{\Phi_0^2(m_\phi^2-\omega_0^2)^2} \quad (2.20)$$

$$V_{\text{gauged}}(f,A) = \frac{1}{2}f^2(\Omega-\alpha A)^2-\frac{U(f)}{\Phi_0^2(m_\phi^2-\omega_0^2)^2} \quad (2.21)$$

$$V_{\text{proca}}(f,A) = \frac{1}{2}f^2(\Omega-\alpha A)^2-\frac{U(f)}{\Phi_0^2(m_\phi^2-\omega_0^2)^2}+\frac{M^2}{2}A^2 \quad (2.22)$$

With these new potentials, the Lagrangians take a form which allows a straightforward extraction of their equations of motion.

$$L_{\text{global}} = 4\pi\Phi_0^2\sqrt{m_\phi^2-\omega_0^2}\int \mathrm{d}\rho\,\rho^2\left[-\frac{1}{2}f'^2 + V_{\text{global}}(f)\right] \tag{2.23}$$

$$L_{\text{gauged}} = 4\pi\Phi_0^2\sqrt{m_\phi^2-\omega_0^2}\int \mathrm{d}\rho\,\rho^2\left[-\frac{1}{2}f'^2 + \frac{1}{2}A'^2 + V_{\text{gauged}}(f,A)\right] \tag{2.24}$$

$$L_{\text{proca}} = 4\pi\Phi_0^2\sqrt{m_\phi^2-\omega_0^2}\int \mathrm{d}\rho\,\rho^2\left[-\frac{1}{2}f'^2 + \frac{1}{2}A'^2 + V_{\text{proca}}(f,A)\right] \tag{2.25}$$

2.6 Equations of motion and solutions

The core task in uncovering the identity of a particular Q-ball is to solve its differential equation(s). A Q-ball solution furnishes the complete function $f(\rho)$ for all points in space (as well as the function $A(\rho)$ for gauged and Proca Q-balls). Solutions also yield the size, energy, and charge of Q-balls. As earlier stated, there are unfortunately no known exact solutions for the coupled differential equations of Q-balls, so finding solutions becomes an exercise in two parts: (1) numerically solving the differential equations as closely as possible using `Mathematica` [19] and (2) using known limiting cases, e.g. "thin wall" Q-balls (c.f. Section 1.3), to approximate analytical solutions.

The basic equations of motion for the scalar and gauge fields of Q-balls are

$$f'' + \frac{2}{\rho}f' = -\frac{\partial V}{\partial f}, \qquad A'' + \frac{2}{\rho}A' = +\frac{\partial V}{\partial A}\,. \tag{2.26}$$

V is the relevant Q-ball potential from Eqs. (2.20), (2.21), and (2.22). Only the scalar field equation of motion applies in the global case.

Explicitly, these equations are

$$f'' + \frac{2}{\rho} f' = -\frac{\partial V_{\text{global}}}{\partial f} = \frac{1}{\Phi_0^2 (m_\phi^2 - \omega_0^2)^2} \frac{\mathrm{d}U}{\mathrm{d}f} - \Omega_G^2 f \qquad \textbf{Global case} \qquad (2.27)$$

$$f'' + \frac{2}{\rho} f' = -\frac{\partial V_{\text{gauged}}}{\partial f} = \frac{1}{\Phi_0^2 (m_\phi^2 - \omega_0^2)^2} \frac{\mathrm{d}U}{\mathrm{d}f} - (\Omega - \alpha A)^2 f \qquad (2.28)$$

$$A'' + \frac{2}{\rho} A' = +\frac{\partial V_{\text{gauged}}}{\partial A} = \alpha f^2 (\alpha A - \Omega) \qquad \textbf{Gauged case} \qquad (2.29)$$

$$f'' + \frac{2}{\rho} f' = -\frac{\partial V_{\text{proca}}}{\partial f} = \frac{1}{\Phi_0^2 (m_\phi^2 - \omega_0^2)^2} \frac{\mathrm{d}U}{\mathrm{d}f} - (\Omega - \alpha A)^2 f \qquad (2.30)$$

$$A'' + \frac{2}{\rho} A' = +\frac{\partial V_{\text{proca}}}{\partial A} = \alpha f^2 (\alpha A - \Omega) + M^2 A \qquad \textbf{Proca case} \qquad (2.31)$$

They are solved subject to boundary conditions on f, f', A, and A', which reflect constraints on physically realizable Q-balls.

$$\lim_{\rho \to 0} f' = \lim_{\rho \to \infty} f = \lim_{\rho \to 0} A' = \lim_{\rho \to \infty} A = 0 \qquad (2.32)$$

The boundary conditions on the field derivatives prevents solutions that are singular at $\rho = 0$, while the boundary conditions on the fields at infinity enforce localized solutions.

2.7 Radius

The three defining features of Q-balls are their size (i.e. radius), charge, and energy. Although there is some ambiguity in defining the radius, the midpoint of the transition region (see the profiles in, e.g., Fig. 2.1) is a logical choice. Since the transition region is well-approximated by an exponential (discussed in Section 3.1.2), this translates mathematically to $f''(R^*) = 0$. R^* is the dimensionless Q-ball radius, defined in (2.16) (see also the footnote in Section 2.5).

A key observation from global Q-balls is that the scalar profile f is determined exclusively by κ; see Section 2.11 for a discussion of this phenomenon. Since the Q-ball radius is exclusively determined by the scalar profile, there is clearly a correspondence between R^* and κ. This relationship is derived and refined in Section 3.1.5 and is a defining result of this work.

2.8 Energy and charge

Q-balls have a conserved charge, Q, which is the spatial integral over the time component of the conserved, scalar Noether current.

$$Q \equiv i \int \mathrm{d}^3x \left(\phi^* \partial^0 \phi - \phi \partial^0 \phi^*\right) \tag{2.33}$$

The energy of Q-balls, E, is obtained from their Hamiltonian.

$$E = 4\pi\Phi_0^2 \sqrt{m_\phi^2 - \omega_0^2} \int \mathrm{d}\rho\, \rho^2 \left[\frac{1}{2} f'^2 \left\{+\frac{1}{2}A'^2\right\} + \frac{1}{2} f^2 (\Omega - \alpha A)^2 + \frac{U(f)}{\Phi_0^2 (m_\phi^2 - \omega_0^2)^2} \left\{+\frac{M^2}{2}A^2\right\}\right] \tag{2.34}$$

The Hamiltonian requires the original potentials $U(f)$ in the Lagrangian forms (2.17), (2.18), and (2.19) (as opposed to negating the dimensionless potentials $V(f)$ and $V(f,A)$ in the di-

mensionless Lagrangians (2.23), (2.24), and (2.25)). The braced terms are excluded in the global case and included in the gauged $\left(\left\{+\frac{1}{2}A'^2\right\}\right)$ and Proca $\left(\left\{+\frac{1}{2}A'^2\right\},\ \left\{+\frac{M^2}{2}A^2\right\}\right)$ cases.

More detailed charge and energy expressions, derivations, and discussions for each type of Q-ball can be found in Sections 3.1.4 (global), 3.2.3 (gauged), and 3.3.3 (Proca).

2.9 Stability

There are several criteria for Q-ball stability (discussed more extensively in [8, 27, 5, 28]), but the most straightforward and applicable criterion for this work is that the energy of a stable Q-ball must be less than the mass of Q free scalars:

$$E < m_\phi Q\ . \tag{2.35}$$

In other words, it must be energetically preferable for Q-ball to stay clumped together than to break apart. (See Section 2.12 for a discussion of how the relationship (2.64) $\mathrm{d}E/\mathrm{d}\omega = \omega\ \mathrm{d}Q/\mathrm{d}\omega$ relates to this energy-stability bound.)

The equations of motions (2.26) for Q-balls can be solved even for Q-balls that violate Eq. (2.35). These Q-balls are marked as "unstable" in all figures. While unstable Q-balls are not prohibited from forming, generally such Q-balls would be short-lived.

It is also worth noting that the regions of stability can change significantly with the type of potential that produces the Q-balls [29]. For instance, in Ref. [9] is is shown that the Q-balls which arise from a potential with a cubic term can be stable even for $\omega \to m_\phi$. However, such potentials will not be considered here, and the condition (2.35) will be the determinant of stability for all Q-balls.

2.10 Classical field dynamics

While Q-balls are a phenomenologically new class of particle, their dynamics can be understood with the simple analogy of a particle (the scalar and, later, gauge profiles) traversing a path under the influence of the potential $V(f)$ or $V(f,A)$. This puts the differential equations of (2.26) on more familiar footing. This picture is attributable to Coleman. [2]

Consider a particle satisfying the equation

$$\ddot{x} + \frac{2}{t}\dot{x} + \frac{\mathrm{d}V}{\mathrm{d}x} = 0\,, \tag{2.36}$$

where dots denote time derivatives. This is a particle moving in a potential $V(x)$ and experiencing time-dependent friction. In this analogy, x corresponds to the scalar profiles f and time t to the radial coordinate ρ. The condition that $f'(0) = 0$ is analogous to $\dot{x}(0) = 0$, meaning that the particle starts at rest, while the condition $f(\infty) = 0$ corresponds to $x(\infty) = 0$, which means the particle must end up at the local maximum at $x = 0$. Thus, the profiles for f correspond to the trajectories of a particle whose friction decreases with time, rolling down a potential and ending up at the top of a local peak. This familiar mechanical analogue is a helpful way to conceptualize the dynamics of Q-ball profiles.

This analogy immediately makes clear the range of κ and its connection to the existence criteria of Eq. (2.4). For $\kappa \geq 1$, $f = 0$ is not a maximum, so the particle can only stop there if (1) it begins there at rest, which is a trivial solution, or (2) it oscillates about the minimum at $f = 0$, which would imply periods with $f < 0$. On the other hand, for $\kappa < 0$, $f = 0$ is higher than any other maxima, and so nothing can roll onto it. If $\kappa = 0$, then the only point on the other hill which is not lower than $f = 0$ is exactly at the maximum $f = f_+$, and the particle never rolls from this equilibrium point. Hence, $0 < \kappa < 1$, which is equivalent to $\omega_0 < \omega < m_\phi$.

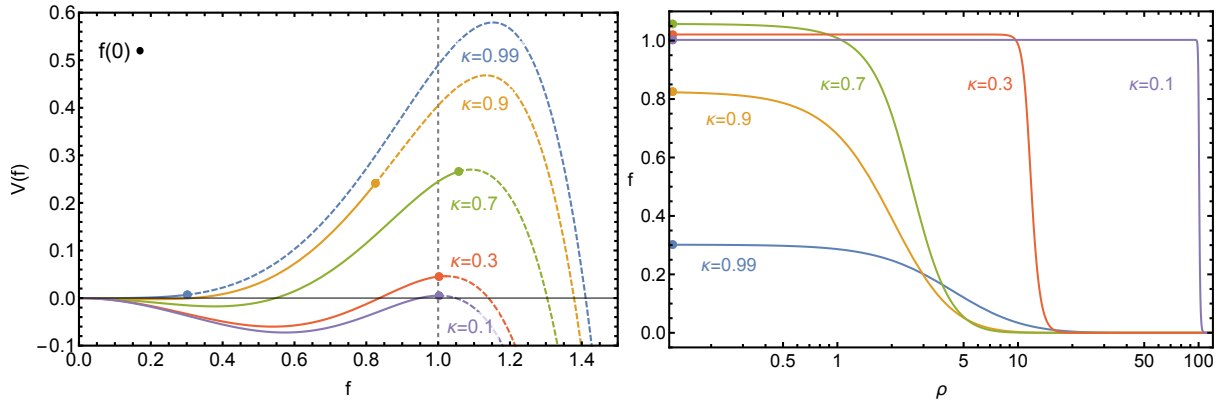

Figure 2.1: *Left:* the effective, global Q-ball potential $V(f)$. *Right:* global Q-ball profiles for various κ. Dots on the potential plot are the points $f(0)$ from which the scalar profile starts its trajectory. The solid curves on the potential plot are the paths the scalar field f takes for associated κ, while the rest of the (untraveled) potential is filled out with dashed lines. The vertical dashed line is the location of the maximum when $\kappa = 0$. The associated spatial profiles for the scalar trajectories shown in the potential plot are given in the f vs. ρ plot on the right.

In the global case, the Q-ball differential equation is Eq. (2.27) with associated potential

$$V_{\text{global}}(f) = \frac{1}{2} f^2 \left[\kappa^2 - \left(1 - f^2\right)^2\right] \tag{2.37}$$

The extrema of $V_{\text{global}}(f)$ are at $f = 0$ and

$$f_{\pm}^2 = \frac{1}{3}\left(2 \pm \sqrt{1 + 3\kappa^2}\right). \tag{2.38}$$

f_+ is always a maximum, while f_- is a minimum for $\kappa < 1$ (or $\omega < m_\phi$), which is necessarily true for global Q-balls (c.f. Section 2.3). The center of the potential, $f = 0$, is a maximum for $\kappa < 1$. When $\kappa = 1$, $f = 0$ becomes a minimum, and the potential becomes nearly flat at $f = 0$. These potential dynamics are illustrated in the left panel of Fig. 2.1.

In the analogy of a particle moving through a potential, Eq. (2.27) is the equation of motion for the particle moving through a potential subject to friction. The $2f'/\rho$ term is this "friction"

term. Were it not for this "friction", the equation of motion could be written as

$$f'' + \frac{\mathrm{d}V}{\mathrm{d}f} = \frac{1}{f'}\frac{\mathrm{d}}{\mathrm{d}\rho}\left(\frac{1}{2}f'^2 + V(f)\right) = 0\,. \tag{2.39}$$

The quantity in parentheses may be identified as a conserved, energy-like term [30] in this analogy

$$\mathcal{E} = \frac{1}{2}f'^2 + V(f)\,. \tag{2.40}$$

When evaluated at $\rho = 0$, this total "energy" $\mathcal{E} = 0$. $\mathcal{E}$ is not conserved when the friction term $2f'/\rho$ is included; rather, energy is lost to the presence of this friction.

$$\frac{\mathrm{d}\mathcal{E}}{\mathrm{d}\rho} = f'\left(f'' + \frac{\mathrm{d}V}{\mathrm{d}f}\right) = -\frac{2}{\rho}f'^2 \tag{2.41}$$

In the analogy of the scalar profile of a Q-ball as a particle moving along a trajectory, the particle starts at $f = f(0)$ with $f' = 0$ and ends at $f = 0$ with $f' = 0$. Integrating the friction term over this trajectory gives the energy difference between the starting and ending potential peaks. [29] Recall that $V(0) = 0$.

$$V(f(0)) = 2\int_0^\infty \mathrm{d}\rho\,\frac{f'^2}{\rho}. \tag{2.42}$$

The height difference between the two potential peaks (see Fig. 2.1 for a visual representation) is then equal to the energy lost due to friction.

This familiar language of a particle "losing energy" over a "trajectory" provides an intuitive, qualitative understanding of the dynamics of the radial, scalar profile $f(\rho)$ of a Q-ball. Trajectories that begin near $V(f_+) \approx 0$ (e.g. the red and purple profiles of Fig. 2.1) transition to the true vacuum, $f = 0$, without much friction. At small ρ, the friction term dominates over the tendency to begin rolling, as the energy difference between f_+ and $f = 0$ is small.

The transition begins when the friction term is suppressed by large ρ, after which it proceeds quickly, unhindered by friction. This gives the sharp, step-like profiles in the right panel. These trajectories correspond to smaller κ.

The extreme limit of the low-friction case is the thin-wall limit, in which $\rho \to \infty$ and $\kappa \to 0$ imply $V(0) = V(f_+) = 0$ and $2f'/\rho \to 0$. The statement that there is no friction in the thin-wall limit is equivalent to the statement that the two maxima $V(0)$ and $V(f_+)$ have equal heights, thus no energy can be lost along the particle's path. The profile of the thin-wall limit also represents the extreme of the small-κ profiles depicted in Fig. 2.1: it is a perfect step function without any smoothing or width attributable to the presence of friction. This is, of course, the profile (1.1) from Section 1.3.

Conversely, as the energy difference between $V(f_+)$ and $V(0) = 0$ increases, the friction cannot completely compensate for the change. In these trajectories, $f(0)$ falls progressively further below f_+, and these particles begin their transitions progressively "sooner," i.e. at smaller ρ. The earlier transitions leads to smaller radii, while the slowing effect from more potent friction leads to softer edges.

For large enough κ, the trajectory must start so far below the first maximum that there is very little rapid motion during the transition. The particle takes a long time rolling to f=0, and the soft edge of the Q-ball continues to widen until at $\kappa = 1$ the trajectory begins and ends at rest at $f = 0$. In other words, as κ continues to increase, the scalar profiles of Fig. 2.1 continue to flatten and their transition regions continue to widen, until at $\kappa = 1$ they are completely flat at $f = 0$.

Fig. 2.2 provides another perspective for the "timing" of the transition in ρ. Black points on the potential mark values of integer ρ. Dots for small ρ ($\rho < 21$) collect at $V(f(0)) \sim 0.02$, while dots for large ρ ($\rho > 24$) collect at $V(0) = 0$. The four dots in between ($21 \geq \rho \leq 24$) illustrate the rapid change in f over a small region in ρ. The profile f_G can be seen in Fig. 2.3.

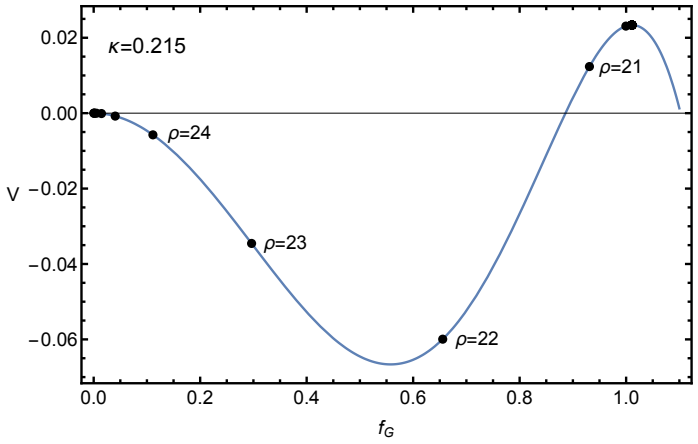

Figure 2.2: ρ dependence of effective, global potential $V_{\text{global}}(f)$. The effective potential $V(f)$ is dependent on the scalar profile f, which is itself dependent on the radial coordinate ρ. The black points illustrate this implicit ρ dependence for integer values of ρ in $\rho \in [0,30]$. They also show that motion along the potential happens over a relatively small region of ρ; this is the transition region. The profile spends most of its "time" on the local maxima of $V(f)$.

The gauged case is similar, although its potential includes the new gauge field, A, in addition to the scalar field f.

$$V_{\text{gauged}}(f,A) = \frac{1}{2} f^2 \left[\kappa^2 + \alpha A(\alpha A - 2\Omega) - \left(1 - f^2\right)^2\right]. \tag{2.43}$$

For constant A, the potential in $f \geq 0$ has three extrema, one at $f = 0$ and the other two at

$$f_\pm^2 = \frac{1}{3}\left(2 \pm \sqrt{1 + 3\kappa^2 - 3\alpha A(2\Omega - \alpha A)}\right) . \tag{2.44}$$

f_+ is a maximum and f_- a minimum. The global case is a limiting case of $V_{\text{gauged}}(f,A)$ with $A = 0$.

For constant f, the potential for A has one extremum at

$$A_{\text{max}} = \frac{\Omega}{\alpha} . \tag{2.45}$$

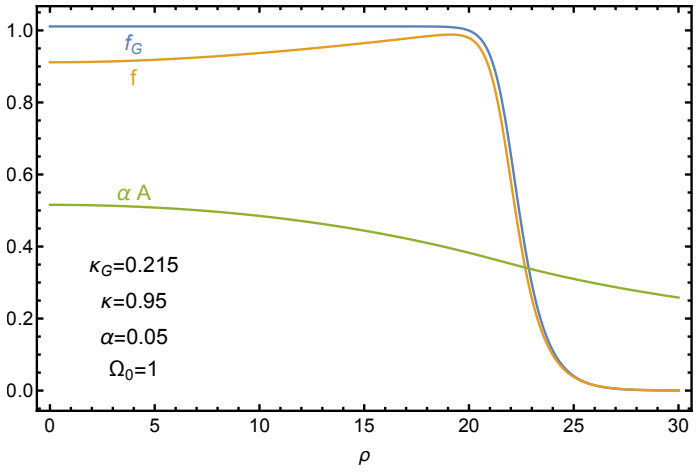

Figure 2.3: Scalar and gauge field profiles for one potential parameterization. The two scalar profiles for $R^* \approx 22$ are shown – the global scalar profile (f_G) in blue, and the gauged scalar profile (f) in orange. This shows visually the correction provided by the mapping of Eq. (3.60) for correspondent radii.

The primary difference between the global and gauged cases is that the evolving gauge field A causes the effective potential for the scalar to change with ρ. This is illustrated in the left panel of Fig. 2.4. The gauge field evolution changes the location and height of the maximum at f_+. The scalar continues to follow this maximum until a certain point, at which time it transitions quickly to the other maximum at $f = 0$.

Of course, this can only occur when f_+ exists, which translates to a requirement that Eq. (2.44) is real. This implies

$$\frac{1}{3} + \kappa^2 \geq \alpha A(2\Omega - \alpha A)\,. \tag{2.46}$$

This condition is automatically satisfied in the global case, i.e. $\alpha \to 0$. In the gauged case, it restricts αA to two possible regions:

$$\alpha A \leq \Omega - \sqrt{\Omega_0^2 - \frac{1}{3}} \quad \text{or} \quad \alpha A \geq \Omega + \sqrt{\Omega_0^2 - \frac{1}{3}}\,. \tag{2.47}$$

The second inequality is not compatible with Q-ball solutions; however, the first inequality provides an upper bound on αA when $\Omega_0 \geq 1/\sqrt{3}$.

Like the global case, initial values of the fields can be determined using energy principles. Neglecting the friction terms, the equations of motion in the gauged case (from Eqs. (2.28), (2.29), (2.21)) are

$$f'' + \frac{\partial V_{\text{gauged}}}{\partial f} = 0, \quad A'' - \frac{\partial V_{\text{gauged}}}{\partial A} = 0\,. \tag{2.48}$$

The energy-like quantity $\mathcal{E}$

$$\mathcal{E} = \frac{1}{2}f'^2 - \frac{1}{2}A'^2 + V_{\text{gauged}}(f, A) \tag{2.49}$$

is conserved as a function of ρ:

$$\frac{\mathrm{d}\mathcal{E}}{\mathrm{d}\rho} = f'\left(f'' + \frac{\partial V_{\text{gauged}}}{\partial f}\right) - A'\left(A'' - \frac{\partial V_{\text{gauged}}}{\partial A}\right) = 0\,. \tag{2.50}$$

The inclusion of friction results in a new differential equation that reflects the true dynamics of the gauged Q-ball system.

$$\frac{\mathrm{d}\mathcal{E}}{\mathrm{d}\rho} = -\frac{2}{\rho}\left(f'^2 - A'^2\right) \tag{2.51}$$

Eq. (2.51) (along with Eq. (3.74) of Chapter 3) indicates that f' and A' affect the energy differently. The f profile behaves according to one's usual intuition, but the A profile's dynamics are backwards due to its opposite-sign kinetic term. It falls up rather than down. As a result, while Eq. (2.45) is a *minimum* in V, this opposite-sign behavior drives A *uphill* either toward $A = 0$ or $A \to \infty$. If A is larger than A_{max}, it diverges as $\rho \to \infty$, which violates the Q-ball boundary conditions (and is obviously physically problematic). This implies a new Q-ball

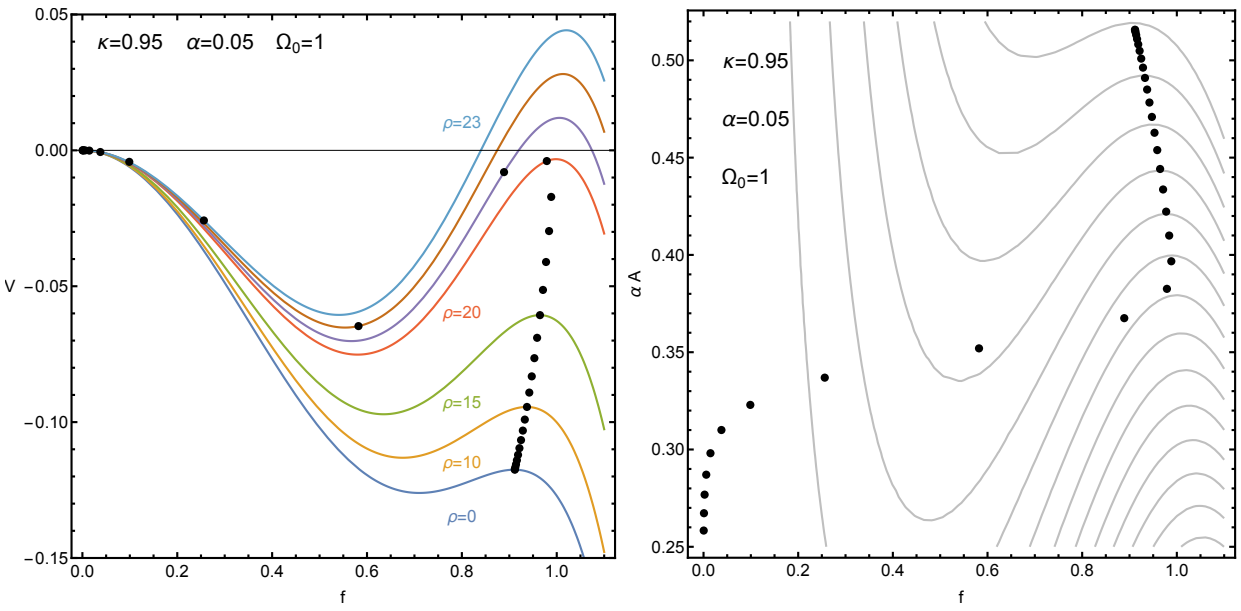

Figure 2.4: *Left:* Evolution of $V_{\text{gauged}}(f)$ with ρ. *Right:* Contour plot of $V_{\text{gauged}}(f,A)$. Black points are the values of the gauged Q-ball profiles for integer values of $\rho \in [0,30]$. The left panel shows how the dynamics of the gauge field A work to drive more energy into the scalar potential for small values of ρ to enable a transition once f_+ approaches $V_{\text{gauged}}(f_+) = 0$. The right panel illustrates the relative constancy of A during the transition in f that enables the mapping of Eq. (3.60).

constraint, $\Omega - \alpha A > 0$, with two consequences for Q-ball dynamics. First, because the right-hand side of the A equation of motion

$$A'' + \frac{2}{\rho}A' = -\alpha f^2(\Omega - A\alpha), \tag{2.52}$$

is always negative, A is monotonically decreasing for Q-ball solutions [7]. Second, as the system evolves, the negative term under the square-root in Eq. (2.44) becomes smaller and the value of f_+ grows. As a result, for some solutions, such as the one shown in Fig. 2.4, the "force" from the A gradient pushes f uphill toward this growing f_+. In other words, the scalar and gauge field profiles influence each other's behavior, and for certain gauged Q-ball trajectories the A field has the ability to overpower and reverse the expected behavior of the scalar field.

While the gauge field does influence the overall system dynamics and generate novel features of gauged Q-balls compared to global Q-balls, the gauge field has a relatively minor effect in

the region of the scalar field transition, where f goes from ~ 1 to ~ 0. This can be seen visually in the right panel of Fig. 2.4. The small contribution from A in this region suggests a connection to the purely scalar transition region of *global* Q-balls, for which the transition profile is shown in Section 3.1 to be an excellent overall fit for global Q-ball dynamics. The resulting "mapping" is shown to be a key feature of both the gauged and Proca cases in Sections 3.2.1 and 3.3.2, respectively.

The Proca case proceeds similarly to the global and gauged cases above. The equations of motion of the Proca case, without friction terms, are ((2.30), (2.31), (2.22))

$$f'' + \frac{\partial V_{\text{proca}}}{\partial f} = 0, \quad A'' - \frac{\partial V_{\text{proca}}}{\partial A} = 0. \tag{2.53}$$

The conserved "energy" quantity is $\mathcal{E}$.

$$\mathcal{E} = \frac{1}{2} f'^2 - \frac{1}{2} A'^2 + V_{\text{proca}}(f, A), \tag{2.54}$$

$$\frac{\mathrm{d}\mathcal{E}}{\mathrm{d}\rho} = f' \left(f'' + \frac{\partial V_{\text{proca}}}{\partial f} \right) - A' \left(A'' - \frac{\partial V_{\text{proca}}}{\partial A} \right) = 0. \tag{2.55}$$

Reintroducing friction gives

$$\frac{\mathrm{d}\mathcal{E}}{\mathrm{d}\rho} = -\frac{2}{\rho} \left(f'^2 - A'^2 \right), \tag{2.56}$$

which can be integrated along the trajectory to find the relative height of the potential at $f(0), A(0)$.

$$V_{\text{proca}}(f(0), A(0)) = 2 \int_0^\infty \frac{\mathrm{d}\rho}{\rho} \left(f'^2 - A'^2 \right) \tag{2.57}$$

As with the gauged case, $f(\infty) = A(\infty) = 0$ and the derivatives of f and A vanish at both boundaries.

The first term in the integral (2.57) is the analogue of energy lost to friction along the trajectory as f rolls from $f(0)$ to $f = 0$. A has the opposite-sign behavior discussed for the gauge case above. Its dynamics are determined by $-V$, not V. Therefore any energy "loss" due to friction acting on A requires an opposite sign in the friction integral.

As above, constraints on the individual potentials of f and A can be determined when the other field is held constant. For constant f, the potential V for A has one extremum at

$$A_{\max} = \frac{\Omega\alpha f^2}{M^2 + f^2\alpha^2} \tag{2.58}$$

For $f \neq 0$ this is a minimum of V. From another perspective: because A behaves as if kinetic energy has the opposite sign, $A_{\max}$ is a maximum in $-V$. This dynamic drives A down the $-V$ hill away from $A_{\max}$. This implies that for Q-ball solutions, where f begins at a value near one, that A must take values below $A_{\max}$ and is subsequently driven to even smaller values.

For constant A, the potential in $f \geq 0$ has three extrema: one maximum at $f = 0$ and a minimum and maximum at

$$f_\pm^2 = \frac{1}{3}\left(2 \pm \sqrt{1 + 3\kappa^2 - 3\alpha A(2\Omega - \alpha A)}\right). \tag{2.59}$$

$f_\pm$ must be real for localized soliton solutions; this translates to a non-negative requirement for the term under the square root. As with the gauged case, the result is a constraint on the amplitude of the gauge field.

$$\alpha A \leq \Omega - \sqrt{\Omega_0^2 - 1/3} \tag{2.60}$$

This constraint is only relevant when $\Omega_0 \geq 1/\sqrt{3}$.

As the system evolves, i.e A shrinks, the term under the square-root in Eq. (2.59) is reduced according to $2\Omega - \alpha A > 0$, with the result that the peak in f grows. When f transitions to small values, $A_{\max}$ follows. This slows the motion of the particle as it approaches ($f = 0,\ A = 0$).

Fig. 2.5 illustrates two examples of Proca Q-ball profiles and trajectories. The left panel contains the scalar and gauge profiles of a "thick-wall" Q-ball, i.e. a Q-ball for which the transition happens relatively slowly and the transition region is radially stretched out as a result. Below the profiles on the left is a quantitative illustration of the qualitative particle trajectory analogy; the thick blue curve is the trajectory in $V_{\text{proca}}(f, A)$. The right panel contains scalar and gauge profiles and the potential trajectory of a more traditional, thin-wall Q-ball. The interplay of f_+ and $A_{\max}$ within the potential V_{proca} is shown with dotted blue and green lines, respectively.

In the thick wall case (left panel), the trajectory begins at $f \approx 1$, a little downhill from f_+. This causes f to roll to smaller values. The value of A is less than $A_{\max}$, so the particle rolls uphill toward smaller A. When f and A become small enough the trajectory crosses $A_{\max}$, at which point the gauge field mass begins to dominate the A evolution.

The thin-wall trajectory begins near the intersection of f_+ and $A_{\max}$. This is a point of unstable equilibrium and plays a role similar to a particle resting exactly at f_+ in the global Q-ball case. By beginning the evolution close and closer to the equilibrium point, the radius of the thin-wall Q-balls can increase without bound. The first stage of motion is dominated by A dynamics. The particle begins rolling and is pushed uphill in V to smaller values of A while following f_+ along the potential ridge. Eventually it enters the transition region, where the scalar f dynamics dominate and the system rapidly rolls to small values in f. Despite this dramatic motion, the effect of friction is still clear from the profiles in the right panel, which are noticeably stretched and smoothed from a pure step function. This friction acts to slow the particle. From a potential perspective, the particle is slowed by both being above $A_{\max}$ by the need to roll into a valley and back up a peak in V during the transition period. In the final period of motion, A dynamics again dominate to bring the trajectory to $f = 0, A = 0$.

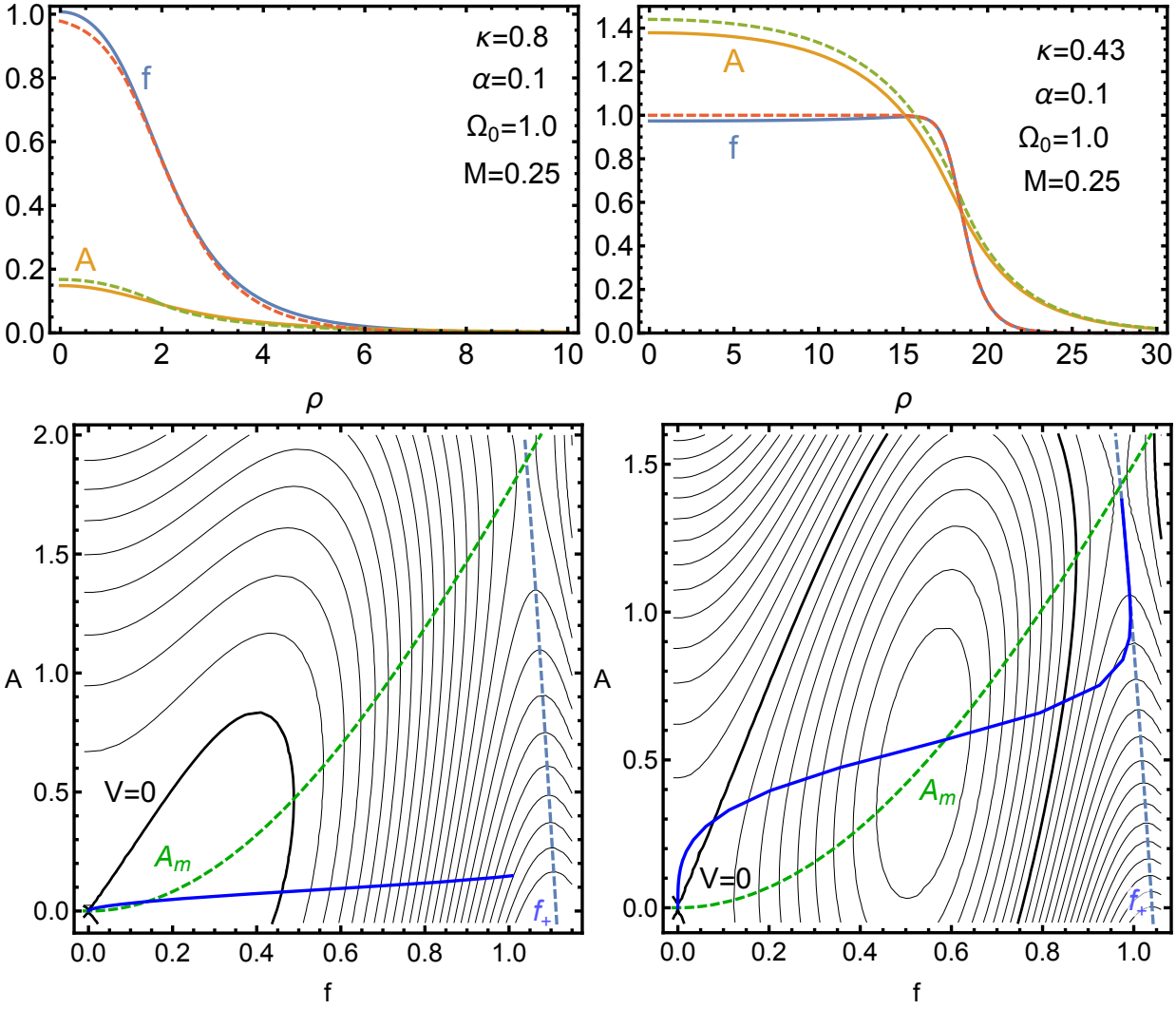

Figure 2.5: *Left:* Profiles and contour plots of a "thick-wall" Proca Q-ball. *Right:* Profiles and contour plots of a thin-wall Proca Q-ball. The top row shows both numeric (blue, orange curves) and approximated (red, green dashes) profiles for the scalar and gauge fields, respectively, of two sample Proca Q-balls. Approximations are taken from Eqs. (3.18) and (3.80). The bottom row contains the contour profiles for their associated potentials $V_{\text{proca}}(f,A)$. The actual trajectories in V_{proca} are blue curves. The f maxima f_+ (blue) and A maxima A_{max} (green) are shown with dashed lines.

2.11 κ dependence

A key result of this work is the observation that the scalar profile of Q-balls is determined exclusively by the dimensionless parameter κ (2.14):

$$\kappa^2 \equiv \frac{\omega^2 - \omega_0^2}{m_\phi^2 - \omega_0^2} \in (0,1]\,. \tag{2.61}$$

In the global case, the potential $V(f)$ is dependent exclusively on κ.

$$\begin{aligned} V_{\text{global}}(f,A) &= \frac{1}{2}f^2\Omega^2 - \frac{U(f)}{\Phi_0^2(m_\phi^2-\omega_0^2)^2} \\ &= \frac{1}{m_\phi^2-\omega_0^2}\left[\frac{1}{2}f^2\omega^2 - \frac{U(f)}{\phi_0^2}\right] \\ &= \frac{1}{m_\phi^2-\omega_0^2}\left[\frac{1}{2}f^2\omega^2 - \frac{1}{2}(m_\phi^2-\omega_0^2)f^2(1-f^2)^2 - \frac{1}{2}f^2\omega_0^2\right] \\ &= \frac{1}{2}f^2\kappa^2 - \frac{1}{2}f^2(1-f^2)^2 \end{aligned} \tag{2.62}$$

In the gauged case, the scalar profile also depends on a single parameter, κ_G, but via the mapping of Eq. (3.60).

$$\begin{aligned} V_{\text{gauged}}(f,A) &= \frac{1}{2}f^2(\Omega-\alpha A)^2 - \frac{U(f)}{\Phi_0^2(m_\phi^2-\omega_0^2)^2} \\ &= \frac{1}{2}f^2\Omega_G^2 - \frac{U(f)}{\Phi_0^2(m_\phi^2-\omega_0^2)^2} \\ &= \frac{1}{2}f^2\kappa_G^2 - \frac{1}{2}f^2(1-f^2)^2 \end{aligned} \tag{2.63}$$

Here $\kappa_G^2 \equiv \Omega_G^2 - \Omega_0^2$, and $\Omega_G \equiv \Omega - \alpha A$. There is also a correspondence between R^* and κ_G for gauged Q-balls, which is defined by the mapping (3.60).

2.12 ω as a chemical potential

Energy, charge, and frequency are related in Q-balls by the following expression, first noted in [8].[4]

$$\frac{\mathrm{d}E}{\mathrm{d}\omega} = \omega \frac{\mathrm{d}Q}{\mathrm{d}\omega} \tag{2.64}$$

Choosing $\omega > 0$ implies $Q > 0$ without loss of generality. In global Q-balls, Eq. (2.64) can be derived via Eqs. (3.29) and (3.31).

$$\begin{aligned}
\frac{\mathrm{d}E}{\mathrm{d}\omega} &= \omega \frac{\mathrm{d}Q}{\mathrm{d}\omega} + Q + 4\pi\phi_0^2 \int \mathrm{d}r\, r^2 \left[f' \frac{\mathrm{d}f'}{\mathrm{d}\omega} - \omega^2 f \frac{\mathrm{d}f}{\mathrm{d}\omega} - f^2 \omega + \frac{1}{\phi_0^2} \frac{\mathrm{d}U}{\mathrm{d}\omega} \right] \\
&= \omega \frac{\mathrm{d}Q}{\mathrm{d}\omega} + Q - Q + 4\pi\phi_0^2 \int \mathrm{d}r\, r^2 \left[-\frac{\mathrm{d}f}{\mathrm{d}\omega} \left(\frac{1}{\phi_0^2} \frac{\mathrm{d}U}{\mathrm{d}f} - \omega^2 f \right) - \omega^2 f \frac{\mathrm{d}f}{\mathrm{d}\omega} + \frac{1}{\phi_0^2} \frac{\mathrm{d}U}{\mathrm{d}\omega} \right] \\
&= \omega \frac{\mathrm{d}Q}{\mathrm{d}\omega}\,,
\end{aligned} \tag{2.65}$$

The first line uses the Hamiltonian for global Q-balls found in Eq. (3.31). The third term in the integral on the first line is Q (c.f. Eq. (3.29)), which can be pulled out of the expression. The first term is reexpressed using integration by parts and the scalar equation of motion (2.27).

For $\mathrm{d}Q/\mathrm{d}\omega \neq 0$, Eq. (2.64) implies $\mathrm{d}E/\mathrm{d}Q = \omega$ — in other words, ω behaves like a chemical potential. That is, ω determines how the energy changes when a particle of charge Q is added or removed from the Q-ball. When $\mathrm{d}Q/\mathrm{d}\omega > 0$, it is energetically favorable for given Q-ball to shed particles to lower its energy; this condition is sometimes used to determine if a given Q-ball is stable. In the opposite case, $\mathrm{d}Q/\mathrm{d}\omega < 0$, it is energetically favorable for the Q-ball to accrete particles.

[4] The relation was derived in [8] for Q-balls in 3 spatial dimensions rather than 3+1 dimensions as here and in Coleman's work [2]. As the Q-balls here depend on time only through an internal phase, the 3 dimensional relationship still applies with no concerns.

Gauged Q-balls are shown to obey this relationship in [31]. The proof that (2.64) continues to hold for the Proca case can be found in Section 3.3.4.

Chapter 3

Analytic predictions

Although exact solutions to the Q-ball equations of motion in Section 2.6 are not accessible analytically, excellent approximations are found here using Coleman's "thin wall" ansatz (c.f. Section 1.3) as a starting point.

This chapter treats global, gauged, and Proca Q-balls in their own sections. Each new case layers complexity upon the previous to arrive at its approximations.

3.1 Global Q-balls

As detailed in Section 1.3, Coleman [2] proposes that very large, global Q-balls in the limit $\kappa \to 0,\ \omega \to \omega_0$, and $R \to \infty$ have a step-function scalar profile $f(\rho)$:

$$f(\rho) = \begin{cases} 1\,, & \rho < R^*\,, \\ 0\,, & \rho > R^*\,, \end{cases} \tag{3.1}$$

This ansatz is predicated on the notion that the "transition region" – i.e. the exterior "crust" of the Q-ball which functions as an interpolation zone between the interior part of the Q-ball and the space exterior to the Q-ball – is very narrow compared to radius of the Q-ball itself. This is helpful in allowing the prediction of a number of quantities, including Q and E, that would be very complex to obtain outside of the thin-wall limit.

3.1.1 Expanding the thin-wall ansatz

One might hope that these approximations hold in the not-quite-so-thin-wall limit as well, i.e. $\omega \gtrsim \omega_0$, in which case Q (1.2) and E (1.3) become

$$Q = \frac{4\pi}{3}\left(\frac{R^*}{\sqrt{m_\phi^2 - \omega_0^2}}\right)^3 \phi_0^2\,\omega, \quad E = \omega Q + \frac{\pi\phi_0^2}{3\sqrt{m_\phi^2 - \omega_0^2}}\,R^{*2}\,. \tag{3.2}$$

If these approximations are to be compared to numerical results, it must also be known how R^* depends on ω (or equivalently on κ). Fortunately, an exact relation that will be helpful in this regard has already been derived in Eq. (2.64),

$$\frac{\mathrm{d}E}{\mathrm{d}R^*} = \omega(R^*)\frac{\mathrm{d}Q}{\mathrm{d}R^*}. \tag{3.3}$$

In concert with Eq. (3.2), an R^* - κ relationship can be determined away from the thin-wall limit. Substituting E from Eq. (3.2), the left-hand side of Eq. (3.3) becomes

$$\begin{aligned}\frac{\mathrm{d}E}{\mathrm{d}R^*} &= \omega(R^*)\frac{\mathrm{d}Q}{\mathrm{d}R^*} + Q\frac{\mathrm{d}\omega}{\mathrm{d}R^*} + \frac{2\pi\phi_0^2}{3\sqrt{m_\phi^2 - \omega_0^2}}\,R^* \\ &= \omega(R^*)\frac{\mathrm{d}Q}{\mathrm{d}R^*} + \frac{4\pi}{3}\left(\frac{R^*}{\sqrt{m_\phi^2 - \omega_0^2}}\right)^3 \phi_0^2\omega(R^*)\frac{\mathrm{d}\omega}{\mathrm{d}R^*} + \frac{2\pi\phi_0^2}{3\sqrt{m_\phi^2 - \omega_0^2}}\,R^*\,.\end{aligned} \tag{3.4}$$

This leaves a differential equation for ω,

$$\omega \frac{\mathrm{d}\omega}{\mathrm{d}R^*} = -\frac{m_\phi^2 - \omega_0^2}{2R^{*2}} \,. \tag{3.5}$$

It can be integrated in the thin-wall limit, with $\omega = \omega_0$ and $R^* = \infty$, then repurposed with general ω and R^* to find

$$R^* = \frac{m_\phi^2 - \omega_0^2}{\omega^2 - \omega_0^2} = \frac{1}{\kappa^2} \,. \tag{3.6}$$

Eq. (3.6) gives the relationship between κ^2, which determines the potential, and R^*, which is the Q-ball size, to leading order. Eq. (3.6) is exact for very large R^* or very small κ but is also an excellent approximation away from the thin-wall limit; the accuracy can be seen visually in Fig. 3.1. Even for the largest κ (up to the limit of Q-ball stability) the deviations between the predictions of Eq. (3.6) and the true numerical values are only about 10%.

However, the agreement is not nearly as good in Q and E predictions, which contain powers of R^* that compound the deviations when Eq. (3.6) is substituted into Eq. (3.2). The resulting deviations from the numerical results can be as large as 50% for stable Q-balls. A better understanding of how κ and R^* are related would allow for more accuracy in the Q and E predictions. Refined predictions for $R^*(\kappa)$ can be found in Eqs. (3.52) and (3.53).

3.1.2 Three regions of a Q-ball: exterior, interior, and transition

To further continue moving beyond the thin-wall limit, a more physically accurate profile than the basic step function is needed. This requires separately treating each Q-ball region: the exterior, interior, and transition regions. In this section, κ will be kept general rather than assuming $\kappa \to 0$ from the thin-wall limit.

Far outside a Q-ball, when $\rho \gg R^*$, f trends to the vacuum, $f \sim 0$. In this region, the potential can be approximated a quadratic, which yields a differential equation for the exterior

$$\begin{aligned} 0 &= f'' + \frac{2}{\rho} f' + \left.\frac{\mathrm{d}V}{\mathrm{d}f}\right|_{f=0} + f \left.\frac{\mathrm{d}^2 V}{\mathrm{d}f^2}\right|_{f=0} + \dots \\ &\simeq f'' + \frac{2}{\rho} f' - (1-\kappa^2) f \,. \end{aligned} \tag{3.7}$$

In the last equation terms of order f^3 and higher are dropped as $f \ll 1$. Solving with the boundary condition $f(\infty) = 0$, the exterior solution $f_>$ is

$$f_> = \frac{c_>}{\rho} e^{-\sqrt{1-\kappa^2}\rho} \,. \tag{3.8}$$

$c_>$ is an integration constant. This exponential drop-off behavior applies to all Q-balls, but in the thin-wall regime κ can be taken as 0 in $f_>$.

In the interior of the Q-ball, there exists the opposite situation: for large enough Q-balls, the value of f is close to the maximum of the potential, $f \sim f_+$. Again approximating the potential as a quadratic, the f equation for the interior is

$$0 = f'' + \frac{2}{\rho} f' + \left.\frac{\mathrm{d}V}{\mathrm{d}f}\right|_{f=f_+} + (f - f_+) \left.\frac{\mathrm{d}^2 V}{\mathrm{d}f^2}\right|_{f=f_+} + \dots \tag{3.9}$$

$$\simeq f'' + \frac{2}{\rho} f' - \alpha^2 (f - f_+) \,. \tag{3.10}$$

Neglected terms are higher order in $(f - f_+)$, and α^2 is defined as

$$\alpha^2 \equiv \frac{4}{3}\left(1 + 3\kappa^2 + 2\sqrt{1+3\kappa^2}\right) = 4 + 8\kappa^2 - 3\kappa^4 + \mathcal{O}(\kappa^6) \,. \tag{3.11}$$

After enforcing the boundary condition $f'(0) = 0$, the solution $f_<$ in the Q-ball interior is

$$f_< = f_+ + c_< \frac{\sinh(\alpha\rho)}{\rho} \,. \tag{3.12}$$

$c_<$ is an integration constant. In the thin-wall regime, where κ is small, $\alpha = 2$ in $f_<$. This result agrees with earlier work by Paccetti Correia and Schmidt. [30]

The most interesting and difficult region is the transition region, which joins the interior and exterior. Expanding the potential around an extremum will not prove useful here. A more expedient strategy is to consider that the center of the transition region is where $\rho = R^*$. With this in mind, a coordinate $z = \rho - R^*$ allows a focus on the region around $z = 0$, which is by definition the transition region. The surface profile f_s describes the transition from one potential maximum to the other, so the full potential must be considered. Using this new coordinate, the differential equation (2.27) becomes

$$\frac{\mathrm{d}^2 f_s}{\mathrm{d}z^2} + \frac{2}{R^* + z}\frac{\mathrm{d}f_s}{\mathrm{d}z} + f_s\left[\kappa^2 - (1 - f_s^2)(1 - 3f_s^2)\right] = 0\,. \tag{3.13}$$

When $-z \ll R^*$, which is true for all but small Q-balls with wide transition regions (relative to their size), the second term can be neglected. In fact, since $(R^*)^{-1}$ is in general reliably small, the scalar profile can be expanded as a power series in $(R^*)^{-1}$:

$$f_s(z) = f_s^{(0)}(z) + (R^*)^{-1} f_s^{(1)}(z) + \ldots \tag{3.14}$$

Using the relation $\kappa^2 = (R^*)^{-1}$ from Eq. (3.6), to leading order the profile satisfies

$$\frac{\mathrm{d}^2 f_s^{(0)}}{\mathrm{d}z^2} = f_s^{(0)}\left[1 - (f_s^{(0)})^2\right]\left[1 - 3(f_s^{(0)})^2\right]. \tag{3.15}$$

Since there is no "friction" term in Eq. (3.15) (see Section 2.10 for a description of "friction" in this context), $\mathcal{E}$ of Eq. (2.40) is conserved. Further, since $f'(0) = V(0) = 0$ for Q-ball solutions, $\mathcal{E} = 0$. This insight simplifies the second-order differential equation (3.15) to an equivalent

first-order equation

$$\frac{\mathrm{d}f_s^{(0)}}{\mathrm{d}z} = \pm f_s^{(0)}\left(1 - f_s^{(0)2}\right) \ . \tag{3.16}$$

Direct integration yields the solution for the transition region.

$$f_s^{(0)}(z) = \left[1 + c_s e^{\pm 2z}\right]^{-1/2} \tag{3.17}$$

c_s is an integration constant. Note that because f_s is a monotonically decreasing function [7], the exponent must be positive.

The constant c_s is determined by requiring $f''(R^*) = 0$, which formally identifies R^* as the Q-ball radius. In its final form, the transition function (at leading order in $1/R^*$) is

$$f_t(\rho) = \frac{1}{\sqrt{1 + 2e^{2(\rho - R^*)}}} \ . \tag{3.18}$$

Interestingly, numerical studies (see, for instance, Figure 3.1 and Chapter 4) will show that this transition profile also provides excellent results outside of the transition region, and can be used as a proxy for the full profile in many cases. A similar profile to the transition profile (3.18) presented here is derived in [32] using the Bogomolny argument; the fact that Bogomolny methods produce such a similar result is a nod to Q-balls' solitonic nature, even though they do not possess a topological charge.

Further corrections in $(R^*)^{-1}$ can in principle be obtained by solving the higher-order equations that result from inserting the profile expansion of Eq. (3.14) into Eq. (3.13). In practice this is quite complex and not worthwhile when the leading order approximation is already so accurate.

3.1.3 Full global profile

The interior (3.12), exterior (3.8), and transition (3.18) region profiles in f found in above are

$$\begin{cases} f_< &= f_+ + c_< \frac{\sinh(\alpha\rho)}{\rho} \\ f_t &= \left[1 + 2e^{2(\rho - R^*)}\right]^{-1/2} \\ f_> &= \frac{c_>}{\rho} e^{-\sqrt{1-\kappa^2}\rho} \end{cases} \tag{3.19}$$

They need to be joined together for the full profile of a global Q-ball. The coefficients $c_<$ and $c_>$ in the interior and exterior solutions are determined by enforcing continuity of f and f' at the matching points.

These profiles were derived in the region $\kappa \sim 0$,[1] but some small adjustments will improve the profile away from this limit. In the thin-wall limit, the scalar field transitions from $f(0) = f_+ = 1$ and to $f = 0$ at large ρ. Away from this limit, it need not be the case that the maximum $f_+ = 1$. The scalar field will start at some value $f(0) \approx f_+$, which is near the maximum f_+, before transitioning to $f = 0$ at large ρ. Rescaling the transition profile by $f_+ = \frac{1}{3}\left(2 + \sqrt{1+3\kappa^2}\right)$ (Eq. (2.38)) accounts for this disparity. The three profiles then take the form

$$f(\rho) = f_+ \begin{cases} 1 - c_< \dfrac{\sinh(\alpha\rho)}{\rho} & \text{for } \rho < \rho_<, \\ \left[1 + 2e^{2(\rho - R^*)}\right]^{-1/2} & \text{for } \rho_< < \rho < \rho_>, \\ \dfrac{c_>}{\rho} e^{-\rho\sqrt{1-\kappa^2}} & \text{for } \rho_> < \rho\ . \end{cases} \tag{3.20}$$

[1] Additional improvements are possible via the introduction of more parameters into the profile and minimization of the resulting E for a fixed Q. This is not addressed further here.

$c_{<,>}$ and $\rho_{<,>}$ must be determined by requiring f and f' to be continuous at $\rho_{<,>}$. $\rho_<$ is determined by the equation

$$2\rho_< = \left(\sqrt{1+2e^{2(\rho_<-R^*)}}-1\right)\left(2+e^{-2(\rho_<-R^*)}\right)[\alpha\rho_<\coth(\alpha\rho_<)-1]\,. \tag{3.21}$$

This equation does not have a simple solution, but under the assumptions $\rho_< \ll R^*$ and $\alpha\rho_< \gg 1$ it becomes

$$\rho_< \approx \frac{1}{\alpha-2} \approx \frac{1}{2}R^*\,, \tag{3.22}$$

where the relationship $\kappa^2 = 1/R^*$ was also used. The constant $c_<$ takes the form

$$c_< = \frac{2e^{2(\rho_<-R^*)}\rho_<^2}{[\alpha\rho_<\cosh(\alpha\rho_<)-\sinh(\alpha\rho_<)][1+2e^{2(\rho_<-R^*)}]^{3/2}} \approx R^* e^{-2R^*}\,. \tag{3.23}$$

The insight of this result is that the interior solution joins the surface solution about halfway between the center of the Q-ball and the edge, and only for smaller R^* does the sinh term play a significant role. This also yields a prediction for the value of the profile in the center of the Q-ball.

$$f(0) = f_+(1-\alpha c_<) \tag{3.24}$$

This quantifies how the initial value of f on the potential is away from the maximum as R^* becomes smaller, but only by exponentially small amounts.

The matching condition for $\rho_>$ is

$$e^{-2(\rho_>-R^*)} = 2\left(\frac{\rho_>}{1+\rho_>\sqrt{1-\kappa^2}}-1\right), \tag{3.25}$$

which leads the approximate solution

$$\rho_> \approx 2R^* . \tag{3.26}$$

The integration constant $c_>$ follows as

$$c_> = \rho_> e^{\rho_>\sqrt{1-\kappa^2}} \left[1 + 2e^{2(\rho_> - R^*)}\right]^{-1/2} \approx \sqrt{2} R^* e^{R^*} . \tag{3.27}$$

Interestingly, the matching point to the exterior solution is well beyond R^*. This shows again that much of the full profile is well-approximated by the transition solution.

With these solutions for $c_{<,>}$ and $\rho_{<,>}$, the full profile is approximated as

$$f(\rho) = \frac{1}{3}\left(2 + \sqrt{1+3\kappa^2}\right) \begin{cases} 1 - R^* e^{-2R^*} \dfrac{\sinh(\alpha\rho)}{\rho} & \text{for } \rho < \frac{R^*}{2} , \\ \left[1 + 2e^{2(\rho - R^*)}\right]^{-1/2} & \text{for } \frac{R^*}{2} < \rho < 2R^* , \\ \dfrac{\sqrt{2} R^* e^{R^*}}{\rho} e^{-\rho\sqrt{1-\kappa^2}} & \text{for } 2R^* < \rho . \end{cases} \tag{3.28}$$

Figure 3.1 shows the accuracy of the full profile of Eq. (3.28) (using the improved $R^*(\kappa)$ from Eq. (3.52)) in comparison to exact (to machine precision) numeric solutions. Since the profile was derived using approximations from the thin-wall limit ($\kappa \to 0$), the agreement of the right panel ($\kappa = 0.1$) is better than the left panel ($\kappa = 0.8$); this is to be expected, although it is worth noting that the agreement in the left panel is still excellent. Substituting the exact numerical R^* (not pictured) results in per-mille level agreement for large R^*, underscoring that (1) the full profile of (3.28) performs superbly when precise values are available for R^* and (2) even better approximations for R^* are needed to improve analytic predictions further. Refinement of $R^*(\kappa)$ is addressed in Section 3.1.5.

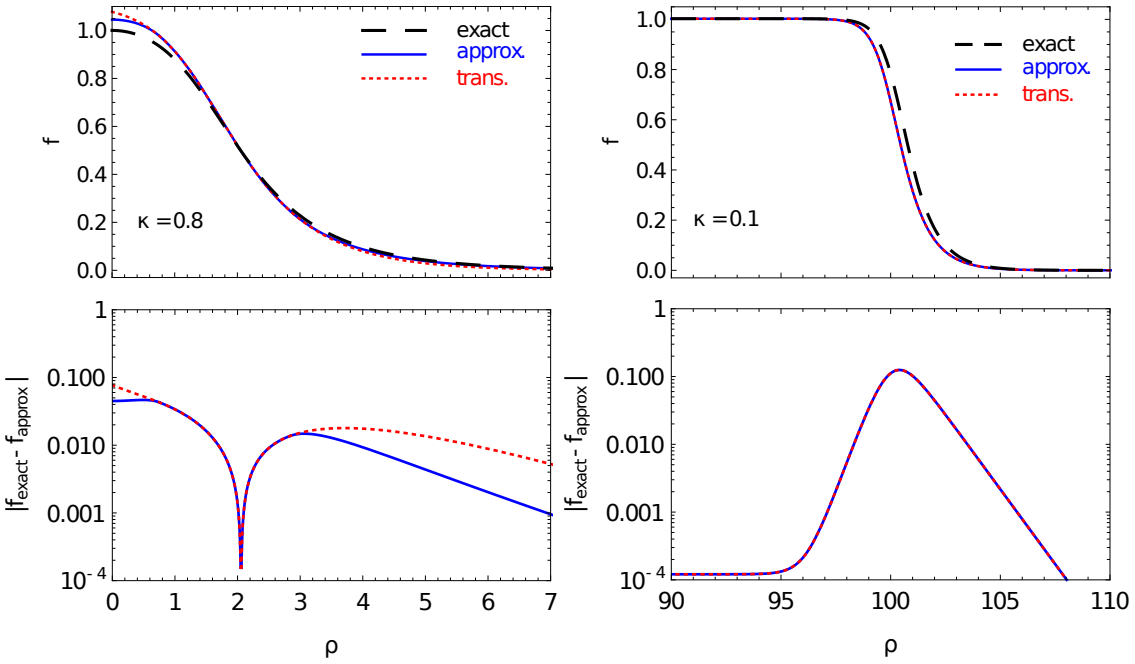

Figure 3.1: *Top:* Profiles $f(\rho)$ for $\kappa = 0.8$ (left) and $\kappa = 0.1$ (right). *Bottom:* Relative error between analytic approximations and exact results. These figures illustrate the excellent agreement between the full profile of Eq. (3.28) (blue lines) and exact numeric results (black dashed) for both small and large κ. The simpler transition profile (3.18), extended to cover the entire Q-ball range (red dotted), is shown to be nearly equally as good as the full profile, particularly for small κ.

Perhaps most amazing is the excellent approximation the transition function provides to the profile as a whole. The transition profile (3.18) is shown in Fig. 3.1 in red, with ρ now being allowed to run over the full region $0 \leq \rho < \infty$. For $\kappa \ll 1$ (right panel), this simplified profile is absolutely indistinguishable from the full profile (3.28), with agreement much better than the 0.01% level. Even for large κ, the agreement is still quite good, with the main divergences as $\rho \to 0$ and $\rho \to \infty$. (This is owing to the fact that the boundary condition $f'(0)$ can only be satisfied asymptotically as $R^{*}to0$.) While the full profile obviously provides the best description, the simplicity and relatively high accuracy of the transition profile (3.18) make it an extremely useful approximation when taken with Eq. (3.52).

3.1.4 Charge and energy

The program of this section will first be performed with dimensionful quantities (e.g. r, ω, ϕ_0) for clarity regarding their connection to the fundamental Q-ball potential (2.10) and Lagrangians (2.11), (2.12), and (2.13), then will be calculated again using the dimensionless quantities (ρ, Ω, Φ_0) employed throughout the rest of this work. The charge and energy sections for gauged (Section 3.2.3) and Proca (Section 3.3.3) Q-balls will reproduce only the dimensionless methods.

The charge of a Q-ball is the integral of the time component of the scalar current

$$Q \equiv i \int \mathrm{d}^3x \left(\phi \partial^0 \phi^* - \phi^* \partial^0 \phi\right) \tag{3.29}$$

$$= 4\pi\omega\phi_0^2 \int \mathrm{d}r\, r^2 f^2 \tag{3.30}$$

The energy is the Hamiltonian for global Q-balls.

$$\begin{aligned} E &= 4\pi\phi_0^2 \int \mathrm{d}r\, r^2 \left[\frac{1}{2}f'^2 + \frac{1}{2}f^2\omega^2 + \frac{U(f)}{\phi_0^2}\right] \\ &= \omega Q + 4\pi\phi_0^2 \int \mathrm{d}r\, r^2 \left[\frac{1}{2}f'^2 - \frac{1}{2}f^2\omega^2 + \frac{U(f)}{\phi_0^2}\right] \end{aligned} \tag{3.31}$$

A relationship between E and Q is already beginning to emerge. The expression for energy can be simplified further. A trick that takes advantage of a property of Lagrangians, suggested in [7], allows the energy integral (3.41) to be reexpressed without reference to the potential. When varied with respect to χ, which is subsequently set to $\chi = 1$, the Lagrangian (2.11) becomes

$$L_{\text{global}} = 4\pi\phi_0^2 \int \mathrm{d}r\; r^2 \left[-\chi \cdot \frac{1}{2}f'^2 + \chi^3 \cdot \frac{1}{2}f^2\omega^2 - \chi^3 \cdot \frac{U(f)}{\phi_0^2}\right]. \tag{3.32}$$

The χ-dependent Lagrangian has two parts: one that explicitly depends on χ and another in which a variation appears because ρ-dependent functions now depend on χ, e.g. $f(\rho) \to f(\rho\chi)$. This second collection of terms is simply the usual variation of the Lagrangian and vanishes by definition when $\chi = 1$.

The other part, with terms that depend explicitly on χ, must vanish when L_{global} is varied with respect to χ.

$$0 = \frac{\partial}{\partial\chi}\left\{4\pi\phi_0^2 \int \mathrm{d}r\; r^2 \left[-\chi \cdot \frac{1}{2}f'^2 + \chi^3 \cdot \frac{1}{2}f^2\omega^2 - \chi^3 \cdot \frac{U(f)}{\phi_0^2}\right]\right\}\Bigg|_{\chi=1} \tag{3.33}$$

$$0 = 4\pi\phi_0^2 \int \mathrm{d}r\; r^2 \left[-\frac{1}{2}f'^2 + \frac{3}{2}f^2\omega^2 - \frac{3U(f)}{\phi_0^2}\right] \tag{3.34}$$

$$0 = 4\pi\phi_0^2 \int \mathrm{d}r\; r^2 \left[\frac{1}{2}f'^2 - \frac{1}{2}f^2\omega^2 + \frac{U(f)}{\phi_0^2}\right] - \frac{4\pi}{3}\phi_0^2 \int \mathrm{d}r\; r^2 f'^2 \tag{3.35}$$

The second term in the last line can replace the first term where it appears in Eq. (3.41). This constraint is productive because it allows E to be formulated with fewer integrals and without

an explicit $U(f)$ dependence.

$$E = \omega Q + \frac{4\pi}{3}\phi_0^2 \int \mathrm{d}r\, r^2 f'^2 \,. \tag{3.36}$$

Additionally, it illustrates the relationship between E, ω, and Q – namely, that $E = \omega Q$ up to terms that depend on the derivative of $f(r)$. For large Q-balls, these terms are subleading and the relationship $E = \omega Q$ dominates.

This methodology can be revisited with dimensionless quantities. Q and E are straightforward mappings.

$$Q = 4\pi\Phi_0^2\,\Omega \int \mathrm{d}\rho\, \rho^2 f^2 \tag{3.37}$$

$$\begin{aligned} E &= 4\pi\Phi_0^2\sqrt{m_\phi^2-\omega_0^2}\int \mathrm{d}\rho\,\rho^2\left[\frac{1}{2}f'^2+\frac{1}{2}f^2\Omega^2+\frac{U(f)}{\Phi_0^2(m_\phi^2-\omega_0^2)^2}\right] \\ &= \sqrt{m_\phi^2-\omega_0^2}\left(\Omega Q + 4\pi\Phi_0^2\int \mathrm{d}\rho\,\rho^2\left[\frac{1}{2}f'^2-\frac{1}{2}f^2\Omega^2+\frac{U(f)}{\Phi_0^2(m_\phi^2-\omega_0^2)^2}\right]\right) \\ &= \sqrt{m_\phi^2-\omega_0^2}\left(\Omega Q + 4\pi\Phi_0^2\int \mathrm{d}\rho\,\rho^2\left[\frac{1}{2}f'^2-V_{\text{global}}(f)\right]\right) \end{aligned} \tag{3.38}$$

Rescaled by χ, the Lagrangian (2.23) becomes

$$L_{\text{global}} = 4\pi\Phi_0^2\sqrt{m_\phi^2-\omega_0^2}\int \mathrm{d}\rho\,\rho^2\chi\left[-\frac{1}{2}f'^2+\chi^2 V_{\text{global}}(f)\right]. \tag{3.39}$$

Variation provides the constraint

$$\begin{aligned} 0 &= 4\pi\Phi_0^2\int \mathrm{d}\rho\,\rho^2\left[-\frac{1}{2}f'^2+3V_{\text{global}}(f)\right] \\ &= 4\pi\Phi_0^2\int \mathrm{d}\rho\,\rho^2\left[\frac{1}{2}f'^2-V_{\text{global}}(f)\right]-\frac{4\pi}{3}\Phi_0^2\int \mathrm{d}\rho\,\rho^2 f'^2\,. \end{aligned} \tag{3.40}$$

When substituted into the previous expression for energy, this yields

$$E = \sqrt{m_\phi^2 - \omega_0^2}\left(\Omega Q + \frac{4\pi\Phi_0^2}{3}\int \mathrm{d}\rho\, \rho^2 f'^2\right) . \tag{3.41}$$

Using the thin-wall limit, the charge Q (3.37) and the energy E (3.41) can be expressed with forms that depend on R^*.

Using the profile (1.1), the charge can be directly integrated.

$$Q = \frac{4\pi}{3}\,\Phi_0^2\,\Omega\,R^{*3} \tag{3.42}$$

This is Coleman's thin-wall charge prediction (1.2). The Q-ball charge is $\Phi_0^2\,\Omega$ times the volume of the Q-ball when $\omega_0 > 0$.

The Q-ball energy E can be integrated using the fact that, in the thin-wall limit, f' is only nonzero at $\rho = R^*$.

$$\int_0^\infty \mathrm{d}\rho\, \rho^2 f'^2 = R^{*2}\int_0^1 \mathrm{d}f\, f' \tag{3.43}$$

Taking the thin-wall "energy" of (2.40) as conserved and zero gives another equality.

$$R^{*2}\int_0^1 \mathrm{d}f\, f' = \int_0^1 \mathrm{d}f\ \sqrt{-2V(f)}\Big|_{\kappa=0} \tag{3.44}$$

When integrated, this gives Coleman's thin-wall expression for the energy (1.3).

$$E = \sqrt{m_\phi^2 - \omega_0^2}\left(\Omega_0 Q + \frac{\pi}{3}\Phi_0^2\,R^{*2}\right) , \tag{3.45}$$

The first term is the volume contribution to the energy and the second is the surface contribution.

The improved profile of Eq. (3.28) additionally allows for further refinement of approximations for Q and E. The integrals of interest, $\int \mathrm{d}\rho\, \rho^2 f^2$ (c.f. Eq. (3.37)) and $\int \mathrm{d}\rho\, \rho^2 f'^2$ (c.f. Eq. (3.41)), can be performed analytically, although the expressions are long and not particularly useful. More practically, in the large R^* limit they read

$$\begin{aligned}\int \mathrm{d}\rho\, \rho^2 f^2 &\simeq \frac{f_+^2 R^{*3}}{3}\left(1-\frac{3\ln 2}{2R^*}+\frac{\pi^2+3\ln^2 2}{4R^{*2}}-\frac{(\pi^2+\ln^2 2)\ln 2}{8R^{*3}}\right),\\ \int \mathrm{d}\rho\, \rho^2 f'^2 &\simeq \frac{f_+^2 R^{*2}}{4}\left(1+\frac{1-\ln 2}{R^*}+\frac{\pi^2+(\ln 2-2)3\ln 2}{12R^{*2}}\right).\end{aligned} \tag{3.46}$$

Using Eq. (3.52), these expressions can also be expanded in in small κ.

The first integral is directly proportional to the dimensionful Q-ball volume $4\pi(m_\phi^2-\omega_0^2)^{-3/2}\int \mathrm{d}\rho\, \rho^2 f^2$. In the large R^* limit, the volume tends to $\simeq 4\pi R^{*3}/3$. This is immediately visible at leading order, since $f_+ = 1$ in the thin-wall limit.

After substitution of (3.46), the dimensionless charge and energy become

$$\begin{aligned}Q &\simeq \frac{4\pi}{3}\Phi_0^2\,\Omega\, R^{*3} f_+^2\left[1-\frac{3\ln 2}{2R^*}+\frac{\pi^2+3\ln^2 2}{4R^{*2}}-\frac{(\pi^2+\ln^2 2)\ln 2}{8R^{*3}}\right],\\ E &\simeq \sqrt{m_\phi^2-\omega_0^2}\left(\Omega Q+\frac{\pi}{3}\Phi_0^2 R^{*2} f_+^2\left[1+\frac{1-\ln 2}{R^*}+\frac{\pi^2+(\ln 2-2)3\ln 2}{12R^{*2}}\right]\right).\end{aligned} \tag{3.47}$$

Again, these reduce to the expressions in Eqs. (3.42) and (3.45) in the thin-wall limit (leading order with $f_+ = 1$). Together with Eq. (3.52), they furnish analytical approximations for Q and E as a function of the potential parameters. Other quantities, such as pressure, can be calculated straightforwardly; see e.g. [29]. The $1/R^*$ terms dramatically improve the fit for smaller Q-balls, as illustrated in the plots of Chapter 4.

For $\omega_0 > 0$, Q and E of (3.47) scale as $Q \propto E \propto R^3$ in the thin-wall limit. This is the proportionality expected for a lump of Q-matter. [2] However, special care must be exercised in the $\omega_0 = 0$ case, in which $\omega \propto 1/\sqrt{R}$ and thus $Q \propto R^{5/2}$ and $E \propto R^2$. [30] The lesson here is that even though the scalar profile f only depends on the parameter κ, the physical Q-ball properties must still be discussed in terms of the original Lagrangian parameters and, in particular, depend on ω_0.

How theoretically motivated are Q and E of Eq. (3.47)? Do they obey the relationship (2.64) $\mathrm{d}E/\mathrm{d}\omega = \omega\ \mathrm{d}Q/\mathrm{d}\omega$ (or, equivalently, $\mathrm{d}E/\mathrm{d}R^* = \omega(R^*)\ \mathrm{d}Q/\mathrm{d}R^*$ (3.3))?

To check, the refined $R^*(\kappa)$ can be inverted to determine $\omega(R^*)$. With this substitution, it turns out that $\mathrm{d}E/\mathrm{d}R^* = \omega(R^*)\ \mathrm{d}Q/\mathrm{d}R^*$ is valid up to terms of order $(R^*)^0$.

Instead of taking $R^*(\kappa)$ to be the fundamentally correct approximation, Q and E could be taken as exact, and then $\kappa(R^*)$ determined by Eq. (2.64). The resulting relationship is

$$\kappa^2 = \frac{1}{R^*} + \frac{1+\ln 16}{8R^{*2}} + \mathcal{O}\left(\frac{1}{R^{*3}}\right). \tag{3.48}$$

It isn't an improvement over Eq. (3.52), though, which will be used as the refined approximation for R^* where needed throughout this work.

3.1.5 R* – κ correspondence

R^*, the Q-ball radius, and κ, a dimensionless parameter that fully parameterizes the global scalar profile, have a leading-order relationship derived in Eq. (3.6). This section refines that relationship with higher-order corrections.

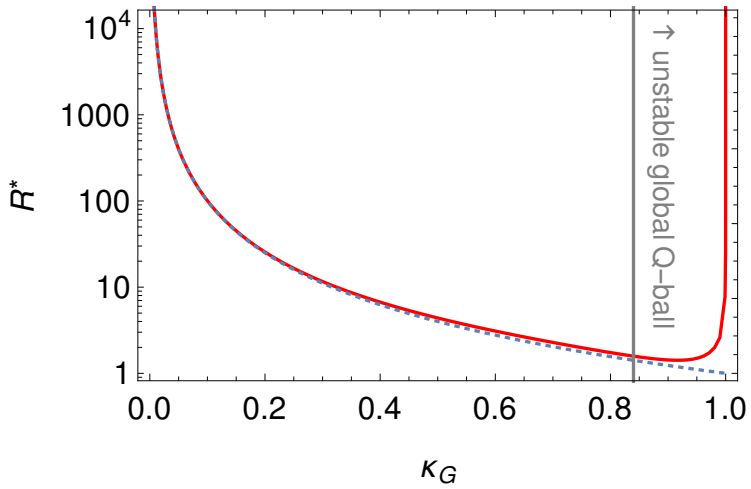

Figure 3.2: Accuracy of the first-order approximation $\kappa_G = 1/R^*$ (Eq. (3.6)) (blue dotted), for $\kappa_G = \sqrt{\Omega_G^2 - \Omega_0^2}$. Numeric results are in red. The first-order approximation is an excellent fit in the physically interesting region of stable Q-balls ($\kappa_G \lesssim 0.84$).

Refining the $R^* - \kappa$ correspondence starts with the work-energy integral of Eq. (2.42):

$$V(f(0)) = 2\int_0^\infty \frac{\mathrm{d}\rho}{\rho}(f')^2 \,. \tag{3.49}$$

For the full, global profile of Eq. (3.28), this integral must be evaluated piecewise over the three regions of f. The integrands of the interior and exterior regions are suppressed by factors of e^{-R^*} or more; this leaves only contributions from the simple transition function (3.18).

Working in the large R^* / small κ limit and utilizing the analytical approximations of Section 3.1.3, namely

$$f(0) \approx f_+ \,, \quad \rho_< \approx \frac{R^*}{2} \,, \quad \rho_> \approx 2R^* \,, \tag{3.50}$$

the friction-loss integral becomes

$$V(f_+) = 8f_+^2 \int_{R^*/2}^{2R^*} \frac{\mathrm{d}\rho}{\rho} \frac{e^{4(\rho - R^*)}}{[1 + 2e^{2(\rho - R^*)}]^3} = 8f_+^2 \int_{-R^*/2}^{R^*} \frac{\mathrm{d}z}{z + R^*} \frac{e^{4z}}{[1 + 2e^{2z}]^3} \,. \tag{3.51}$$

In the last equality, the coordinate $z = \rho - R^*$ of Section 3.1.3 is substituted for ρ. The integrand is sharply peaked at $z = 0$, allowing the expansion of $(z + R^*)^{-1}$ in powers of z/R^*. This peakiness also permits the extension of the limits of integration out to infinity, up to exponentially suppressed terms. The resulting relation

$$R^*(\kappa) = \frac{f_+^2}{2V(f_+)} = \frac{1}{\kappa^2} + \frac{1}{4} - \frac{5\kappa^2}{16} + \mathcal{O}(\kappa^4) \tag{3.52}$$

agrees with Eq. (3.6) to lowest order in κ^2 but introduces subleading corrections that further improve its agreement with the numerical solutions and provide a high degree of accuracy across the Q-ball profile landscape.

An even more accurate relation that closely resembles Eq. (3.52) is

$$R^*(\kappa) = \frac{1}{\kappa^2} - \frac{1}{4\kappa} + \frac{3}{2} - 2\kappa + \frac{1}{3\sqrt{1-\kappa^2}} \, . \tag{3.53}$$

This relationship was produced "experimentally" by tweaking and parameterizing Eq. (3.52) to improve its fit to numerical results, while leaving its fundamental structure intact. It approximates numeric results with an accuracy exceeding 2% in the region $\kappa < 0.84$ (or $R^* \gtrsim 1.5$), the significance of this region being that it allows the formation of stable global Q-balls (i.e. Q-balls with $E < m_\phi Q$). This ultra-precise relation produces extremely accurate expressions of the global Q-ball's energy and charge as a function of radius using the expressions in Section 3.1.4.

3.1.6 Stability

The primary requirement for Q-ball stability, given in Eq. (2.35), is

$$E < m_\phi Q \, . \tag{3.54}$$

In general, this bound can be seen directly in plots of Q-ball parameters; see e.g. Figs. 4.4, 4.5, and 4.6.

The approximations (3.47) can be used to express the stability requirement in terms of ω, ω_0, and m_ϕ for $\omega_0 \ll m_\phi$.

$$\frac{\omega}{m_\phi} \lesssim \frac{1}{14}\left(5+\sqrt{41}\right)+\left(\frac{1}{8}+\frac{37}{56\sqrt{41}}\right)\frac{\omega_0^2}{m_\phi^2} \tag{3.55}$$

Interestingly, the stability does not depend purely on κ but also on ω_0/m_ϕ, although it turns out that this dependence is weak. Numeric results show that the region of stability is between $\kappa \lesssim 0.82$ (for $\omega_0 = 0$) and $\kappa \lesssim 0.84$ (for $\omega_0 \sim m_\phi$). This calculation is the basis for the instability region denoted in several of the global Q-ball figures in Chapter 4.

3.2 Gauged Q-balls

3.2.1 Mapping

An observation from Section 2.10 suggests that there is a connection between the scalar transition region of global Q-balls and the transition region of gauged Q-balls. This arises from the gauge field dynamics and the fact that the gauge field plays a minor role during the scalar transition phase. The resultant "mapping" derived below allows for analytic approximations in the style of global Q-balls.

The starting point for this mapping is, as ever, the thin-wall limit, with f approximated as a step function, $f(\rho) = 1 - \Theta(\rho - R^*)$. This approximation for f can then be used to solve the equation of motion (2.29) for A. With the requirement that $A(\rho)$ and its derivative be

continuous at $\rho = R^*$, a thin-wall profile for A is [7]

$$A(\rho) = \frac{\Omega}{\alpha} \begin{cases} 1 - \dfrac{\sinh(\alpha\rho)}{\cosh(\alpha R^*)\,\alpha\rho}, & \rho < R^*, \\ \dfrac{\alpha R^* - \tanh(\alpha R^*)}{\alpha\rho}, & \rho \geq R^*. \end{cases} \tag{3.56}$$

As with the thin-wall approximation in the global case, this profile remains a good approximation to exact gauge field solutions even for thicker-wall scenarios (i.e. smaller R^* and larger κ).

When the Q-ball radius R^* is large (i.e. in the thin-wall limit), Eq. (3.56) shows that the derivative of αA is small.

$$|\alpha A'(R^*)| = \frac{\Omega}{R^*} \left| \frac{\tanh(\alpha R^*) - \alpha R^*}{\alpha R^*} \right| < \frac{\Omega}{R^*} \tag{3.57}$$

This implies that αA is essentially constant during the transition. The scalar profile can now be iteratively refined by solving the f equation of motion (2.28) around $\rho \sim R^*$ with a constant A.

$$f'' + \frac{2}{\rho} f' = \frac{1}{\Phi_0^2 (m_\phi^2 - \omega_0^2)^2} \frac{\mathrm{d}U}{\mathrm{d}f} - [\Omega - \alpha A(R^*)]^2 f \tag{3.58}$$

Herein lies the mapping. Equation (3.58) is exactly the form of Eq. (2.27) for *global* Q-balls, with the global value of Ω_G given by

$$\Omega_G = \Omega - \alpha A(R^*) \tag{3.59}$$

Since the derivative of αA is small, it does not contribute significantly to the friction over the transition region. This means that the frictional effects over the transition are also almost identical to the global case. Since the relation between Ω_G and R^* is determined by the friction,

if the R^* dependence of the global Q-ball parameter $\Omega_G(R^*)$ is known, then the R^* dependence of the gauged Q-ball $\Omega(R^*)$ can be determined via

$$\boxed{\Omega(R^*) = \Omega_G(R^*)\,\alpha R^* \coth(\alpha R^*)\,.} \tag{3.60}$$

This correspondence makes use of Eq. (3.59) and the thin-wall formula of Eq. (3.56) for $A(R^*)$. It provides a mapping from global Q-balls, for which the relation $\Omega_G(R^*)$ is much easier to obtain both analytically and numerically, to gauged Q-balls for any α. Further, as argued above, the scalar transition profiles for gauged Q-balls are expected to be identical to the transition profiles for the corresponding global Q-balls (Eq. (3.18)). This rather simple argument leads to surprisingly accurate analytic descriptions of gauged Q-balls.

There is another approach to arrive at the mapping of Eq. (3.60). This derivation again relies on the estimations of the thin-wall limit, but it arrives at the mapping relationship via charge Q and energy E rather than the scalar and gauge equations of motion.

Using the thin-wall profile ansätze $f(\rho) \simeq 1 - \Theta(\rho - R^*)$ [7] and A from Eq. (3.56), the charge Q (Eq. (3.67)) can be easily obtained by integrating f and A.

$$Q = \frac{4\pi\Omega\Phi_0^2}{\alpha^3}\left(\alpha R^* - \tanh(\alpha R^*)\right) \tag{3.61}$$

The energy (Eq. (3.74)) is

$$E = \omega Q + \frac{\pi\phi_0^2}{3\sqrt{m_\phi^2 - \omega_0^2}} R^{*2} - \frac{4\pi\phi_0^2}{3\sqrt{m_\phi^2 - \omega_0^2}} \frac{\Omega^2\left(\alpha R^*\left(\operatorname{sech}^2(\alpha R^*) + 2\right) - 3\tanh(\alpha R^*)\right)}{2\alpha^3}, \tag{3.62}$$

Notice that the last term in E goes to zero for $\alpha \to 0$, leading back to the global case.

Eq. (3.3), written in the form $\mathrm{d}E/\mathrm{d}R^* = \omega(R^*)\,\mathrm{d}Q/\mathrm{d}R^*$ to reflect the dependence of ω on R^*, yields a differential equation for $\omega(R^*)$. The solution to this differential equation is

$$\omega(R^*) = \coth(\alpha R^*)\sqrt{cR^{*2} + \alpha^2(m_\phi^2 - \omega_0^2)R^*}\,. \tag{3.63}$$

c is an integration constant that is difficult to obtain, but an approximation $c = \alpha^2\omega_0^2 + \mathcal{O}(\alpha^3)$ is possible from matching Eq. (3.63) to the global case $\kappa^2 \simeq 1/R^*$ (valid roughly for $R^* > 2$). This yields

$$\omega(R^*) = \alpha R^* \coth(\alpha R^*)\sqrt{\omega_0^2 + \frac{m_\phi^2 - \omega_0^2}{R^*}}, \tag{3.64}$$

which is identical to the more general mapping of Eq. (3.60) in the large R^* limit, where $\omega_G \simeq \sqrt{\omega_0^2 + \frac{m_\phi^2 - \omega_0^2}{R^*}}$.

3.2.2 Gauged profile

The mapping in Eq. (3.60) lays a path to construct analytic estimates for gauged Q-ball profiles. Eq. (3.60) furnishes the radius of a gauged Q-ball given the known relationship $\Omega_G(R^*)$ from the global Q-ball (Eq. 3.53). The scalar profile $f(\rho)$ is the transition profile of global Q-balls (Eq. (3.18)), which is shown in Section 3.1.3 to be a very good approximation for the full global profile. The gauge profile $A(\rho)$ is taken from Eq. (3.56).

$$f(\rho) = \frac{1}{\sqrt{1 + 2e^{2(\rho - R^*)}}} \tag{3.65}$$

$$A(\rho) = \frac{\Omega}{\alpha}\begin{cases} 1 - \dfrac{\sinh(\alpha\rho)}{\cosh(\alpha R^*)\,\alpha\rho}, & \rho < R^*, \\ \dfrac{\alpha R^* - \tanh(\alpha R^*)}{\alpha\rho}, & \rho \geq R^*. \end{cases} \tag{3.66}$$

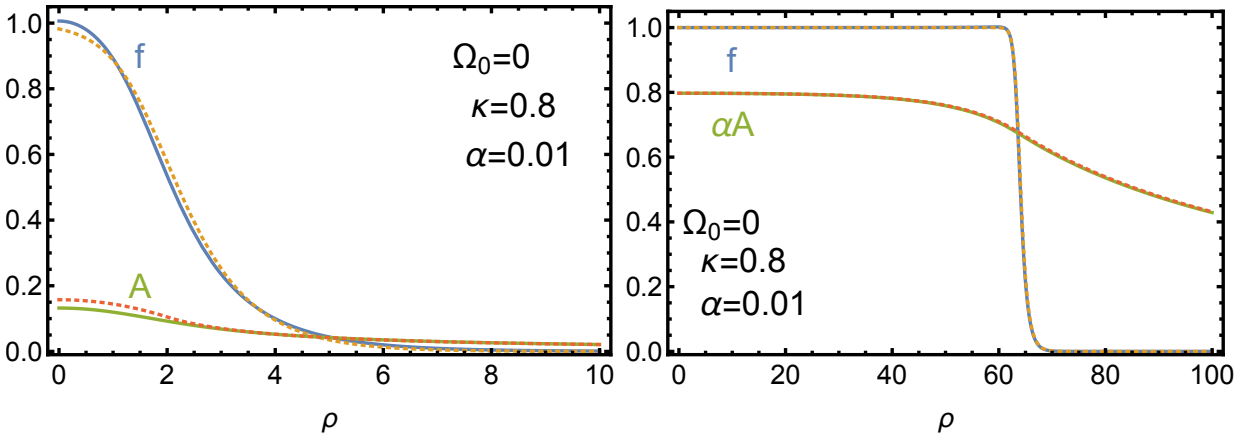

Figure 3.3: *Left:* Profiles of a "thick-wall" gauged Q-ball. *Right:* Profiles of a thin-wall gauged Q-ball. Numeric results are solid lines (blue, green) and analytic approximations are dashed lines (orange, red). Approximations are taken from Eq. (3.65).

Figure 3.3 displays a comparison between numeric calculations and the analytical estimates of (3.65) for one choice of parameters. The numeric methods employed for this analysis are detailed in Chapter 4, along with a description of the use of approximated scalar and gauge field profiles as "seed functions" to power the computational solver.

Note that the two solutions in Fig. 3.3 have the same potential parameters and scalar frequency ω, but they differ in their Q-ball observables such as radius, charge, and energy. These two solutions correspond to the two solutions for R^* obtained from the mapping in Eq. (3.60). As the plot illustrates, the analytic profiles for f and A match the numeric results remarkably well, especially for the large Q-balls (right panel), which is to be expected for profiles derived in the large R^* limit.

More plots and a discussion of their features are presented in Section 4.3.

3.2.3 Charge and energy

The charge of a gauged Q-ball is the integral over the time component of the scalar current

$$Q = 4\pi\Phi_0^2 \int \mathrm{d}\rho\, \rho^2 f^2 (\Omega - \alpha A) \tag{3.67}$$

$$= -\frac{4\pi\Phi_0^2}{\alpha} \lim_{\rho\to\infty} \rho^2 A' \,. \tag{3.68}$$

The expression (3.68) uses the equation of motion for the gauge field (2.29) and the fact that A'' is zero except for a small area in the transition region, which contributes negligibly. This implies that for large ρ,

$$A = \frac{\alpha Q}{4\pi\,\Phi_0^2 \rho} \tag{3.69}$$

up to corrections that fall off faster than $1/\rho$.

The energy is taken directly from the Lagrangian form (2.18)

$$E = 4\pi\Phi_0^2 \sqrt{m_\phi^2 - \omega_0^2} \int \mathrm{d}\rho\, \rho^2 \left[\frac{1}{2} f'^2 + \frac{1}{2} A'^2 + \frac{1}{2} f^2 (\Omega - \alpha A)^2 + \frac{U(f)}{\Phi_0^2 (m_\phi^2 - \omega_0^2)^2} \right] . \tag{3.70}$$

Approximating the energy of gauged Q-balls borrows from the methodology for global Q-balls. The starting point is the Lagrangian (2.24) with a rescaled radial coordinate $\rho \to \chi\rho$.

$$L_{\text{gauged}} = 4\pi\Phi_0^2 \sqrt{m_\phi^2 - \omega_0^2} \int \mathrm{d}\rho\, \rho^2 \chi \left[-\frac{1}{2} f'^2 + \frac{1}{2} A'^2 + \chi^2 V_{\text{gauged}}(f, A) \right] \tag{3.71}$$

$V_{\text{gauged}}(f, A)$ is defined in Eq. (2.21). When varied with respect to χ, which is subsequently set to $\chi = 1$, the Lagrangian has two parts: a part that explicitly depends on χ and a part in which a variation appears because ρ-dependent functions now depend on χ, e.g. $f(\rho) \to f(\rho\chi)$. This second collection of terms is simply the usual variation of the Lagrangian and vanishes by

definition when $\chi = 1$. Requiring the other term in the variation, which depends explicitly on χ, to also vanish provides the constraint

$$0 = \int \mathrm{d}\rho\, \rho^2 \left[-\frac{1}{2} f'^2 + \frac{1}{2} A'^2 + 3 V_{\text{gauged}}(f, A) \right]. \tag{3.72}$$

This constraint allows E to be formulated without an explicit $U(f)$ dependence.

$$\begin{aligned} E =& 4\pi \Phi_0^2 \sqrt{m_\phi^2 - \omega_0^2} \int \mathrm{d}\rho\, \rho^2 \left[\frac{1}{3} f'^2 + \frac{2}{3} A'^2 + f^2 (\alpha A - \Omega)^2 \right] \\ =& 4\pi \Phi_0^2 \sqrt{m_\phi^2 - \omega_0^2} \int \mathrm{d}\rho\, \rho^2 \left[\frac{1}{3} f'^2 + \frac{2}{3} A'^2 + \frac{1}{\alpha \rho^2} (\alpha A - \Omega) \left(\rho^2 A' \right)' \right] \end{aligned} \tag{3.73}$$

The second equality makes use of the equation of motion for A from Eq. (2.29). When the third term is integrated by parts, the expression becomes

$$E = \sqrt{m_\phi^2 - \omega_0^2} \left[\Omega Q + \frac{4\pi \Phi_0^2}{3} \int \mathrm{d}\rho\, \rho^2 \left(f'^2 - A'^2 \right) \right]. \tag{3.74}$$

This result may alternately be expressed with the potential $V_{\text{gauged}}(f, A)$, which eliminates derivatives in E.

$$E = \sqrt{m_\phi^2 - \omega_0^2} \left[\Omega Q + 8\pi \Phi_0^2 \int \mathrm{d}\rho\, \rho^2\, V_{\text{gauged}}(f, A) \right] \tag{3.75}$$

As discussed in Section 3.2.1, in the limiting situation of large R^*, the expressions for charge and energy simplify to

$$Q = \frac{4\pi}{\alpha^2} \Phi_0^2 \left(\alpha R^* \coth(\alpha R^*) - 1 \right) \sqrt{R^{*2} \Omega_0^2 + R^*}, \tag{3.76}$$

$$\begin{aligned} E = \frac{\pi m_\phi R^* \Phi_0^2 \operatorname{csch}^2(\alpha R^*)}{6\alpha \sqrt{\Omega_0^2 + 1}} \Big[& \alpha R^* \left(4 R^* \Omega_0^2 + 3 \right) - 6 \left(R^* \Omega_0^2 + 1 \right) \sinh(2\alpha R^*) \\ & + \alpha R^* \left(8 R^* \Omega_0^2 + 9 \right) \cosh(2\alpha R^*) \Big] . \end{aligned} \tag{3.77}$$

These predictions are more approximate than the full integrals, which are calculated in `Mathematica` and used to generate the figures, but they are much more manageable and still make excellent predictions at large R^*. They are included here for their utility in that regard.

Finally, a word about maximal radii and their connection to Q and E. In Section 4.3, the numeric solutions all show maximal radii. For a given benchmark, this maximal radius can have one of two origins: (1) the inequality of Eq. (2.47) or (2) $\kappa = \kappa_{\max} = 1$. For benchmarks in which $R^*_{\max}$ is set by the condition $\kappa = 1$ rather than by Eq. (2.47), a prediction can be made for $R^*_{\max}$. Eq. (3.60) and the substitution of the large-R^* relation $\kappa_{\text{global}} = 1/\sqrt{R^*}$ (Eq. (3.6)) yields

$$\alpha^2 R^*_{\max}(1 + R^*_{\max}\Omega_0^2)\coth^2(R^*_{\max}\alpha) - \Omega_0^2 = 1\,. \tag{3.78}$$

This equation cannot be solved analytically, but has the limiting cases

$$R^*_{\max} \simeq \begin{cases} \frac{1}{\alpha^2}\,, & \text{for } \Omega_0 \lesssim \alpha\,, \\ \frac{1}{\alpha\Omega_0}\,, & \text{for } \Omega_0 \gg \alpha\,. \end{cases} \tag{3.79}$$

Since both charge and energy grow with R^* for large radii, this $R^*_{\max}$ also implies a maximal Q-ball charge and energy for a given set of potential parameters, which can be seen in the figures of Section 4.3. This qualitative claim was made in Ref. [7], but without the quantitative predictions and numeric verification presented here.

3.3 Proca Q-balls

Lastly are Proca Q-balls, i.e. gauged Q-balls where the gauge field is massive. The Proca Q-balls analytical discussion will look very similar to that of gauged Q-balls, only with more complexity. Proca Q-balls are the most general types of Q-balls; global and gauged Q-balls are

special cases of Proca Q-balls, with $\alpha \to 0$ and $M \to 0$, respectively. This provides a useful check for derived Proca approximations, which must return to the approximations of Section 3.1 and 3.2 in their respective limits.

3.3.1 Proca profile

The discussion begins, as usual, in the thin-wall limit, with the scalar profile approximated by a step function, $f \sim 1-\Theta(\rho-R^*)$ [2, 7], which is defined exclusively by the radius R^*. This was the starting ansatz in both the global ($M \to \infty$) and gauged ($M \to 0$) cases, and is sensible here given that the gauge boson mass interpolates between these two cases. Using this ansatz for f, the differential equation for A, Eq. (2.31), yields the solution

$$A(\rho) = \frac{\alpha\Omega}{\mu^2} \begin{cases} 1 - \dfrac{1}{\rho} \dfrac{(1+MR^*)\sinh(\rho\mu)}{\mu\cosh(R^*\mu) + M\sinh(R^*\mu)}, & \rho < R^* \\ \dfrac{R^*\mu - \tanh(R^*\mu)}{\mu + M\tanh(R^*\mu)} \dfrac{e^{(R^*-\rho)M}}{\rho}, & \rho \geq R^* \end{cases} . \tag{3.80}$$

It has been required that A and A' be continuous at $\rho = R^*$. A new quantity $\mu \equiv \sqrt{\alpha^2 + M^2}$ is introduced, which is the effective mass of the gauge field inside the Q-ball. Like in the gauged case, the thin-wall A profile is a good approximation of the exact solution when the radius is not large; see for example the green dashed lines in Fig. 2.5.

The scalar profile can be improved by replacing the step function by the transition profile

$$f = \frac{1}{\sqrt{1+2e^{2(\rho-R^*)}}}, \tag{3.81}$$

which was derived for the global case (c.f. Eq. (3.18)) and shown to be an excellent approximation for scalar profile for all radii. The transition function continues to hold its own even in the presence of gauge and Proca fields; see the red dashed lines in Fig. 2.5 for an illustration of its efficacy.

3.3.2 Mapping

The following discussion maps closely to Section 3.2.1 (pun intended).

As with the gauged case, it is expected that the derivative of A will be small when f transitions from 1 to 0. Eq. (3.80) allows an estimate for how much αA changes in the scalar transition region.

$$|\alpha A'(R^*)| = \alpha^2 \frac{\Omega(1+MR^*)}{\mu^2 R^{*2}} \left| \frac{\tanh(\mu R^*) - \mu R^*}{\mu + M\tanh(\mu R^*)} \right| < \frac{\alpha\Omega}{3} \tag{3.82}$$

This implies that $\alpha A' \ll 1$ for small $\alpha\Omega$ during the f transition from interior to exterior, so A is approximately constant. In fact, this mapping is qualitatively, and often quantitatively, accurate even beyond the small $\alpha\Omega$ limit, as shown below.

In the region around $\rho \sim R^*$, the f equation in Eq. (2.30) takes the form

$$(\rho^2 f')' = \frac{\rho^2}{\Phi_0^2(m_\phi^2 - \omega_0^2)^2} \frac{\mathrm{d}U}{\mathrm{d}f} - \rho^2 \left[\Omega - \alpha A(R^*)\right]^2 f \ . \tag{3.83}$$

As with the gauged case, this is the form of the potential for the global Q-ball equation with the global value of $\Omega = \Omega_G$ given by

$$\Omega_G = \Omega - \alpha A(R^*) \ . \tag{3.84}$$

This makes clear that the f transition profiles for Proca Q-balls can be identified with particular transition profiles for *global* Q-balls. This is very convenient, as an excellent and simple approximation for global transition profiles has already been identified in Eq. (3.18).

However, these profiles only match when the amount of friction is the same for both the global and gauged cases, which implies that the radius R^* is the same for each. Therefore, if the R^* dependence of the global Q-ball parameter $\Omega_G(R^*)$ is known, the R^* dependence of the Proca

Q-ball $\Omega(R^*)$ can be determined via

$$\boxed{\Omega(R^*) = \Omega_G(R^*)\left[1 - \frac{\alpha^2}{\mu^2 R^*}\frac{R^*\mu - \tanh(R^*\mu)}{\mu + M\tanh(R^*\mu)}\right]^{-1}} \tag{3.85}$$

Here the profile given in Eq. (3.80) has been used for $A(R^*)$. A check that $\Omega(R^*) \to \Omega_G(R^*)$ for either $\alpha \to 0$ or $M \to \infty$ confirms that this relation holds for the limiting case of global Q-balls; $M \to 0$ reduces to the gauged mapping relation of Eq. (3.60).

This mapping provides remarkably accurate predictions using the much simpler results from global Q-balls, for which $\Omega_G(R^*)$ is easier to obtain both analytically and numerically. Both the gauged mapping of Eq. (3.60) and the Proca mapping of Eq. (3.85) are recent, novel additions to the Q-ball literature. They were introduced in a series of papers [33, 34] by the author and collaborators.

The mapping of Eq. (3.85) can lead to a maximal radius constraint for certain Proca Q-balls, although the complexity of the mapping initially makes this difficult to see. Taken in the large R^* limit and using the relation $\Omega_G^2 \simeq \Omega_0^2 + 1/R^*$ in Eq. (3.85), κ approaches

$$\kappa(R^* \to \infty) \to \frac{\alpha\Omega_0}{M} \tag{3.86}$$

for $M > 0$. Since stable localized Q-balls require $\kappa \leq 1$ (corresponding to $\omega \leq m_\phi$), the immediate implication of Eq. (3.86) is that Proca Q-balls with $M < \alpha\Omega_0$ exhibit a maximal radius just like gauged Q-balls. Proca Q-balls with $M > \alpha\Omega_0$ can potentially be arbitrarily large like global Q-balls.[2] This quantifies previous statements that heavy (light) gauge bosons give rise to solitons that resemble global (gauged) ones. Eq. (3.86) provides another qualitative point of evidence for the statement that Proca Q-balls interpolate between the global and gauged cases via the gauge boson mass.

[2]Additional relations need to be satisfied to evade a maximal radius, in particular Eq. (2.47).

3.3.3 Charge and energy

The charge and energy of Proca Q-balls fellow from the methods of the global and gauged cases. The charge is the integral over the time component of the scalar current.

$$Q = 4\pi\Phi_0^2 \int \mathrm{d}\rho\, \rho^2 f^2 (\Omega - \alpha A) \tag{3.87}$$

Using the equation of motion (2.31), the charge can be rewritten as

$$Q = \frac{4\pi\Phi_0^2}{\alpha} \int \mathrm{d}\rho\, \rho^2 \left[A'' + \frac{2}{\rho} A' - M^2 A \right] \tag{3.88}$$

A'' is zero except for within a small area around the transition region, and its contribution is negligible.

The energy comes as usual from the Hamiltonian

$$\begin{aligned} E &= 4\pi\Phi_0^2 \sqrt{m_\phi^2 - \omega_0^2} \int \mathrm{d}\rho\, \rho^2 \left\{ \frac{1}{2} f'^2 + \frac{1}{2} A'^2 + \frac{1}{2} f^2 (\Omega - \alpha A)^2 + \frac{U(f)}{\Phi_0^2 (m_\phi^2 - \omega_0^2)^2} + \frac{M^2}{2} A^2 \right\} \\ &= \sqrt{m_\phi^2 - \omega_0^2} \left[\Omega Q + \frac{4\pi\Phi_0^2}{3} \int \mathrm{d}\rho\, \rho^2 \left(f'^2 - A'^2 \right) \right]. \end{aligned} \tag{3.89}$$

As in the gauged case, the charge and energy of Proca Q-balls can be refined by the results of the scalar and gauge field profiles in the Proca case. Deriving a simplified expression for the energy proceeds exactly as in the gauged case in Section 3.2.3.

Rescaling the radial coordinate $\rho \to \chi\rho$ in the Lagrangian (2.25) yields

$$L = \sqrt{m_\phi^2 - \omega_0^2}\, 4\pi\Phi_0^2 \int \mathrm{d}\rho\, \rho^2 \chi \left[-\frac{1}{2} f'^2 + \frac{1}{2} A'^2 + \chi^2 V_{\mathrm{proca}}(f, A) \right]. \tag{3.90}$$

When this Lagrangian is varied with respect to χ, there emerge two parts with different χ dependences: a set of terms in which the variation is implicit in the functions $f(\rho) \to f(\rho\chi)$, $A(\rho) \to A(\rho\chi)$, which vanishes when $\chi = 1$; and a set of terms that explicitly depend on χ. This second set of terms must also vanish when $\chi = 1$.

$$0 = \int \mathrm{d}\rho\, \rho^2 \left[-\frac{1}{2} f'^2 + \frac{1}{2} A'^2 + 3V(f,A) \right] \tag{3.91}$$

This constraint allows Eq. (3.89) to be expressed without an explicit $U(f)$ dependence.

$$\begin{aligned} E &= 4\pi\Phi_0^2 \sqrt{m_\phi^2 - \omega_0^2} \int \mathrm{d}\rho\, \rho^2 \left[\frac{1}{3} f'^2 + \frac{2}{3} A'^2 + f^2(\alpha A - \Omega)^2 + M^2 A^2 \right] \\ &= 4\pi\Phi_0^2 \sqrt{m_\phi^2 - \omega_0^2} \int \mathrm{d}\rho\, \rho^2 \left[\frac{1}{3} f'^2 + \frac{2}{3} A'^2 + \frac{1}{\alpha\rho^2} (\alpha A - \Omega) \left(\rho^2 A' \right)' + \frac{M^2 \Omega}{\alpha} \right] \end{aligned} \tag{3.92}$$

Integration of the third term by parts produces

$$E = \sqrt{m_\phi^2 - \omega_0^2} \left[\Omega Q + \frac{4\pi\Phi_0^2}{3} \int \mathrm{d}\rho\, \rho^2 \left(f'^2 - A'^2 \right) \right]. \tag{3.93}$$

3.3.4 Relationship between energy, charge, and frequency

Section 2.12 discusses the relationship between energy, charge, and frequency in the global case and interprets it physically as a type of chemical potential. This section provides a derivation to show that the relationship Eq. (3.3) remains valid in the Proca case with nonzero M.

The definition of Q for Proca Q-balls is

$$Q = 4\pi\Phi_0^2 \int \mathrm{d}\rho\, \rho^2 f^2 (\Omega - \alpha A) \tag{3.94}$$

$$= \frac{4\pi\Phi_0^2 M^2}{\alpha} \int \mathrm{d}\rho\, \rho^2 A - \frac{4\pi\Phi_0^2}{\alpha} \lim_{\rho\to\infty} \rho^2 A', \tag{3.95}$$

where the second line uses the equation of motion (2.31) for A. If $M = 0$, this implies that for large ρ

$$A = \frac{\alpha Q}{4\pi \Phi_0^2 \rho} \,, \tag{3.96}$$

up to corrections that fall off faster than $1/\rho$ [7]. For $M \neq 0$, requiring a finite Q implies A falls off faster than $1/\rho$; therefore

$$\frac{Q\alpha}{4\pi\Phi_0^2 M^2} = \int \mathrm{d}\rho\, \rho^2 A \,. \tag{3.97}$$

These results lead to a rewriting of the Proca energy (3.89).

$$\begin{aligned} E &= 4\pi\Phi_0^2 \sqrt{m_\phi^2 - \omega_0^2} \int \mathrm{d}\rho\, \rho^2 \left[\frac{1}{2} f'^2 + \frac{1}{2} A'^2 + f^2(\Omega - \alpha A)^2 + M^2 A^2 - V_{\text{proca}}(f, A) \right] \\ &= 4\pi\Phi_0^2 \sqrt{m_\phi^2 - \omega_0^2} \int \mathrm{d}\rho\, \rho^2 \left[\frac{1}{2} f'^2 + \frac{1}{2} A'^2 + \frac{1}{\alpha\rho^2}(A\alpha - \Omega)\left(\rho^2 A'\right)' + \frac{\Omega M^2}{\alpha} A - V_{\text{proca}}(f, A) \right] \end{aligned} \tag{3.98}$$

The equation of motion (2.31) is used in the second line. The third term can be integrated by parts; when $M = 0$ this produces a nonzero boundary term determined by Eq. (3.96). When $M \neq 0$, the boundary term vanishes and the fourth term can be evaluated using Eq. (3.97). For either mass,

$$E = \omega Q - L \,. \tag{3.99}$$

The derivative of L turns out to be Q.

$$\begin{aligned}\frac{\mathrm{d}L}{\mathrm{d}\omega} &= \sqrt{m_\phi^2 - \omega_0^2}\, 4\pi\Phi_0^2 \int \mathrm{d}\rho\, \rho^2 \left[-f' \frac{\mathrm{d}f'}{\mathrm{d}\Omega} + A' \frac{\mathrm{d}A'}{\mathrm{d}\Omega} + \frac{\mathrm{d}V}{\mathrm{d}\Omega} \right] \\ &= \sqrt{m_\phi^2 - \omega_0^2}\, 4\pi\Phi_0^2 \left\{ \rho^2 A' \frac{\mathrm{d}A}{\mathrm{d}\Omega}\bigg|_0^\infty + \int \mathrm{d}\rho\, \rho^2 \left[-\frac{\mathrm{d}f}{\mathrm{d}\Omega} \frac{\partial V}{\partial f} - \frac{\mathrm{d}A}{\mathrm{d}\Omega} \frac{\partial V}{\partial A} + \frac{\mathrm{d}V}{\mathrm{d}\Omega} \right] \right\} \\ &= \sqrt{m_\phi^2 - \omega_0^2}\, 4\pi\Phi_0^2 \int \mathrm{d}\rho\, \rho^2 \frac{\partial V}{\partial \Omega} \\ &= Q\,, \end{aligned} \tag{3.100}$$

The large-ρ A (3.96) should be used to evaluate the limit in the second line when $M = 0$. This result implies that

$$\frac{\mathrm{d}E}{\mathrm{d}\omega} = \omega \frac{\mathrm{d}Q}{\mathrm{d}\omega}\,. \tag{3.101}$$

This extends the relationship $\mathrm{d}E/\mathrm{d}\omega = \omega\, \mathrm{d}Q/\mathrm{d}\omega$ to the case of nonzero M.

Chapter 4

Numeric solutions

4.1 Methods

There are a variety of methods for solving the scalar and gauge field equations of motion numerically, particularly in the simplest case of global Q-balls.

The mechanical analogy of a particle rolling down a potential in the presence of friction (see Section 2.10) suggests the "shooting" method. With this technique, an initial, numeric value for f is selected at $\rho = 0$, then the equation of motion is numerically integrated out to $\rho \gg 1$. A visual inspection confirms whether f has overshot or undershot the $f = 0$ maximum of the potential. The guess for f is then manually tuned until eventually the field comes to rest on the $f = 0$ point of the effective potential. While numerically simple and easy to implement, this method is tedious and difficult to automate. Furthermore, it becomes completely unwieldy for the coupled differential equations of the gauged and Proca cases. The precision required to arrive at viable coupled solutions is functionally impossible to approach simultaneously in each variable.

Another option in the global case is to interpret the differential equation (2.27) as a vacuum tunneling process. Various computer codes exist to efficiently solve the vacuum tunneling problem, e.g. `AnyBubble` [35], and they can easily be repurposed to solve for Q-ball profiles. Like the shooting method, however, these software packages cease to be useful when the gauge field is introduced. Their main utility in this work was to confirm the results and behavior of the custom `Mathematica` notebooks created for this project in the global case, which was subsequently used to check the behavior of the gauged and Proca cases.

The final approach for all three cases was to solve the boundary value problems directly via the finite element methods of `Mathematica`. Unfortunately, `Mathematica` cannot reliably solve differential equations in which some of the boundary conditions are taken at infinity. To evade this computational difficultly, a new, compactified radial coordinate y can be substituted for ρ in the equations of motion.

$$y = \frac{\rho}{1+\rho/a} \tag{4.1}$$

a is any positive number. It is taken in all numeric solutions to be $a = 1000$. This new coordinate maps the range $\rho \in [0, \infty)$ to $y \in [0, a]$, and ρ derivatives become

$$\frac{\mathrm{d}}{\mathrm{d}\rho} = \frac{\mathrm{d}y}{\mathrm{d}\rho}\frac{\mathrm{d}}{\mathrm{d}y} = \left(1-\frac{y}{a}\right)^2 \frac{\mathrm{d}}{\mathrm{d}y}\,. \tag{4.2}$$

The global differential equation (2.27) is now

$$\left(1-\frac{y}{a}\right)^4 \left(f'' + \frac{2}{y}f'\right) + \frac{\mathrm{d}V_{\text{global}}}{\mathrm{d}f} = 0\,, \tag{4.3}$$

with the boundary conditions $f'(0) = 0$ and $f(a) = 0$. A boundary condition at $a = 1000$ rather than $\rho = \infty$ is handled much more gracefully by `Mathematica`.

The differential equations (2.28), (2.29), (2.30), and (2.31) become

$$\left(1-\frac{y}{a}\right)^4\left(f''+\frac{2}{y}f'\right)+\frac{\partial V(f,A)}{\partial f}=0\,, \tag{4.4}$$

$$\left(1-\frac{y}{a}\right)^4\left(A''+\frac{2}{y}A'\right)-\frac{\partial V(f,A)}{\partial A}=0\,, \tag{4.5}$$

where $V(f,A)$ is either $V_{\text{gauged}}(f,A)$ or $V_{\text{proca}}(f,A)$ depending on the context. The gauge field introduces two new boundary conditions: $A'(0)=0$ and $A(a)=0$.

Q-balls with certain potential configurations, particularly in regions of parameter space in which viable Q-ball profiles are densely spaced (usually because they have highly varying radii for similar κ), are beyond `Mathematica`'s capacity to solve unassisted. In this situations, precise guess functions, i.e. seed functions, that are highly similar to the expected numerical solution are needed. The analytic approximations of Chapter 3 are generally accurate enough to serve as these seed functions.

In some regions, even the very accurate analytic approximations are not precise enough to aid `Mathematica` in converging on a correct solution. In these instances, previously generated numeric solutions for similar κ may serve as seed functions instead. Iterative use of solutions as seed functions can generate Q-ball solutions in otherwise unreachable parameter space. Taken to extreme precisions, this iterative method is dubbed "crawling". An automated, iterative solution loop capable of many digits of precision in κ, "the Crawler," provides access in the most solution-resistant regions of parameter space.

A downside of radial compactification is the uneven visualization of Q-balls when the profile solutions are plotted over y. The features of large Q-balls are radially compressed when plotted vs. y relative to small Q-balls. In practice, this is not a problem, as large Q-balls are already well-described by approximations in the thin-wall limit. This note applies only to plotting considerations encountered in the course of working with the compactified coordinate in

Mathematica and is not relevant to a casual reader, as all plots and figures shown here are plotted in the true, non-compactified radial coordinate ρ, not y.

4.2 Global

Fig. 2.1 shows the potentials and profiles for several values of $0 < \kappa < 1$. In the left plot, the single-particle trajectories that lead to Q-ball solutions are plotted as solid lines, while the remainder of the potential is dashed. The initial position of the particle, which corresponds to the value of $f(0)$ at the center of the Q-ball, is marked by a solid point. The corresponding $f(\rho)$ profiles are shown in the right plot; they are analogous to the position of the particle as a function of time.

The right plot in Fig. 2.1 shows that Q-balls become bigger and less rounded for smaller κ. In fact, global Q-ball profiles tend to a step function as $\kappa \to 0$, which is Coleman's thin-wall limit. [2] Small κ solutions are called thin-wall profiles. Conversely, when $\kappa \to 1$, Q-balls become more "fuzzy" (i.e. their transition region is wider and more diffuse) and approach the trivial vacuum solution $f = 0$. Past a certain threshold, estimated analytically in Eq. (3.55), these thick-wall Q-balls are unstable; see e.g. Fig. 4.2. The Q-ball radius $f''(R^*) = 0$ also has a clear physical meaning in the profiles of Fig. 2.1 as the midpoint of the transition region.

The following figures and discussion are a granular comparison of various global Q-ball predictions to their corresponding numeric results. While such a comparison is not undertaken for gauged and Proca Q-balls, they are closely related to global Q-balls via their mappings (Eqs. (3.60) and (3.85), respectively), and thus the precision demonstrated here for global Q-balls indirectly applies to them, too.

Fig. 4.1 compares the analytically-derived Q and E component integrals of (3.46) (blue curve) to numeric results (black dashed) for those same integrals. The agreement is excellent for

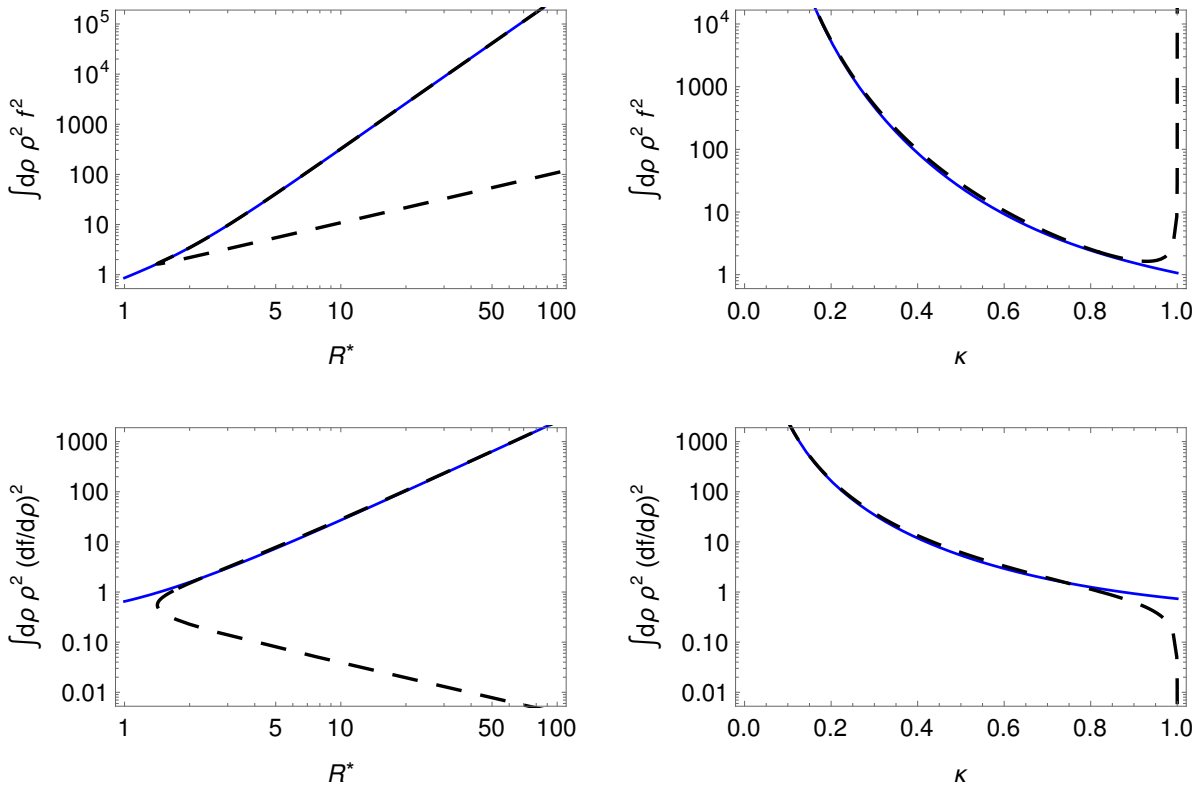

Figure 4.1: The integrals $\int \mathrm{d}\rho\, \rho^2 f^2$ (*top*) and $\int \mathrm{d}\rho\, \rho^2 f'^2$ (*bottom*) as a function of R^* (*left*) and κ (*right*). The dashed black line denotes the exact numerical solution and the blue solid line the predictions (3.46).

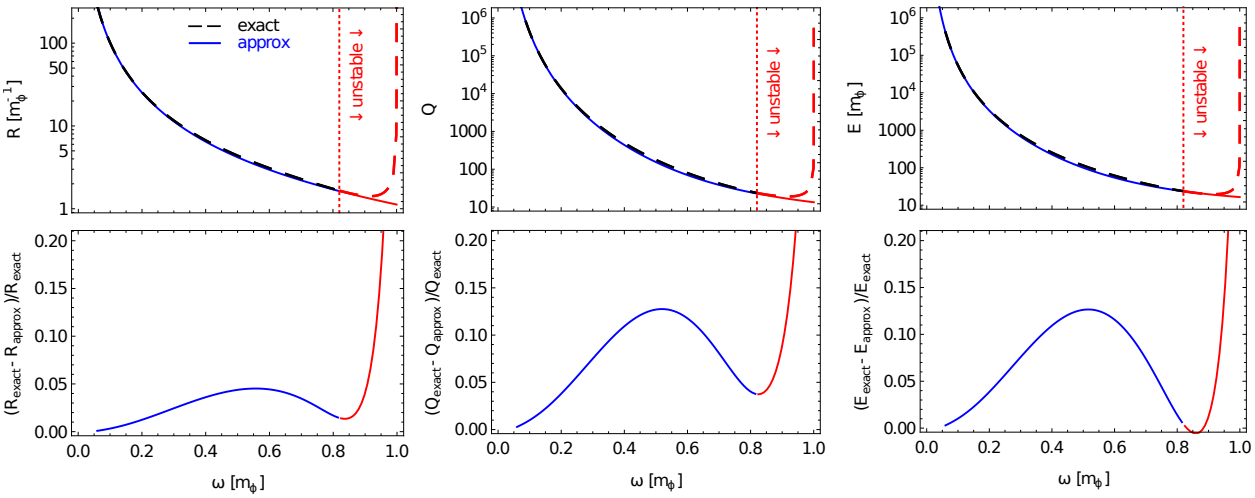

Figure 4.2: $R(\omega)$ (*left*), $Q(\omega)$ (*middle*), and $E(\omega)$ (*right*) for the potential parameter set $\phi_0 = m_\phi$, $\omega_0 = 0$. In the upper row, black (red) dashed lines show the exact numeric values in the stable (unstable) regime. Blue and red solid curves are the approximations of Eq. (3.47). The lower row provides the relative difference between exact and approximate values. The red region $\omega \gtrsim 0.82$ is the realm of unstable Q-balls with $E > m_\phi Q$.

stable Q-balls, i.e. $\kappa \lesssim 0.8$. As a function of R^*, analytic result for $\int \mathrm{d}\rho\, \rho^2 f^2$ approximates the true numeric solution to better than 1% for stable Q-balls. The agreement as a function of κ is not as good, with the match worsening to 13% near $\kappa \sim 0.5$. This is due to imperfect $R^*(\kappa)$ modeling. The integral $\int \mathrm{d}\rho\, \rho^2 (f')^2$ agrees with the numerical results to better than 5% for $R^* > 2$ and better than 13% for $\kappa \lesssim 0.8$.

Fig. 4.2 evaluates the accuracy of the approximation (3.52) of $R^*(\omega)$ with the parameters $\phi_0 = m_\phi$, $\omega_0 = 0$. Beyond $\omega \sim 0.82 m_\phi$ (red region), the Q-balls have $E > m_\phi Q$ and are unstable to fission; accuracy is not phenomenologically important here. The analytic estimate (3.52) agrees with the numeric results to better than 5% in the stable Q-ball regime, another fantastic result. As expected, in the thin-wall limit $\omega \to \omega_0$ the agreement becomes exact, since the analytic approximations were derived in this limit.

Shown in the middle and right columns are Q and E as functions of ω, respectively. The numeric and analytic results agree to better than 13% over the entire stable region. The improvement over the original simple, thin-wall formulas (3.2), for which agreement was only

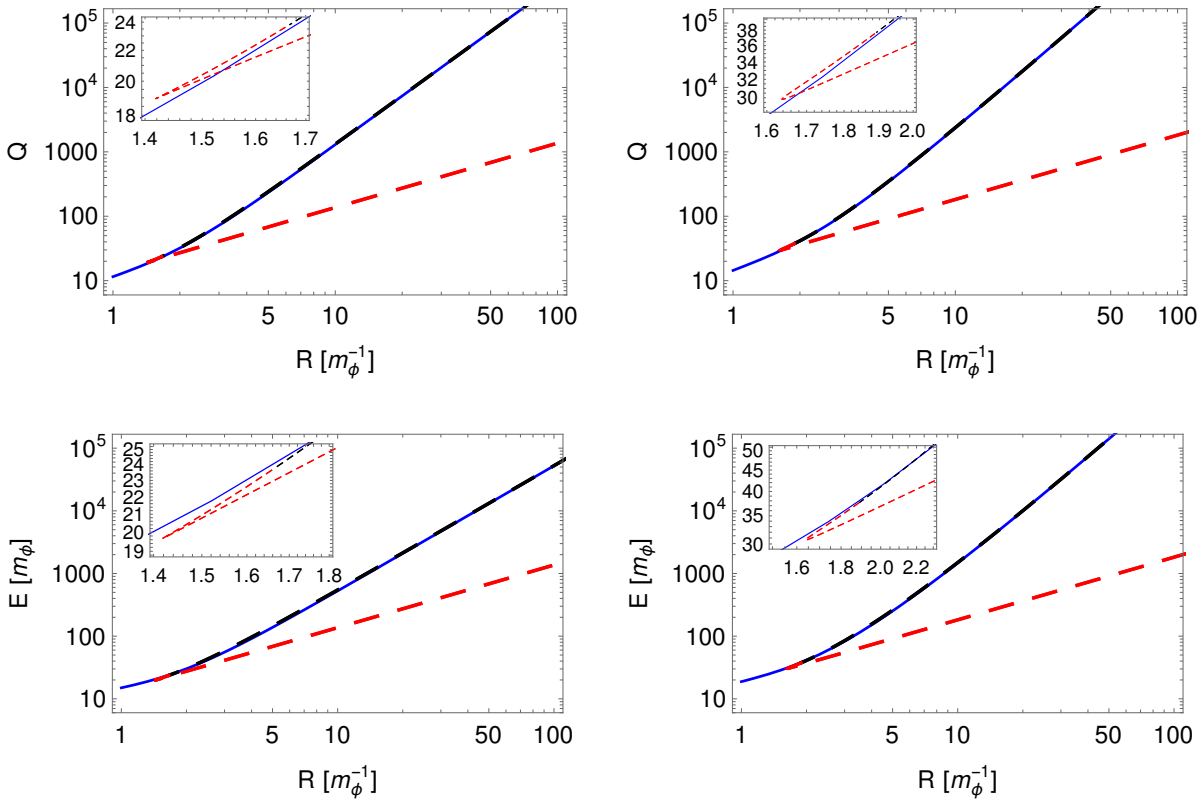

Figure 4.3: $Q(R^*)$ (*top*) and $E(R^*)$ (*bottom*) for $\phi_0 = m_\phi$ and $\omega_0 = 0$ (*left*), $\omega_0 = m_\phi/2$ (*right*). Dashed black lines are the exact solution in the stable regime; dashed red lines are unstable exact solutions. Blue solid lines are the predictions of Eq. (3.47).

50%, makes the success of the refined estimates even more apparent. Errors in the approximation $R^*(\omega)$ propagate into magnified errors in Q and E, which explains the relatively worse agreement compared to $R^*(\omega)$. The fit for $Q(\omega)$ and $E(\omega)$could be improved with a further refined $R^*(\omega)$.

Fig. 4.3 demonstrates the accuracy of $Q(R^*)$ and $E(R^*)$ using $\omega(R^*)$ from the inversion of Eq. (3.52). The agreement is superior to that of $Q(\omega)$ and $E(\omega)$ shown in Fig. 4.2: better than 3% for $Q(R^*)$ and 5% for $E(R^*)$ for stable Q-balls. This is an order-of-magnitude improvement over the first-order approximations of Eq. (3.2), which have agreement as poor as 40%. This excellent agreement further demonstrates that $R^*(\omega)$ is the dominant source of error, while the explicit dependence on the radius in (3.47) is very accurate.

Fig. 4.3 also illustrates the qualitative difference of the two cases $\omega_0 = 0$ (left column) and $\omega_0 > 0$ (right column). For large R and $\omega_0 \neq 0$, $E \propto Q \propto R^3$ as expected from the thin-wall approximation. However, as observed in Ref. [30], for $\omega_0 = 0$, $\omega \sim \sqrt{m_\phi / R}$ for large R and thus $Q \propto R^{5/2}$ and $E \propto R^2$. In the unstable regime, which is not well-approximated, numeric results give $E \simeq m_\phi Q \propto R$ for large R for all ω_0.

4.3 Gauged

Examining a range of benchmarks, i.e. combinations of potential parameters, provides information about Q-balls in the aggregate. Fig. 4.4 plots Q-ball predictions and numeric solutions for the benchmark point $\Omega_0 = 5$ and $\alpha = 1/100$, where $\phi_0 = m_\phi$ and all dimensional quantities are measured in units of m_ϕ. In the top left panel, the numerical results for κ vs. R^* (circles) are compared with the prediction of Eq. (3.60) (line). The other panels show the analogous results for $E/m_\phi, Q$, and $(E/m_\phi Q)$. Overall, there is excellent agreement between the numerical and analytical results.

The existence constraints on Q-balls are clearly visible in these figures. First, $\omega \leq m_\phi$ (or $\kappa \leq 1$) (c.f. discussion in Section 2.3). This implies a maximum Q-ball radius.[1] Secondly, $E \leq m_\phi Q$ ensures that the Q-ball is stable against decay to scalars. This constraint implies the existence of a *minimal* Q-ball radius, which can be best seen in the top right panel of Fig. 4.4. Q-balls with $E > m_\phi Q$ are unstable; this is shown in the figure with a dashed line for the prediction and open markers for the numeric solutions. The stable solution with smallest R^* is demarcated by a star.

Finally, the constraint of Eq. (2.47) requires that the scalar potential have a second maximum away from $f = 0$. This puts an upper bound on the radius which, for this benchmark, is more

[1] This constraint could in theory be circumvented by a contrived and thorny potential designed to do just that. Such a potential is not of interest here.

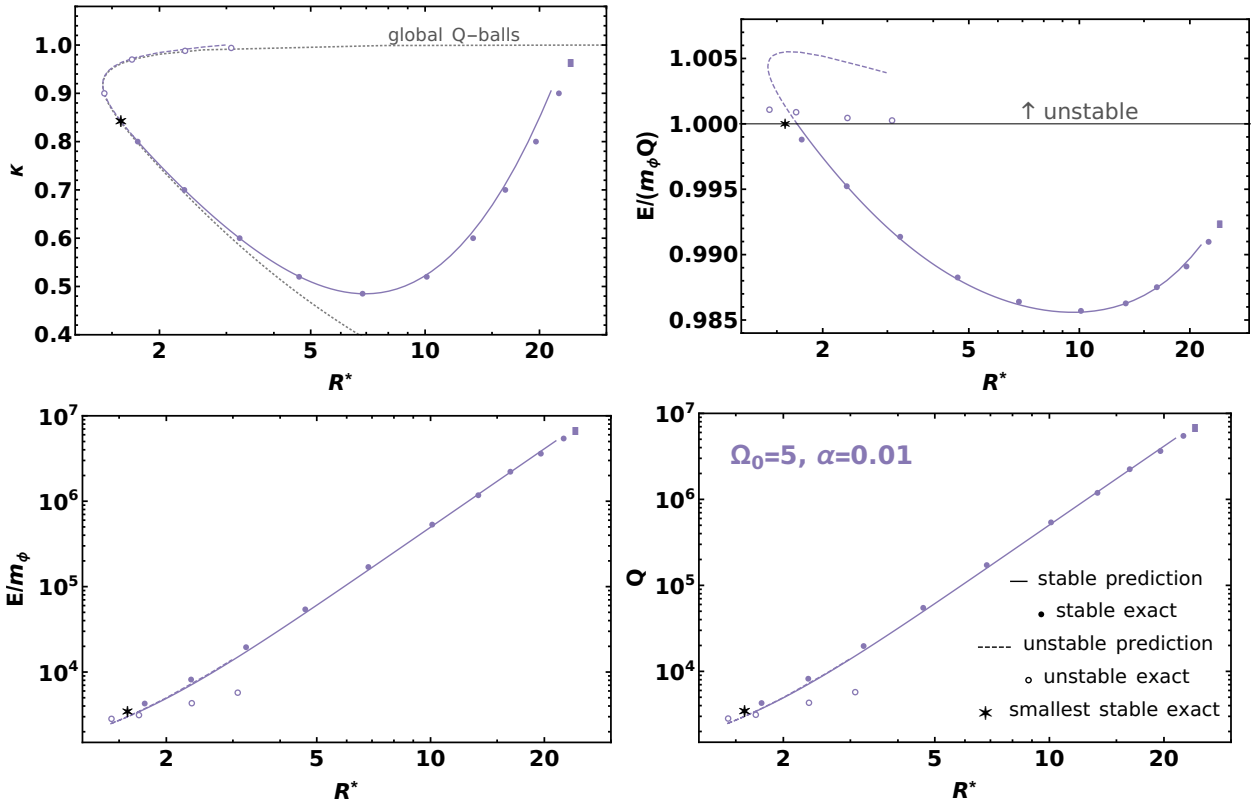

Figure 4.4: A comparison of predictions from Eq. (3.60) to numeric solutions for κ (*top left*), E/m_ϕ (*bottom left*), Q (*bottom right*), and $E/(m_\phi Q)$ (*top right*) for a sample benchmark $\Omega_0 = 5$, $\alpha = 0.01$, $\phi_0 = m_\phi$. Predicted stable and unstable solutions are shown as solid and dashed lines, respectively, and stable and unstable numeric solutions are shown as filled and open points, respectively. The gray dotted line shows the global Q-ball case. The rectangle is the largest numerical solution.

restrictive than the maximal radius determined by the relation $\omega \leq m_\phi$. Using Eq. (2.47) with $A = A(0)$ from the thin-wall approximated profile from Eq. (3.56), this maximal radius $R^*_{\max}$ can be calculated numerically. $R^*_{\max}$ is a prediction and can be seen in Fig. 4.4 where the solid prediction line ends before $\kappa = 1$. Since the thin-wall $A(0)$ overestimates the true value, $R^*_{\max}$ is slightly smaller than the true maximal radius (a rectangle in the plot), but the agreement is still good.

One interesting feature in the κ vs. R^* plot of Fig. 4.4 is the existence of a minimum allowed value of κ. An analytic expression for this minimum value can found and, since this minimum value must be less than or equal to one for Q-balls to exist, leads to the constraint

$$\alpha \lesssim \frac{1}{\sqrt{1/(0.58)^2 + 9\Omega_0^2/2}}\,. \tag{4.6}$$

This predicts that there are no gauged Q-balls with $\alpha > 0.58$. Numeric solutions give the actual upper limit $\alpha = 0.52$. Ref. [7] notes that for any scalar potential (and its implied attractive force) there must be an upper bound on the allowed gauge coupling (and its implied repulsive force) in order to form a stable Q-ball. This upper bound is Eq. (4.6).

The lower panels of Fig. 4.4 illustrate the behavior of Q and E as a function of R^*. Both Q and E inherit minimal and a maximal values from their corresponding radii. The analytical predictions of Section 3.2 match the numerical results in the region where Q-balls are stable.

Analytic and numeric results for several other benchmarks are compared in Fig. 4.5. The analytic predictions show only small deviations with respect to the numeric results for all benchmarks, demonstrating the resounding success of the analytic methods and approximations presented here. The plots also illustrate that the mapping in Eq. (3.60) holds both qualitatively and quantitatively over the whole parameter space.

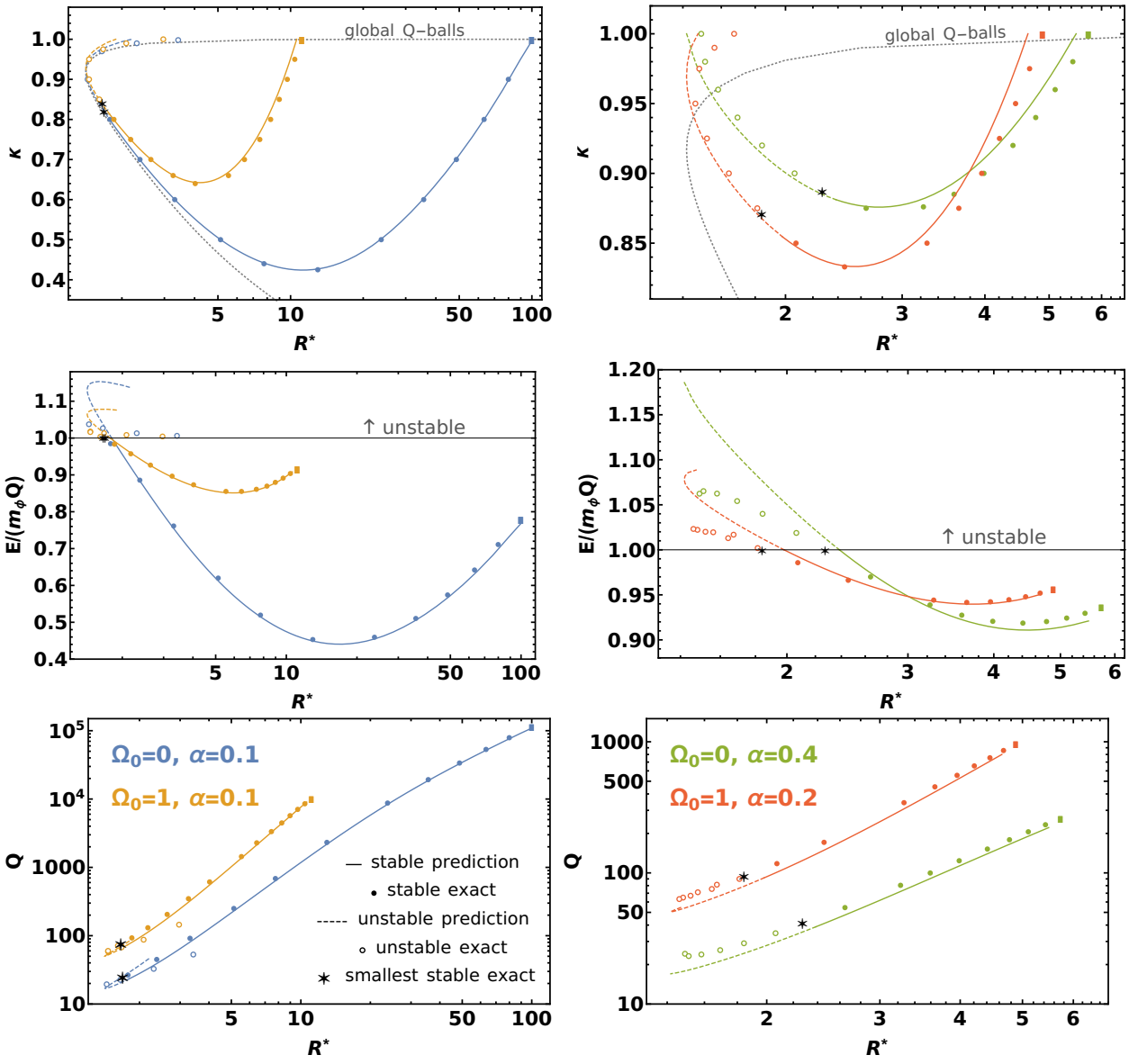

Figure 4.5: A comparison of predictions from Eq. (3.60) and numeric solutions for benchmarks $\Omega_0 = 0$, $\alpha = 0.1$ (*left*, blue), $\Omega_0 = 1$, $\alpha = 0.1$ (*left*, orange). $\Omega_0 = 0$, $\alpha = 0.4$ (*right*, green) and $\Omega_0 = 1$, $\alpha = 0.2$ (*right*, red). Conventions are as in Fig. 4.4.

Using analytic approximations in concert with numeric results, it can be determined that stable, gauged Q-balls have $R^* \gtrsim 1.5$, which is similar to the lower limit of $R^* \sim 1.5$ found for global Q-balls. This matches the physical expectation that the introduction of a repulsive force to a Q-ball should not decrease the Q-ball radius.

Finally, observe that for $\Omega_0 = 0$, the scalar profile is found to be essentially constant in the interior of thin-wall Q-balls (Fig. 3.3, right), and that approximations become more accurate, especially for small α, where the solutions approach the global Q-ball case. For larger Ω_0, the solutions deviate from the global case (Fig. 2.3), but the predictions remain quite accurate.

4.4 Proca

Fig. 2.5 shows two examples of predicted profiles for f and A plotted alongside exact numeric results. The agreement is particularly good for small α and large R^* – the approximations that the mapping formula and profile functions are predicated on – but the predictions remain good for large α and small R^* as well.

Some benchmark scenarios for Proca Q-balls are shown in Fig. 4.6. In addition to exact numeric solutions (circles), analytical predictions (curves) for $\kappa(R^*)$ from the mapping relation in Eq. (3.85) are plotted, as well as the predictions for E and Q. The $\kappa(R^* \to \infty)$ behavior from Eq. (3.86) is clearly visible in the $M = 0.25$ and $M = 1$ benchmarks in the left column.

The benchmark point $M = 0.1$ exhibits an instability at $R^* \sim 23$ due to violation of Eq. (2.47) and therefore has a maximal radius. Using Eq. (2.47) together with $A = A(0)$ from Eq. (3.80) and the mapping relation predicts this instability at $R^* > 16$, which qualitatively agrees with the numerical result. The $M = 0.1$ benchmark also supports Q-shells, which are discussed in Chapter 5.

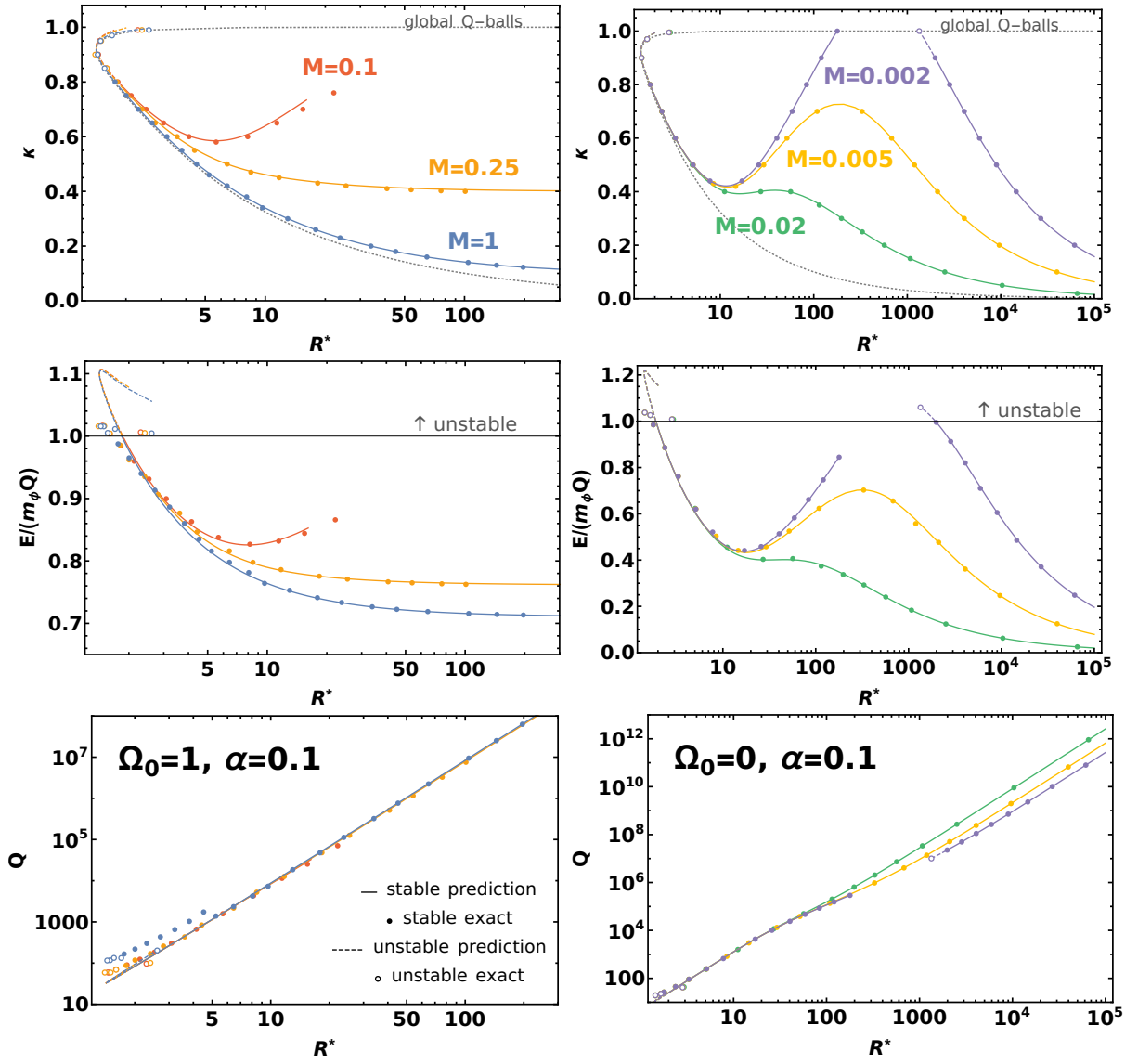

Figure 4.6: Proca Q-ball solutions for $\Omega_0 = 1$ (*left*), $\Omega_0 = 0$ (*right*), and various M as labeled. *Top row:* κ vs. (R^*). *Middle row:* $E/(m_\phi Q)$ vs. R^*. *Bottom row:* Q vs. R^*. The solid lines correspond to the predictions from the mapping (3.85), the dots to exact numeric solutions, and the gray dotted line to the global Q-ball case for comparison. Q-balls are unstable for $E/(m_\phi Q) > 1$.

The behavior of $\kappa(R^*)$ in the benchmarks in the left column suggests a straightforward relationship between κ and R^*. The benchmarks of the right column show that this is not universally the case. For small Ω_0, $\kappa(R^*)$ can have a local maximum at large R^* and thus up to three "branches" of Q-ball solutions for a given κ.[2] Because $\Omega_0 = 0$, these Proca Q-balls resemble global Q-balls for very large R^* and have no maximal charge or radius. However, the case $M = 1/500$ has an instability region around $R^* \in (200, 2000)$, defined by $\kappa > 1$ and $E > m_\phi Q$. These disconnected stability regions are a novel feature of Proca Q-balls.

[2]Some types of Q-balls may have multiple valid solutions with different radii for a single κ. These sets of solutions are grouped into "branches," where small radii up to those associated with a minimum or local minimum in κ form the first branch, medium radii from the local minimum in κ to the local maximum κ form the second branch, and the remaining large radii form the third branch.

Chapter 5

Other Q-states: Q-shells and excited Q-balls

The bulk of this thesis has predominantly treated Q-balls, the spherically symmetric solutions to the Q-ball equations of motion, which physically take the form of a dense ball of Q-particles. Q-solitons also come in other variants; Q-shells and excited states of Q-balls will be briefly discussed here.[1]

Q-shells are solutions to the Q-ball equations of motion (2.26) in which the scalar field ϕ configures into a spherical shell rather than a solid ball. Importantly, they only arise in the presence of a gauge field, i.e. in the gauged and Proca cases. Only Q-balls exist in the global case. Proca Q-shells are particularly interesting because they fall into two classes: solutions that map to gauged Q-shells as $M \to 0$ and solutions that have no $M \to 0$ analogue. The existence of a new class of Proca Q-shells that has no massless gauged Q-shell equivalent is another exciting demonstration of the novel affects that arise uniquely from a gauge field mass.

[1] Q-shells can, in principle, also exhibit excited states. These states are complex and will not be discussed here.

An analytic approach to Q-shell solutions follows the methodology of Chapter 3. In the style of Eq. (1.1), the scalar profile of large radius Q-shells can be approximated as simply

$$f(\rho) = \begin{cases} 0\,, & \rho < R_<\,, \\ 1\,, & R_< \le \rho \le R_>\,, \\ 0\,, & R_> < \rho\,. \end{cases} \tag{5.1}$$

ρ is the radial coordinate, while $R_<$ and $R_>$ are the inner and outer radii of the shell, respectively.

As previously, this ansatz can be used to solve the equation of motion for the gauge field, A.

$$A(\rho) = \begin{cases} A_< \dfrac{R_<}{\rho} \dfrac{\sinh(M\rho)}{\sinh(MR_<)}\,, & \rho < R_<\,, \\ \dfrac{\alpha\Omega}{\mu^2} - \dfrac{A_1}{\rho}\sinh(\mu\rho) - \dfrac{A_2}{\rho}\cosh(\mu\rho)\,, & R_< \le \rho \le R_>\,, \\ A_> \dfrac{R_>}{\rho} e^{(R_>-\rho)M}\,, & R_> < \rho \end{cases} \tag{5.2}$$

$A_<$, A_1, A_2, and $A_>$ are determined by demanding continuity of A and A' at $R_<$ and $R_>$.

Already $f(\rho)$ and $A(\rho)$ are good descriptions of exact Q-shell solutions; however, $f(\rho)$ can be further improved by the introduction of a modified version of the transition function (3.18).

$$f(\rho) = \frac{1}{\sqrt{1+2e^{2(R_<-\rho)}}} \frac{1}{\sqrt{1+2e^{2(\rho-R_>)}}} \tag{5.3}$$

The top panel of fig. 5.3 demonstrates the excellent qualitative and respectable quantitative performance of these approximations when compared to exact results.

Expressions for $R_<$ and $R_>$ as a function of potential parameters allow Q-shells to be fully, if approximately, analytically specified. Requiring continuity in A and A' and $R_<$ and $R_>$ provides four constraints for the six parameters $A_<$, $A_>$, A_1, A_2, $R_<$, and $R_>$. The energy-due-to-friction

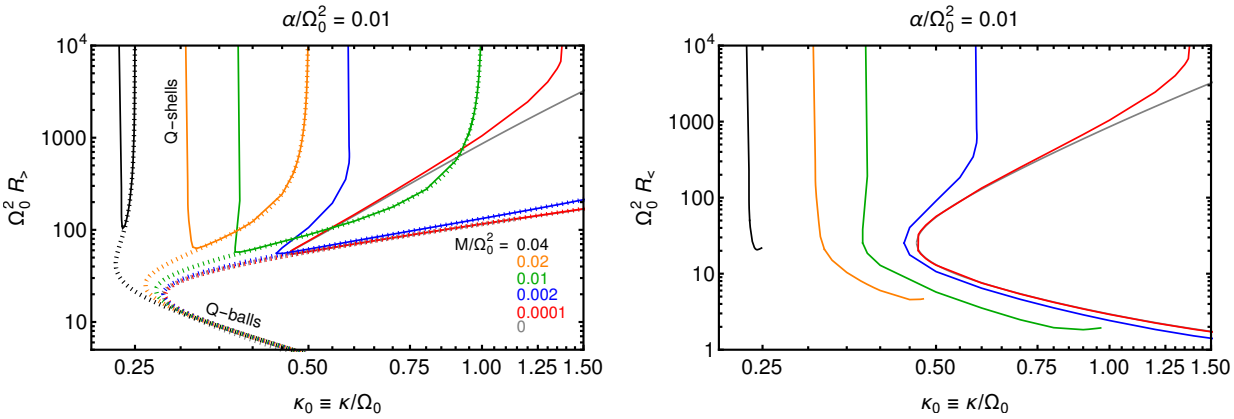

Figure 5.1: Predictions for the Q-shell radii $R_>$ (left) (Eq. (5.5)) and $R_<$ (right) (Eq. (5.4)) at various values of the gauge boson mass M. The narrow Q-shell radii $R_{>,<}$ diverge at κ given by Eq. (5.6). The wide Q-shell radii $R_>$ are degenerate with the Q-ball radii (dashed), and both end at a radius that is determined by Eq. (2.47) for a given Ω_0 (not shown in the plot). The predictions are plotted in terms effective parameters $\Omega_0^2 R_{>,<}$ and κ/Ω_0, which are the original parameters rescaled by Ω_0 as described in [36].

relation of Eq. (2.57) provides the two additional constraints needed to approximate $R_<$ and $R_>$, as detailed in [36].

$$R_< \simeq -\left[\kappa^2 - \alpha A_< (2\Omega - \alpha A_<)\right]^{-1} , \tag{5.4}$$

$$R_> \simeq \left[\kappa^2 - \alpha A_> (2\Omega - \alpha A_>)\right]^{-1} \tag{5.5}$$

While not as conducive to further analytic solubility as similar expressions for Q-balls, Eqs. (5.1) and (5.2) can be solved numerically to predict Q-shell radii as a function of the potential parameters.

As with Q-balls, κ may be determined as a function of the potential parameters.

$$\kappa^2 \sim \frac{\alpha^2 - M^2 + \sqrt{(\alpha^2 - M^2)^2 + 8M\alpha^2\Omega_0^2}}{2M} \tag{5.6}$$

At this value of κ, the Q-shell radii will grow without bound. This result is derived in the thin-wall (i.e. large radius) limit, which in Q-shells means both $R_<$ and $R_>$ are infinite. Functionally, the limit applies to very thin shells.

Fig. 5.1 shows predictions for outer and inner radii of Q-shells of various M, as compared to the radii predictions of their corresponding Q-balls, which form under the same potential parameters. Wide Q-shells are degenerate with their sister Q-balls at their outer radii. Narrow Q-shells diverge at the κ from Eq. (5.6). The wide-shell – Q-ball correspondence does not mean that all Proca Q-balls have a corresponding Q-shell; Q-balls which exhibit a one-to-one relationship between κ and R^* do not have associated Q-shells.

Fig. 5.2 compares exact Q-ball and Q-shell solutions to the analytic predictions of Eqs. (5.1) and (5.2). The benchmark presented is unique to the Proca case and contains no gauged Q-shell analogue. (Gauged Q-shells have a massless gauge field, i.e. $M \to 0$.) It shows highly satisfactory agreement between predictions and numerics and a perfect overlap of Q-ball and wide Q-shell solutions. This one-to-one degeneracy suggests that the Q-ball mapping relation may be used to predict Q-shell outer radii in place of the more complex prediction (5.5).

Interestingly, Fig. 5.2 shows that $E/(m_\phi Q)$ is smaller, for a given Q, for narrow Q-shells than for other solutions. Since $E/(m_\phi Q)$ is a measure of stability, this implies that narrow Q-shells may be more stable than other Q-solitons for a given Q. If this is true, then production of Q-solitons would favor narrow Q-shells at these locations in parameter space. The phenomenological implications of this result are an open question.

Fig. 5.3 shows the trajectory of the scalar and gauge fields in the Proca potential space. A notable difference to the case of gauged Q-solitons, i.e. $M = 0$, is that A need not be monotonic in the Proca case. The right lower plot clearly shows such a non-monotonic trajectory for a narrow Proca Q-shell.

Investigation of further classes of Q-solitons and their excited states is ongoing. A more extensive treatment of excited Q-balls that builds on the foundations presented here has, at the time of writing, recently been released in preprint. [37]

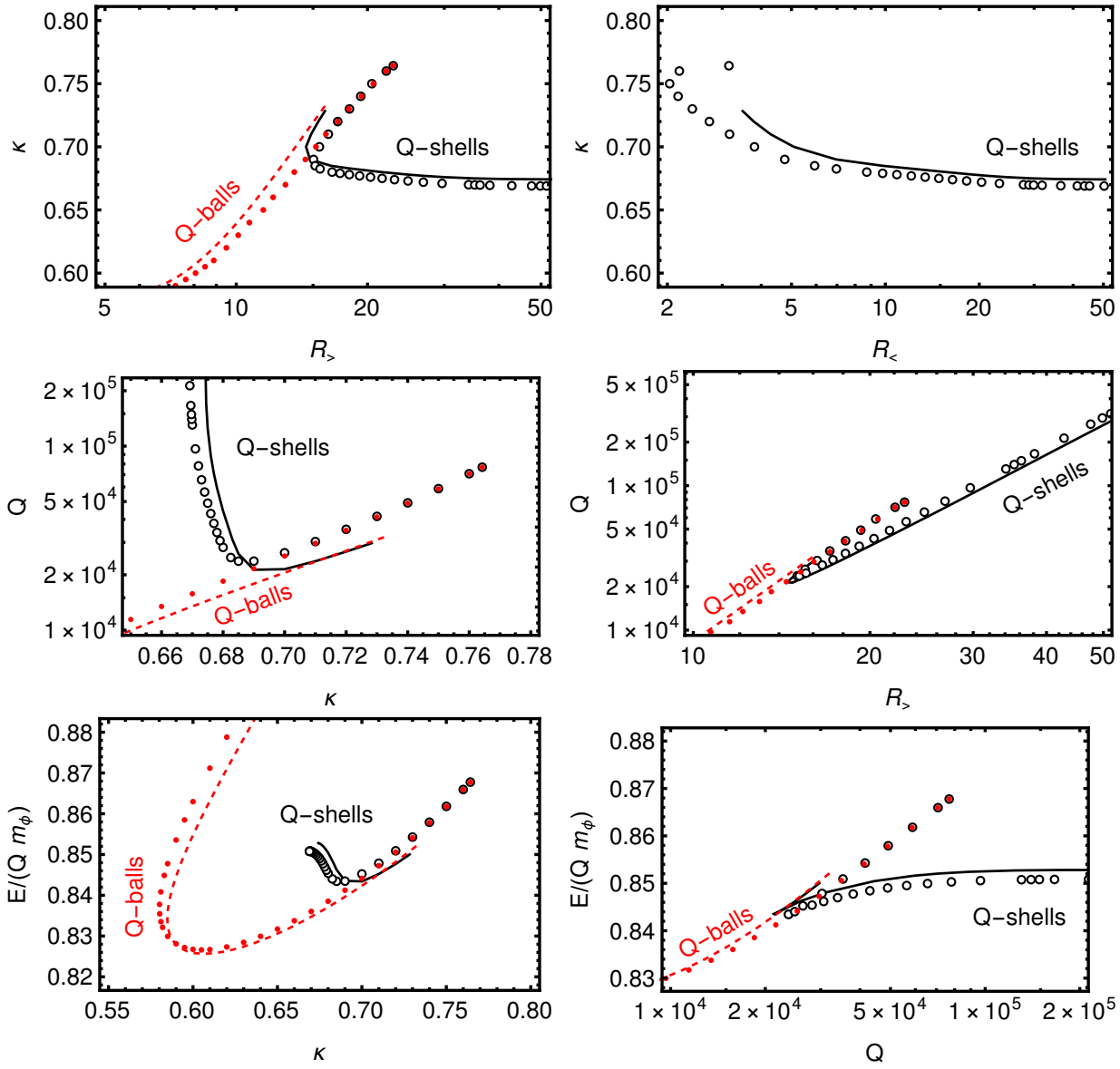

Figure 5.2: Proca Q-solitons for the benchmark $\alpha = M = \Omega_0/10 = 1/10$, $\phi_0 = m_\phi$. The red and black points are exact Q-ball and Q-shell solutions, respectively. Dashed lines are analytic predictions. (The full Q-ball branch for this benchmark is shown in Fig. 4.6.) Wide Q-shells are degenerate with Q-balls and cease to exist for $\kappa > 0.76$ due to the instability described in Eq. (2.47).

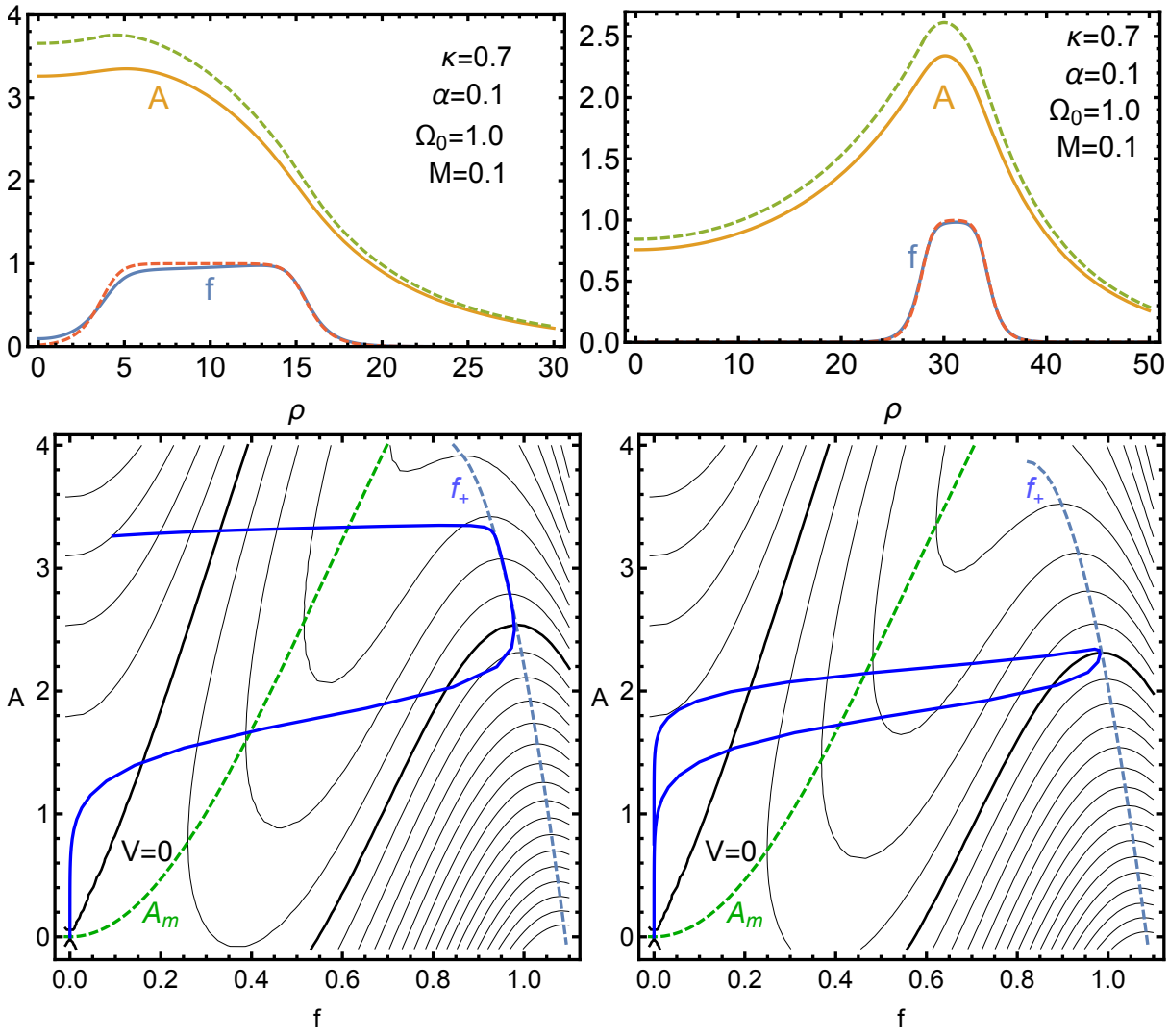

Figure 5.3: *Left:* Profiles and contour plots of a wide Proca Q-shell. *Right:* Profiles and contour plots of a narrow Proca Q-shell. *Top:* The top row shows both numeric (blue, orange curves) and approximated (red, green dashes) profiles for the scalar and Proca gauge fields, respectively, of a sample Proca parameter set. *Bottom:* The dark blue line is the trajectory of the Proca Q-shell through potential space. The values of the f maximum f_+ (blue) and A minimum A_m (green) are shown with dashed lines.

Chapter 6

Phenomenology of Q-balls

6.1 Macroscopic dark matter

The original impetus for the study of Q-solitons presented here was curiosity regarding possible macroscopic dark matter candidates. Macroscopic dark matter is a class of dark matter candidates that fall in the mass region between particle dark matter and ultraheavy dark matter. These dark matter "macros" are generally conceived as composite particles that behave very similarly to a nucleus and are of approximately the same density. Dark matter macros range in mass from a minimum of ~ 55 g up to tonnes. For comparison, WIMPs, a relatively heavy particle dark matter candidate, weigh in at approximately 10^{-20} grams, while ultraheavy dark matter is on the order of solar masses. As such, flux of macroscopic dark matter would be quite small, which excuses its non-detection for wide swaths of parameter space.

In general, dark matter macros are difficult to produce in theoretical models. Models that predict macros generally produce them from Standard Model or dark quark matter, which is compressed by some mechanism to approximately nuclear density. After compression, it is able to persist in a stable state – usually after incorporating extra considerations, for example

enhanced conversion rates of down quarks to strange quarks. It should be noted that many of these candidates are actually not traditionally "dark" in the sense of having very weak or no interactions with the Standard Model, but their number density is low enough for them to be considered dark matter candidates nonetheless. Less dense candidates of approximately atomic density can also be considered, but below certain densities they become more difficult to search for terrestrially because they rip apart in the atmosphere. Additionally, they are more difficult to produce in theoretical models.

Q-balls are an exception to the (admittedly limited) macroscopic dark matter model landscape in that they are Beyond the Standard Model objects rather than an exotic state of normal matter. This fact provides a convenient complementarity with the prevailing sentiment that dark matter should be a new, Beyond the Standard Model particle, while simultaneously making available a currently weakly-constrained region of dark matter parameter space to Q-ball candidates.

Because of the difficulties in developing production mechanisms theoretically, macroscopic dark matter candidates have received little attention experimentally. As such, the parameter space for macroscopic dark matter is still relatively unconstrained, with some of the more serious bounds arising from such unlikely sources as the dramatically-titled "Death and Serious Injury from Dark Matter," [38] which constrains macros based on the fact that we have yet to observe one of these high-energy composites kill anyone. Macroscopic dark matter candidates present an exciting new class of dark matter candidates, with much breadth for exploration and innovation, precisely because they have received so little consideration to date.

6.2 Macro production

A fundamental difficulty in building models with macros is that they must be simultaneously stable, i.e. have a lower energy density than other accessible states of matter, but also relatively

impervious to ordinary matter since it is not observed collapsing into the stable macro state. In practice, this requires a mechanism of generating macros that is no longer accessible, in addition to conditions ensuring both macro stability and a resistance to macro conversion by ordinary matter.

One prospective mechanism for achieving these objectives is through a first-order QCD phase transition that results in a novel configuration of ordinary matter inside persistent, initial-phase nuggets. While lattice calculations have increasingly disfavored a first-order QCD phase transition, an early example of such a production mechanism by Witten is provided here to demonstrate the mechanics of these types of mechanisms.

6.2.1 Hot quark nuggets

An early but now disfavored theory of macroscopic dark matter was proposed by Edward Witten in 1984 [39]. At the time, the possibility was not yet ruled out that the Universe could have undergone a first-order QCD phase transition at ~ 100 MeV. Witten begins with the assumption that a transition from quasifree, light quarks to mesons and baryons occurred at $T_c \approx 100-200$ MeV and explores the consequences.

In the event of a smooth, first-order phase transition in which equilibrium was maintained to such a degree that high- and low-temperature phases could coexist, the compression of stable, high-temperature bubbles into a new form of hot quark matter ("nuggets") was a possibility. Quark matter would not be dark in the traditional sense, i.e. being weakly coupled or uncoupled to the Standard Model, but rather would occur in such low number densities as to go undetected to date.

The formation of such nuggets would proceed as follows: Two possible phases were present in the early Universe, separated by a phase transition at temperature T_c: a high-temperature

phase in which quasi-free, virtually massless quarks were loosely bound into baryons, and a low-temperature phase in which baryons became massive particles of at least $\sim$ 1 GeV. The temperature of the phase transition, T_c, was the temperature at which the high- and low-temperature phases had equal pressures and could coexist. As the temperature of the Universe dropped below T_c, low-temperature bubbles began nucleating out of the high-temperature phase. In a typical, non-equilibrium, first-order phase transition, these nucleated bubbles would expand explosively, quickly overtaking and eradicating the high-temperature phase. However, in the equilibrium transition, the expanding low-temperature bubbles compressed the high-temperature phase as they grew, reheating it to $T > T_c$ and increasing its pressure on their domain walls, counteracting their growth. Eventually the heat pressure of the high-temperature phase balanced the energetic expansion pressure of the low-temperature phase, and the low-temperature bubbles stopped expanding. This equilibrium was maintained absent the expansion of the Universe.

But of course, the Universe was expanding. This diluted the energy of the high-temperature phase and decreased its heat-induced pressure on the low-temperature bubbles. In order to maintain an overall heat pressure to balance the low-temperature bubbles, the hot-temperature phase had to shrink to reequilibrate its temperature. As the Universe continued to expand, the low-temperature bubbles grew, but they grew slowly, driven by the expansion of the Universe rather than an energy differential between the high- and low-temperature phases.

As the low-temperature bubbles grew and began meeting each other, they began to coalesce up to a size $R_1 \approx$ few centimeters, at which point the dynamics of surface tension, heat transfer, and fluid motion rendered coalescence energetically unfavorable. After reaching R_1, the low-temperature bubbles retained their shaped and continued growing without further coalescence. When the low-temperature bubbles grew to occupy $\sim$ 50% of the overall volume of the Universe, pockets of high-temperature phase began to be pinched off into effective bubbles, which shrank as the Universe continued to expand and cool. Witten estimated that these

high-temperature bubbles would have radii on the order of $1 - 10^4$ cm and would contain $80 - 99\%$ of all the baryons in the universe.[1] Further expansion continued to shrink the high-temperature bubbles, which could have either disappeared or persisted in a stable, compressed state of quark matter.

There is a narrow path for the formation of macroscopic dark matter in this scenario. Its viability turns on the admittedly unlikely assumption that the high-temperature bubbles unnaturally suppress certain heat loss processes, but its convenience is obvious: persistent high-temperature bubbles are unique is in their ability to source extreme asymmetric baryon densities and form dark matter.

As the Universe continued to expand, the high-temperature phase would hemorrhage heat into the low-temperature phase in order to maintain it at the critical temperature, T_c. There are two potential mechanisms for this heat loss: surface evaporation and neutrino emission.

Surface evaporation is exactly what it seems: a shedding of the contents of the high-temperature bubble into the low-temperature phase from the surface region of the high-temperature bubble. Such emission releases the baryonic content of the high-temperature bubble into the low-temperature phase.

Neutrino emission, by contrast, originates from anywhere within a mean-free-path distance from the surface. Such emission produces heat loss without the loss of baryons. In a scenario in which surface emissions from the high-temperature bubbles are suppressed, only particles with a sufficiently long diffusion length can escape the bubble. The baryons in the high-temperature bubbles, which have a much shorter diffusion length than the neutrino mean free path, would remain trapped in the high-temperature phase in such a scenario. The high-temperature bub-

[1] Although dark matter is expected to be primarily non-baryonic, there are observational discrepancies between the amount of visible baryonic matter and the predicted production rates of baryons during Big Bang nucleosynthesis. Quark nuggets are additionally compelling for providing a mechanism to produce this discrepancy.

bles would continue steadily shrinking, losing heat via neutrino emission, all the while building an increasing baryon excess inside.

These quark-matter bubbles would continue to shrink, eventually occupying a tiny fraction of the total volume of the Universe but containing 80-99% of its overall baryons. Their final state would be lumps of hot quark matter with a density $\rho \approx 10^{15}$ g/cm^3 and mass of $10^9 - 10^{18}$ g. There is a possibility that such lumps could persist to present times in a stable or slowly decaying form, a compact soup of loosely bound quarks in an exotic state of quark matter with a density somewhat above that of nuclear matter. The most compelling prospect for the stability of such quark matter is a scenario in which down quark to strange quark conversions become energetically favorable in this hot, quasifree quark phase, reducing the energy per quark and resulting in more tightly-bound quark matter with increased stability. Other suggestions include quark matter that decays via the weak force, but slowly enough for remnants to persist today.

As a brief aside, this state of stable, strange-quark matter has been studied by others. [40, 41] While heavier than ordinary, quasi-free quark matter due to the increased proportion of strange quarks, it is still more stable due to the Pauli exclusion principle. Witten estimates that the energy per quark in up-down-strange quark matter is $\sim$ 90% that of up-down quark matter, potentially offsetting the energy penalty associated with the strange quark mass, although the stability of strange-quark matter has been unable to be confirmed.

De Rujala and Glashow [40] find that strange quark nuggets possess a net positive charge and attract an electron cloud "atmosphere" around themselves, which act as a buffer to atomic collisions, complicating their interaction picture. Others [42] are not optimistic about the prospects for stable quark matter, and report that nuggets with baryon number less than 10^{52} would have evaporated before the Universe cooled to 1 MeV. Such a baryon number represents a planetary-sized mass.

Nonetheless, if such quark nuggets were to still exist, the rate of collisions with Earth would be in the neighborhood of one per year ($r \approx 10^{-2}$ cm) to 1 in 10^9 years ($r \approx 10$ cm). These quark nuclei would rocket through the Earth, vaporizing everything in their path along a tube of 0.001–10 cm radius. Such a prospect is the focus of the experimental constraint efforts detailed in Section 6.3.

Unfortunately, such a scenario is plagued by many possible avenues to decay and evaporation, and a single, narrow, contrived path to stability. Witten himself acknowledged that stable dark macros are implausible, in particular because there is no immediate reason to suspect neutrino emission dominates over surface emission for heat loss; subsequent publications have essentially ruled out such nuggets almost entirely, even before the prospect of a first-order QCD phase transition became disfavored.

While quark-nugget macros are no longer considered viable macroscopic dark matter candidates, the substantial wrangling required to generate them foreshadows the persistent difficulties encountered in macro production. Q-balls are no exception.

6.2.2 Q-ball production

Q-ball production is an open question and one under active consideration by the author and collaborators. While a clean and very precise description of Q-balls has emerged, issues of production and stability in the presence of matter - Q-ball and Q-ball - Q-ball interactions are much more challenging.

Despite detailed knowledge of the stability of various types of Q-balls, including how stability depends on the Q-ball parameters, it remains unclear if and how Q-balls can subdivide (or, equivalently, merge) and what the dynamics of Q-balls would be in a theory that allows subdivision. Is there a smallest stable Q-ball that coexists in Nature with a spectra of larger,

quasi-stable Q-balls? When Q-balls are impacted by ordinary matter or other Q-balls, do they shatter into Q particles, smoothly cleave in two, or simply jump into an excited state? Can excited Q-balls merge or split into less stable Q-balls as an alternative to de-exciting? While the path forward in understanding these dynamics is itself unclear, these questions precede the consideration of the even more difficult problem of how to produce Q-balls.

Fortunately, even in the absence of a compelling production mechanism, Q-ball phenomenology can independently pass judgment on the viability of these dark matter candidates through a number of constraints, some of which are quite inventive.

6.3 Constraints on macroscopic dark matter parameter space

As stated previously, owing to limited theoretical activity, macroscopic dark matter has received little experimental attention, with no dedicated experiments allocated to its parameter space. As such, these macros are able to be initially constrained with a variety of basic, armchair considerations. A summary of the major constraints can be found in [43] and follow-up papers.

Two relevant astrophysical constraints provide upper bounds on macro masses and interaction cross sections. Microlensing surveys rule out macros with $M \geq 10^{24}$ g, while the absence of thermonuclear runaway events from white dwarfs provides an even tighter mass constraint of $M \lesssim 10^{15}$ g. Negative detection of the scattering of CMB photons from macros constrains the geometric interaction cross section to the range $\sigma \approx 10^{-9} \sim 1$ cm^2 over generations of macro mass from milligrams to tonnes.

The region 55 g $\leq M \lesssim 10^{15}$ g remains essentially wide open for dense dark matter macros. Mica, granite, or similarly light-colored rock slabs provide the first of several heuristic attempts to constrain this parameter space. [43] "Countertop searches" – literally, investigating granite countertop slabs for evidence of past collision events – attempt to trace deposits of macros in

light-colored rock. Granite slabs provide an easily-accessible, visual history of nuclear-density macro impacts (or lack thereof).

A nuclear-density macro incoming from space would contain a tremendous amount of kinetic energy, which would vaporize a core through an impacted rock and then melt a larger cylinder of rock around that core. This heat shock would restructure the chemical composition of the melted rock, which would subsequently recalcify with a different color and structure than the surrounding granite. These tracks would remain in the rock as a type of fossil record of macro impacts accrued during its lifetime of surface exposure, and would be visible as circles or ellipses in subsequent thin slabs of the granite. Since there are veins of granite that have been exposed on the Earth's surface for hundreds of thousands of years, these rocks have the unique ability to have served as detectors for incredibly long periods of of time.

Conveniently, granite is commercially farmed and available in slabs that are amenable to looking for tracks on either side of the cut part of the slab, including the slabs available in local countertop supply stores. Sidhu, Starkman, and Harvey [43] estimate that such countertop searches can constrain the parameter space from $10 \lesssim M \lesssim 10^6$ g for interaction cross sections from $\sigma \sim 10^{-5}$ cm^2 up to the CMB photon scattering bound.

In a similar vein, high-energy macros that can melt and vaporize rock would have devastating consequences if impacting a human body, presumably causing serious bodily injury or even death. [38] Such impacts would resemble gunshot wounds traversing the body, presenting an unexplained and mysterious phenomenon to medical professionals perplexed as to the apparent lack of a weapon, bullet, or perpetrator. Under the assumption that such bizarre injuries would have been reported by news outlets and medical journals had they occured, Sidhu, Scherrer, and Starkman place constraints on macro parameter space from $10^{-2} \lesssim M \lesssim 10^5$ g for geometric cross sections from $\sigma \sim 10^{-7}$ cm^2 up to the CMB photon scattering bound.

Another detection proposal for dark matter macros, which would additionally help constrain less dense macros that break up before reaching Earth's surface, are remote camera networks. [44] Incoming macros would heat the air column surrounding them into a plasma, which would emit visible light upon cooling. Sky-camera networks such as the U.S. Prairie Network, Canadian Network, Eastern European Network, and the Australian Desert Fireball Network have never detected an object moving fast enough to have originated outside the solar system. (Dark matter macros are expected to arrive at speeds faster than meteorites but slower than cosmic rays.) Continued observation by these networks progressively constrains the dark matter macro parameter space.

Incoming macros would also cause nitrogen florescence due to their ionization of atmospheric nitrogen. Cosmic ray detectors could potentially be repurposed to detect this florescence. A simple way to distinguish dark matter macros from cosmic rays is that, unlike cosmic rays, they do not shower.

6.4 Q-ball interactions

Given that there is considerable breathing room for Q-ball candidates in the macro dark matter parameter space, the pertinent considerations for phenomenology become their measurable Standard Model interactions, scattering cross sections, and other characteristic experimental signals. Some work has already been done in this department, e.g. the treatment of Q-ball dark matter scattering off of nucleons. [10]

The Q-balls described here give rise to two immediate Standard Model portals:

1. The scalar field ϕ of Q-balls is generally assumed to have a Higgs-portal coupling to the Standard Model. [11]

2. The gauge boson A of gauged and Proca Q-balls kinetically mixes with Standard Model photons and Z bosons.

Both of these portals produce distinct experimental signatures which can constrain Q-ball masses and couplings.

For gauged and Proca Q-balls, the underlying $U(1)$ symmetry of the Q-ball scalar field ϕ can be associated with various natural symmetries, e.g. $U(1)_{B-L}$, which gives rise to myriad Q-ball phenomenologies.

- $U(1)'$: A is a dark or hidden photon. Only ϕ is charged. Standard Model coupling occurs via kinetic mixing, which is proportional to electric charge if A is light and hypercharge if A is heavy. Q-balls repel each other but do not act on normal matter at long distances.
- $U(1)_{B-L}$: Q-balls couple directly to all Standard Model fermions via A. This interaction is effectively a Q-ball - neutron interaction. Light A can exhibit a long-range Q-ball - neutron force.
- $U(1)_{L_e-L_\alpha}$: Q-balls couple only to electrons and leptons of flavor $\alpha \in \{\mu, \tau\}$ and their neutrinos. Q-balls scatter only on electrons, not nucleons.
- $U(1)_{L_\mu-L_\tau}$: Q-balls couple only to muons, taus, and their neutrinos.

Which of these phenomenologies are compatible with macroscopic dark matter and Standard Model mixing and coupling constraints is under active investigation by the author and collaborators. Our hope is that the parametric liberties granted to Q-balls as macroscopic dark matter candidates will help evade the stringent constraints of Standard Model interactions. Specific models and phenomenological constraints are expected to be the subject of future publications.

Chapter 7

In closing

Q-balls are curious objects that arise in certain $U(1)$-symmetric scalar field theories. This thesis provides a guide to understanding Q-ball solutions, along with simple formulae that describe their salient characteristics without the need to numerically solve their underlying differential equations. The analytic approximations presented here significantly improve upon the results of previous methods both qualitatively and quantitatively.

Global Q-balls are described in arbitrary $U(1)$-symmetric, sextic potentials to $\sim 10\%$ accuracy for small Q-balls, and much better for large Q-balls. In an effective field theory, these potentials capture the leading dynamics which produce Q-balls and are therefore of particular interest. The global scalar profile presented here closely describes the exact solution to the differential equation over a wide range of parameters, as do the derived analytic formulae for the resulting Q-ball properties, namely the charge, energy, and radius.

Promoting the $U(1)$ symmetry to a gauge symmetry complicates the discussion significantly and has previously eluded analytical descriptions outside of some limiting cases. This thesis has described methods to obtain essentially all properties of gauged Q-balls via a mapping to global Q-balls. Since the latter can be easily obtained numerically and often even analytically,

this mapping allows for an excellent prediction of the gauged Q-ball properties without the need to solve their coupled, nonlinear differential equations.

This dissertation also presents novel results for Q-balls with a massive Proca gauge boson. The resulting solitons are similar to the global ones for large Proca masses and similar to gauged ones for small Proca masses. For intermediate gauge boson masses, Proca Q-balls show unique features such as extremely large minimal radii and charge. Analytic approximations for the scalar and gauge profiles provided for Proca Q-balls allow insights into their behavior and also make possible efficient numerical studies.

While the analytic approximations presented here perform best in the large-radius limit, they also provide complementarity to numerical studies, which more easily describe smaller Q-balls. Additionally, these analytic approximations serve as reliable seed functions for numerical finite-element methods, enabling these methods to succeed in generating solutions that would be impenetrable without the accurate initial guesses that these approximations provide.

The results of this thesis are of great value for simply and accurately calculating the properties of Q-balls for use in various cosmological and astrophysical studies. In addition, since the sextic potential was left completely general, these results will apply for a wide variety of specific sextic potentials describing various effective field theories. Open avenues for further study include Q-balls' stability with respect to decay into smaller solitons as well as the reverse issue of Q-ball formation from smaller solitons and individual scalars. The possibility of transitions between Q-balls and Q-shells of equal charge is also salient. Addressing these questions will advance a more complete understanding of how these solitons might be produced in the early universe and how they might persist as a component of the Universe's dark matter.

Bibliography

[1] F. Zwicky, "On the Masses of Nebulae and of Clusters of Nebulae," *The Astrophysical Journal* **86**, p. 217, Oct. 1937.

[2] S. Coleman, "Q-balls," *Nuclear Physics B* **262**, pp. 263–283, Dec. 1985.

[3] G. Rosen, "Particlelike Solutions to Nonlinear Complex Scalar Field Theories with Positive-Definite Energy Densities," *Journal of Mathematical Physics* **9**, pp. 996–998, July 1968.

[4] E. Y. Nugaev and A. V. Shkerin, "Review of Nontopological Solitons in Theories with U(1)-Symmetry," *Journal of Experimental and Theoretical Physics* **130**, pp. 301–320, Feb. 2020.

[5] T. Lee and Y. Pang, "Nontopological solitons," *Physics Reports* **221**, pp. 251–350, Nov. 1992.

[6] M. Colpi, S. L. Shapiro, and I. Wasserman, "Boson Stars: Gravitational Equilibria of Self-Interacting Scalar Fields," *Physical Review Letters* **57**(20), pp. 2485–2488, 1986.

[7] K. Lee, J. A. Stein-Schabes, R. Watkins, and L. M. Widrow, "Gauged Q balls," *Physical Review D* **39**(6), pp. 1665–1673, 1989.

[8] R. Friedberg, T. Lee, and A. Sirlin, "Class of scalar-field soliton solutions in three space dimensions," *Physical Review D* **13**(10), pp. 2739–2761, 1976.

[9] A. Kusenko and M. Shaposhnikov, "Supersymmetric Q-balls as dark matter," *Physics Letters B* **418**, pp. 46–54, Jan. 1998.

[10] A. Kusenko and P. J. Steinhardt, "Q-Ball Candidates for Self-Interacting Dark Matter," *Physical Review Letters* **87**(14), 2001.

[11] E. Pontón, Y. Bai, and B. Jain, "Electroweak symmetric dark matter balls," *Journal of High Energy Physics* **2019**, pp. 1–47, Sept. 2019.

[12] Y. Bai and J. Berger, "Nucleus capture by macroscopic dark matter," *Journal of High Energy Physics* **2020**, pp. 1–21, May 2020.

[13] A. Kusenko, V. Kuzmin, M. Shaposhnikov, and P. Tinyakov, "Experimental Signatures of Supersymmetric Dark-Matter Q-Balls," *Physical Review Letters* **80**(15), pp. 3185–3188, 1998.

[14] E. Krylov, A. Levin, and V. Rubakov, "Cosmological phase transition, baryon asymmetry, and dark matter Q-balls," *Physical Review D* **87**(8), 2013.

[15] D. Croon, A. Kusenko, A. Mazumdar, and G. White, "Solitosynthesis and gravitational waves," *Physical Review D* **101**(8), 2020.

[16] G. Rosen, "Dilatation Covariance and Exact Solutions in Local Relativistic Field Theories," *Physical Review* **183**(5), pp. 1186–1188, 1969.

[17] S. Theodorakis, "Analytic Q ball solutions in a parabolic-type potential," *Physical Review D* **61**(4), 2000.

[18] I. E. Gulamov, E. Y. Nugaev, and M. N. Smolyakov, "Analytic Q-ball solutions and their stability in a piecewise parabolic potential," *Physical Review D* **87**(8), 2013.

[19] I. Wolfram Research, "Mathematica." Wolfram Research, Inc., 2021.

[20] I. E. Gulamov, E. Y. Nugaev, A. G. Panin, and M. N. Smolyakov, "Some properties of U(1) gauged Q-balls," *Physical Review D* **92**(4), 2015.

[21] Y. Brihaye, A. Cisterna, B. Hartmann, and G. Luchini, "From topological to nontopological solitons: Kinks, domain walls, and Q-balls in a scalar field model with a nontrivial vacuum manifold," *Physical Review D* **92**(12), 2015.

[22] H. Ishihara and T. Ogawa, "Charge-screened nontopological solitons in a spontaneously broken U(1) gauge theory," *Progress of Theoretical and Experimental Physics* **2019**, Feb. 2019.

[23] H. Ishihara and T. Ogawa, "Homogeneous balls in a spontaneously broken U(1) gauge theory," *Physical Review D* **99**(5), 2019.

[24] P. Forgács and Á. Lukács, "Nontopological solitons in Abelian gauge theories coupled to U(1)xU(1) symmetric scalar fields," *Physical Review D* **102**(7), 2020.

[25] H. Ishihara and T. Ogawa, "Variety of nontopological solitons in a spontaneously broken U(1) gauge theory: Dust balls, shell balls, and potential balls," *Physical Review D* **103**(12), 2021.

[26] H. Ruegg and M. Ruiz-Altaba, "The stueckelberg field," *International Journal of Modern Physics A* **19**, pp. 3265–3347, Aug. 2004.

[27] M. Grillakis, J. Shatah, and W. Strauss, "Stability theory of solitary waves in the presence of symmetry, I," *Journal of Functional Analysis* **74**, pp. 160–197, Sept. 1987.

[28] M. I. Tsumagari, E. J. Copeland, and P. M. Saffin, "Some stationary properties of a Q-ball in arbitrary space dimensions," *Physical Review D* **78**(6), 2008.

[29] M. Mai and P. Schweitzer, "Energy momentum tensor, and the D-term of Q-balls," *Physical Review D* **86**(7), 2012.

[30] F. Paccetti Correia and M. G. Schmidt, "Q-balls: Some analytical results," *The European Physical Journal C - Particles and Fields* **21**, pp. 181–191, June 2001.

[31] I. E. Gulamov, E. Y. Nugaev, and M. N. Smolyakov, "Theory of U(1) gauged Q-balls revisited," *Physical Review D* **89**(8), 2014.

[32] T. Ioannidou, V. Kopeliovich, and N. Vlachos, "Energy-charge dependence for Q-balls," *Nuclear Physics B* **660**, pp. 156–168, June 2003.

[33] J. Heeck, A. Rajaraman, R. Riley, and C. B. Verhaaren, "Mapping gauged Q-balls," *Physical Review D* **103**, p. 116004, June 2021.

[34] J. Heeck, A. Rajaraman, R. Riley, and C. B. Verhaaren, "Proca Q-balls and Q-shells," *arXiv:2107.10280 [hep-ph, physics:hep-th]* , July 2021.

[35] A. Masoumi, K. D. Olum, and B. Shlaer, "Efficient numerical solution to vacuum decay with many fields," *Journal of Cosmology and Astroparticle Physics* **2017**, p. 051, Jan. 2017.

[36] J. Heeck, A. Rajaraman, and C. B. Verhaaren, "Ubiquity of gauged Q -shells," *Physical Review D* **104**, p. 016030, July 2021.

[37] Y. Almumin, J. Heeck, A. Rajaraman, and C. B. Verhaaren, "Excited Q-Balls," *arXiv:2112.00657 [hep-ph, physics:hep-th]* , Dec. 2021.

[38] J. S. Sidhu, R. Scherrer, and G. Starkman, "Death and serious injury from dark matter," *Physics Letters B* **803**, p. 135300, Apr. 2020.

[39] E. Witten, "Cosmic separation of phases," *Physical Review D* **30**(2), pp. 272–285, 1984.

[40] A. De Rújula and S. L. Glashow, "Nuclearites—a novel form of cosmic radiation," *Nature* **312**, pp. 734–737, Dec. 1984.

[41] P. B. Price, "Limits on contribution of cosmic nuclearites to galactic dark matter," *Physical Review D* **38**, pp. 3813–3814, Dec. 1988.

[42] C. Alcock and E. Farhi, "Evaporation of strange matter in the early Universe," *Physical Review D* **32**, pp. 1273–1279, Sept. 1985.

[43] J. S. Sidhu, G. Starkman, and R. Harvey, "Counter-top search for macroscopic dark matter," *Physical Review D* **100**, p. 103015, Nov. 2019.

[44] J. S. Sidhu and G. Starkman, "Macroscopic dark matter constraints from bolide camera networks," *Physical Review D* **100**, p. 123008, Dec. 2019.